CO_2 CORROSION OF HIGH STRENGTH STEEL WIRES IN THE ANNULUS OF FLEXIBLE PIPES

Tatiane Seixas Campos

Tese de Doutorado apresentada ao Programa de Pós-graduação em Engenharia Metalúrgica e de Materiais, COPPE, da Universidade Federal do Rio de Janeiro, como parte dos requisitos necessários à obtenção do título de Doutor em Engenharia Metalúrgica e de Materiais.

Orientador: José Antônio da Cunha Ponciano Gomes

Rio de Janeiro
Maio de 2022

CO_2 CORROSION OF HIGH STRENGTH STEEL WIRES IN THE ANNULUS OF FLEXIBLE PIPES

Tatiane Seixas Campos

TESE SUBMETIDA AO CORPO DOCENTE DO INSTITUTO ALBERTO LUIZ COIMBRA DE PÓS-GRADUAÇÃO E PESQUISA DE ENGENHARIA DA UNIVERSIDADE FEDERAL DO RIO DE JANEIRO COMO PARTE DOS REQUISITOS NECESSÁRIOS PARA A OBTENÇÃO DO GRAU DE DOUTOR EM CIÊNCIAS EM ENGENHARIA METALÚRGICA E DE MATERIAIS.

Orientador: José Antônio da Cunha Ponciano Gomes

Aprovada por: Prof. José Antônio da Cunha Ponciano Gomes
Prof.ª Marysilvia Ferreira da Costa
Prof. Sérgio Souto Maior Tavares
Dr. Marcelo Torres Piza Paes
Dr.ª Marion Elisabeth Seiersten

RIO DE JANEIRO, RJ - BRASIL
MAIO DE 2022

Campos, Tatiane Seixas

CO_2 corrosion of high strength steels wires in the annulus of flexible pipes / Tatiane Seixas Campos. – Rio de Janeiro: UFRJ/COPPE, 2022.

XIV, 84 p.: il.; 29,7 cm.

Orientador: José Antônio da Cunha Ponciano Gomes

Tese (doutorado) – UFRJ/ COPPE/ Programa de Engenharia Metalúrgica e de Materiais, 2022.

Referências Bibliográficas: p.76 - 84.

1. Corrosão por CO_2. 2. Dutos flexíveis. 3. Espaço anular. 4. Siderita. 5. pH próximo ao neutro. I. Gomes, José Antônio da Cunha Ponciano. II. Universidade Federal do Rio de Janeiro, COPPE, Programa de Engenharia Metalúrgica e de Materiais. III. Título

AGRADECIMENTOS

À Deus por sua presença incessante.

À minha família, em especial ao meu esposo Emanuel, minha mãe Vera Lúcia e meu irmão Tiago pelo apoio, incentivo, confiança e amor. Sem vocês não teria sido possível ir tão longe.

Ao meu orientador José Antônio e o corpo técnico do Labcorr pela oportunidade, convivência e ensinamentos.

Ao PEMM pelos dedicados professores e funcionários, inspiradores laboratórios e lindas amizades conquistadas.

Ao IFE pela acolhida amorosa e pela rica troca acadêmica e pessoal.

À 4Subsea pela parceria e memoráveis workshops.

À Shell, Petrobras e CNPq por ter apoiado e financiado esta tese.

Resumo da Tese apresentada à COPPE/UFRJ como parte dos requisitos necessários para a obtenção do grau de Doutor em Ciências (D.Sc.)

CORROSÃO POR CO_2 DE ARAMES DE AÇO DE ALTA RESISTÊNCIA NO ESPAÇO ANULAR DE DUTOS FLEXÍVEIS

Tatiane Seixas Campos

Maio/2022

Orientador: José Antônio da Cunha Ponciano Gomes

Programa: Engenharia Metalúrgica e de Materiais

A corrosão do aço carbono pode ocorrer em pH próximo do neutro em soluções desoxigenadas com alta concentração de íon bicarbonato quando há redução de hidrogênio atômico. Tais condições são encontradas no espaço anular de dutos flexíveis com água e CO_2 dissolvido, que produz alta concentração de íon ferroso (Fe^{2+}) e bicarbonato (HCO_3^-). O objetivo deste estudo foi investigar se altos níveis de Fe^{2+} e HCO_3^- podem persistir a ponto de induzir corrosão sob tensão (CST) em aços de armadura. Isso implica que a nucleação e o crescimento da siderita ($FeCO_3$) são tão lentos que a solução permanece supersaturada por vários dias. O papel do acabamento superficial e das áreas catódicas compostas por cementita também foram avaliados, assim como a salinidade, temperatura e pCO_2. Os resultados mostram que, abaixo de 40 °C e pCO_2 de 5 a 10 kPa, a razão de saturação (SR) da siderita pode persistir em valores muito superiores a 1 e manter pH próximo da neutralidade por várias centenas de horas. No entanto, a taxa de corrosão uniforme do aço de arame é baixa se o pH logo atingir a faixa neutra. A siderita forma uma camada na superfície do aço e a reação catódica torna-se limitada pela difusão. A taxa de corrosão aumenta com o aumento do teor de sal e cementita exposta, sendo ainda mais pronunciada a 25 °C. Nesses casos, a siderita não pode inibir completamente a corrosão localizada, o que pode ser um local de início de CST. Isso está relacionado com uma ação conjunta da maior solubilidade da siderita e o efeito do íon cloreto. A 25°C e salmoura, a pCO_2 é o principal parâmetro a ser considerado em superfícies ativas das armaduras de aço.

Abstract of Thesis presented to COPPE/UFRJ as a partial fulfillment of the requirements for the degree of Doctor of Science (D.Sc.)

CO_2 CORROSION OF HIGH STRENGTH STEEL WIRES IN THE ANNULUS OF FLEXIBLE PIPES

Tatiane Seixas Campos

May/2022

Advisor: José Antônio da Cunha Ponciano Gomes

Department: Metallurgical and Materials Engineering

Corrosion of carbon steel may occur at near neutral pH in deoxygenated solutions with high bicarbonate concentration when the corrosion reaction produces elemental hydrogen. Such conditions are encountered in the annulus of flexible pipes when it contains water with dissolved CO_2, which produces high concentration of ferrous ion (Fe^{2+}) and bicarbonate (HCO_3^-). The objective of the present study was to investigate if high levels of Fe^{2+} and HCO_3^- can persist for the time required to induce SCC in armor wire steels. It implies that the nucleation and growth of siderite ($FeCO_3$) is so slow that the solution remains supersaturated for several days. The role of surface finishing and cathodic areas composed of cementite were also evaluated, as well as the salinity, temperature, and pCO_2. The results show that, at temperatures lower than 40 °C and CO_2 partial pressure of 5 to 10 kPa, the saturation ratio (SR) of siderite can persist at values much higher than 1 and maintain a near neutral pH for several hundred hours. The uniform corrosion rate of armor wire steel is low if pH soon achieves near neutral range. The siderite forms a layer on the steel surface and the cathodic reaction becomes limited by diffusion through it. The corrosion rate increases with increasing salt content and exposed cementite, being even more pronounced at 25 °C. In such cases, siderite could not completely inhibit localized corrosion, which may be a great site for SCC cracks to start. That is related with a join action of the higher solubility of siderite and the effect of ion chloride. At 25°C and brine, the pCO_2 is the main parameter to concern in active surfaces of armor steels.

CONTENTS

LIST OF FIGURES viii
LIST OF TABLES xii
LIST OF SYMBOLS AND ABREVIATIONS xiii
1. INTRODUCTION 1
1.1. Offshore flexible pipes – the beginning of the concept 1
1.2. Flexible pipes configuration 2
1.3. The annulus environment 3
1.4. SCC at near neutral pH 5
1.5. Research objective 6
2 THEORY 7
2.1. Water acidification in presence of CO_2 7
2.2. CO_2 corrosion in annulus 9
2.3. Siderite formation 10
3. EXPERIMENTAL 16
3.1. Materials 16
3.2. Solutions 18
3.3. Test setups and procedures 18
3.3.1. Solid precipitation tests 18
3.3.2. Electrochemical tests 20
3.3.2.1. CO_2 corrosion in siderite supersaturated system 21
3.3.2.1.1. Effect of salinity and surface finish on steel wires 21
3.3.2.1.2. Siderite growth and the effect of exposed cementite 22
3.3.2.2. CO_2 corrosion at near neutral pH on film free surfaces 23
4. RESULTS AND DISCUSSION 26
4.1. Chemical evolution and morphological analysis of solid precipitation 26
4.2. Effect of as received layers and salt content on corrosion of armor wire steels 33
4.2.1. Corrosion in 0.1 wt.% NaCl solution 33
4.2.2. Corrosion in artificial seawater 38
4.3. Effect of exposed cementite on corrosion of armor wire steels 42
4.3.1. Cementite exposure at acidic stage 43
4.3.2. The effect of siderite precipitation on corrosion of armor wire steel 44
4.4. Corrosion in unfilmed samples 64
5. CONCLUSIONS 73
6. SUGGESTIONS FOR FUTURE WORK 75
7. REFERENCES 76

LIST OF FIGURES

Figure 1 – Map of Campos Basin, the first offshore oilfield that used flexible pipes in Brazil (adapted from (BORRE & COFFEY, 2014). 2

Figure 2 - Annulus configuration of flexible pipes presenting layers of tapes and armor steel wires in between the inner and the outer polymers (adapted from JHA et al., 2013). 3

Figure 3 - (a) Ferrous ion concentration ratio in relation to time at 25, 45, 55 and 65 °C (adapted from YEAN et al. (2008)). (b) Carbonate film growth rate as a function of temperature and at different levels of supersaturation (adapted from TOMSON et al. (1991). 14

Figure 4 - Diagram built from simulated data showing the influence of temperature and CO_2 partial pressure on the pH, $SR_{siderite}$ and Fe^{2+} at (a) distilled water; and (b) seawater. 14

Figure 5 - SEM images and EDS maps of iron (pink) and oxygen (green) of SEM images and EDS maps of iron (pink) and oxygen (green) of "as received" surface morphology of steel wires Type 1 (a); and Type 2 (b). 17

Figure 6 – SEM images of steel wires of (a) Type 1, (b) Type 2 and (c) Type 3 polished and etched with Nital (2%) to reveal the microstructure. (d) X65 standard specimen (Ref.) polished and etched in 3-4% picric acid in methanol with benzalkonium chloride (adapted from BERNTSEN (2017)). 17

Figure 7 -Test setup scheme for solid precipitation tests showing ferrous ion feeding unit filled with steel wool (on the left) and the test cell (on the right). 19

Figure 8 – Test setup scheme showing ferrous ion feeding unit filled with steel wool (on the left) and the test cell (on the right). The electrochemical electrodes and the immersion samples are in a close. 21

Figure 9 – Test setup scheme for electrochemical analysis of bare steels at acid and near neutral pH by $NaHCO_3$ addition. 24

Figure 10 - Measured and calculated parameters in the de-supersaturation experiments (a) measured pH; (b) measured Fe^{2+} concentration; (c) calculated saturation ratio for siderite

($SR_{(siderite)}$). The arrows show when the CO_2 partial pressure was decreased from 10 to 5 kPa (SW = artificial seawater solution, corr = tests with corrosion coupons). 31

Figure 11 - XRD spectra of the bulk precipitate formed at different temperatures and reference spectra of siderite, chuckanovite and NaCl (halite). 31

Figure 12 -Chemical stability diagram for Fe^{2+} and siderite ($FeCO_3$) at partial pressure of CO_2 equal to 9 kPa at 40 °C and 10 kPa at 10 °C (10% CO_2 in purging gas at 100 kPa total pressure). The solid lines give the Fe^{2+} solubility vs. pH at equilibrium at 40 °C (red) and 10 °C (blue). The dotted lines show the Fe^{2+} concentration vs. pH in the experiment with the start point at the high pH. 32

Figure 13 – OM and SEM images showing morphological differences among precipitates formed at 10, 15, 25 (with and without salt addition) and 40 °C. 33

Figure 14 - Corrosion rate of steels Type 1 and Type 2 with “machined” (M) and “as received” (AR) surface finish in 0.1 wt.% NaCl solution (25C_corr in Table 3). The close-up on the right shows the corrosion rate of the materials in the first 5 h. 34

Figure 15 - Development of potentiodynamic sweeps over time for “as received” surface finish Type 1 (a) and Type 2 (b) in 0.1 wt.% NaCl solution (25C_corr in Table 3). 35

Figure 16 - EIS plots for “as received” steels (a) Type 1, and (b) Type 2 tested in 0.1 wt.% NaCl solution (25C_corr in Table 3). 36

Figure 17 - SEM images of corrosion layers formed in 0.1 wt.% NaCl solution with high initial Fe^{2+} concentration and alkalinity (25C_corr in Table 3). (a) and (c) cross-sections of “as received” steels Type 1 and Type 2, respectively; (b) and (d) the surface of “as received” steels Type 1 and Type 2, respectively. 37

Figure 18 - Corrosion rate of “as received” steels Type 1 and Type 2 (25C_SW_corr in Table 3). The close-up on the right shows the corrosion rate of the materials in the first 5 h. 38

Figure 19 - Development of potentiodynamic sweeps over time for “as received” steels (a) Type 1 and (b) Type 2 in artificial seawater (25C_SW_corr in Table 3). 39

Figure 20 - EIS plots for “as received” steels (a) Type 1 and (b) Type 2 in artificial seawater (25C_SW_corr in Table 3). 40

Figure 21 - SEM images of corrosion layers formed in artificial seawater solution (25C_SW_corr in Table 3). (a) and (c) cross-sections of “as received” steels Type 1 and Type 2, respectively; (b) and (d) surfaces of “as received” steels Type 1 and Type 2 steel, respectively. 42

Figure 22 – Type 3 steel after acidic stage at 25 °C and 3.5 wt.% NaCl with a close-up on exposed cementite..... 44

Figure 23 - Pourbaix diagram Fe-H_2O-CO_2 at (a) 25 °C; and (b) 40 °C and 10 kPa pCO_2, varying salinity. 45

Figure 24 – Corrosion rate of the steel Type 3 analysing the effect of NaCl content and temperature of the system (a) with exposed cementite on steel surface; and (b) bare steel. 48

Figure 25 – $SR_{(siderite)}$ vs. time of the tests listed in Table 4. 50

Figure 26 - Measured values of OCP over time of sample Type 3. 50

Figure 27 – EIS plots showing the effect of film formation over time on corrosion of the steel Type 3 in different salinity and temperature. 53

Figure 28 – ECC used for modelling the impedance spectra recorded for (a) 3.5 wt.% NaCl; and (b) 0.1 wt.% NaCl. 54

Figure 29 – The effect of salinity and temperature on the precipitation and growth of siderite crystals over time in steel Type 3. 55

Figure 30 – Area covered by the siderite layer over time in steel Type 3 under different salinity and temperature (in %). 55

Figure 31 – SEM image of cross-sectioned sample Type 3 tested at 25 °C and 0.1 wt.% NaCl showing light siderite crystals (n. 2) encrusted in a dark layer of precipitates (n. 1). 58

Figure 32 – SEM image of cross-sectioned sample Type 3 tested at 40 °C and 0.1 wt.% NaCl showing an outer and darker layer (n. 1); an inner and lighter (n. 2); and areas presenting cementite (n. 3 and 4). 59

Figure 33 – (a) SEM image of cross-sectioned sample Type 3 tested at 25 °C and 3.5 wt.% NaCl showing localized corrosion. (b) SEM maps highlighting siderite formation and presence of element Cl in pit tip. 60

Figure 34 – (a) SEM image of cross-sectioned sample Type 3 tested at 40 °C and 3.5 wt.% NaCl showing localized corrosion. (b) SEM maps highlighting siderite formation and presence of element Cl in pit tip. 61

Figure 35 - Pourbaix diagram for the Fe-CI-H_2O system at 25 and 40 °C and 1.6 M NaCl. 62

Figure 36 – SEM images of stripped Type 3 steels tested at (a) 0.1 wt.%NaCl 25 °C; (b) 0.1 wt.%NaCl 40 °C; (c) 3.5 wt.%NaCl 25 °C; and (d) 3.5 wt.%NaCl 40 °C. 63

Figure 37 – Confocal microscopy showing depth profile of steel Type 3 tested in brine at (a) 25 °C; and (b) 40 °C, revealing pits. 63

Figure 38 – Corrosion rate of Type 3 steel during the acid stage (left), and at near neutral pH by the addition of $NaHCO_3$ (right). 66

Figure 39 – Nyquist and Bode impedance spectra recorded for the tests carried out in bare steels under conditions shown in Table 5. 67

Figure 40 – ECC for modelling the impedance spectra shown in Figure 39. 68

Figure 41 – Polarization sweeps for steel Type 3 during acidic stage (black), precipitation stage (red) and in presence of NaHCO3 (blue). (a) 0.1 wt.% NaCl at 25 °C; (b) 3.5 wt.% NaCl at 25 °C; (c) 0.1 wt.% NaCl at 40 °C; and (d) 3.5 wt.% NaCl at 40 °C. 70

Figure 42 – The effect of pCO2, alkalinity and pH on bare steels Type 2 and Ref. under near neutral pH. 72

LIST OF TABLES

Table 1 - Chemical compositions and mechanical properties of the tested steels (wt.%) (Fe in balance). 16

Table 2– Solid precipitation test matrix (corr = presence of carbon steel coupons, SW = seawater). 19

Table 3 – Experimental test matrix (total pressure 100 kPa) (corr = corrosion, SW = seawater, M = “machined”, AR = “as received”). 22

Table 4 – Summary of the tests carried out to analyse siderite growth and the effect of exposed cementite on electrochemical responses (i = initial). The solution with 3.5 wt.% NaCl is also called “brine” in this research. 23

Table 5 – Summary of test conditions in film free surfaces of Type 3 varying temperature and salinity (i = initial). 25

Table 6 – Summary of test conditions to calculate CR of the tested steels Type 2 and Ref. by varying pCO_2, alkalinity and pH in artificial seawater. 25

Table 7 - Calculated pH at siderite saturation as a function of temperature and CO_2 partial pressure in 0.1 wt.% NaCl and artificial seawater solution (SW). 29

Table 8 – EDS analysis in the areas indicated in Figure 32. 59

Table 9 - EDS analysis in the areas indicated in Figure 33. 59

Table 10 – CR of the tested steels Type 2 and Ref. by varying pCO_2, alkalinity and pH in artificial seawater. 73

LIST OF SYMBOLS AND ABREVIATIONS

σ - Relative supersaturation

ΔI – Current variation

Ω – Molecular volume

ΔE – Potential variation

B – Rate at which atoms are added to the core

a – Activity chemical

A – Pre-exponential fator

API – American piping products

ASTM – American Society for Testing and Materials

B – Stern-Geary constant

$C_{CO2(diss)}$ – Dissolved carbon dioxide

CE – Counter electrode

C_{H2CO3} – Ratio of carbonic acid

C_i – The concentration of *i* specie

CR – Corrosion rate

CST – Corrosão sob tensão

E_a – Activation energy

Ecorr – Corrosion potential

EDS – Energy dispersive spectroscopy

EIS – Electrochemical Impedance Spectroscopy

H – Henry constant

h – Interplanar space

I – Nucleation rate

icorr – Densisty current

IFP French institute of Pretroleum

K – Boltzmann constant

K – Equilibruim constants

K_i – Equilibruim constant

KSP - Solubility product constant

ln – Natural logarithmic

LPR – Linear polarization resistance

n – Number of molecules per volume

OCP – Open circuit potential

OM – Optical microscope

PA11 – Polyamide 11

PA12 – Polyamide 12

PCO_2 – Partial pressure of CO_2

pH – Potential of hydrogen

ppb – Portion per bilion

ppm – Partion per milion

PVDF – Poly (vinylidene fluoride)

Q_{dl} – Double layer capacitance

Q_f – Energy vibration

Q_p – Capacitance

r – Critical radius of crystal nucleation

RE – Reference electrode

Rp – Polarization resistance

Rp – Second resistance

Rs – Solution resistance

S – Surface area

SCC – Stress corrosion cracking

SEM – Scanning eléctron microscopy

SR – Saturation rate

SSRT – Slow strain rate testing

SW – Seawater

T – Temperature

v – Frequency of molecular vibration

V – Volume

WE – Working electrode

XRD – X-ray diffraction

1. INTRODUCTION

1.1.Offshore flexible pipes – the beginning of the concept

Although the application of flexible pipes is currently for commercial purposes in offshore oilfields, their technology began in World War II in Operation Overlord, in June 6, 1944, better known as D-Day. In the event, it was created as a mechanism capable of guaranteeing the fuel supply for the invading force in Normandy safely, regardless of the weather conditions. Through the cooperation between British scientists, oil companies and the armed forces, it was possible to develop a flexible pipeline linking the south-east of England to France. The installation was called Operation Pluto (Pipelines Under the Ocean) (JENSEN, 2010). Its success stimulated the creation of a new concept of transportation of oil and gas implemented years later.

The first attempt to introduce flexible pipes technology into the oil and gas industry happened in the 1960s supported by the French Petroleum Institute (SPARKS, 2007). They have developed a system of flexible pipes called *Fexoforage*. However, its application was suspended because its well sealing system was not considered safe in case of a possible breach. Even so, the development of flexible pipes for subsea continued. Years later, flexible pipes started to be used by *Coflexip*[1] in fields considered "mild" based on oceanographic studies (winds, waves and sea currents), such as those in the Campos Basin in Brazil (Figure 1), Far East and the Mediterranean. With the advancement of their technologies, flexible pipes started to be used in various fields of the North Sea and in the Gulf of Mexico, and continue being used to this day (BAI & BAI, 2010b, PALMER & KING, 2008).

[1] Company created by IFP (French Institute of Petroleum) specialized in design, manufacture and supply of flexible flow lines for underwater media. In the 2000s, they merged with Technip.



Figure 1 – Map of Campos Basin, the first offshore oilfield that used flexible pipes in Brazil (adapted from BORRE & COFFEY (2014)).

1.2. **Flexible pipes configuration**

Flexible pipes are based on a complex structure formed by overlapping metal and polymers. Although they require higher costs of production when compared to rigid pipes, in specific cases, flexible pipes can be considered economically viable due their ease of installation and greater flexibility in project adaptations. Additionally, they are durable, and allow to repair in the external coating in case of damage (REMITA *et al.*, 2008a).

The annulus consist of polymers, voids and armor layers between the bore and outer sheath (Figure 2) (BAI & BAI, 2010a). The armors are made of high strength carbon steel wires, designed to provide axial and tensile strength. They are enveloped by polymers, extruded or helically wrapped, which aim to isolate the wires from the internal (gases, oil and water) and also the external fluids (seawater), forming an occluded environment[2] between them (BATISTA *et al.*, 2007, RUBIN & GUDME, 2006, AMERICAN PETROLEUM INSTITUTE, 2008). The annulus is composed of about 70 percent by volume of armor steels, 0.5-1.5 mm apart. The ratio between the free volume and the surface area of metallic materials is generally up to 0.1 $mL.cm^{-2}$. The air and/or fluids injected into the voids during the manufacture are also part of the annulus (BERGE *et al.*, 2017, BAI & BAI, 2005, AMUNDSEN *et al.*, 2017).

[2] A space where solution and corrosive species can be trapped, or it is a thermodynamically closed system.

There is an immense variety of configurations to meet the requirements of each project, i.e., composition of the transported fluid, pressure, temperature, depth and mechanical demands. Their configuration may be designed for applications at depths up to 2500 m, pressure of approximately 680 bar, temperatures above 65°C and for adverse climatic conditions (SPARKS, 2007, BAI & BAI, 2010a). Thus, flexible pipelines emerged as a possibility to use in the Pre-Salt[3] in Brazil.

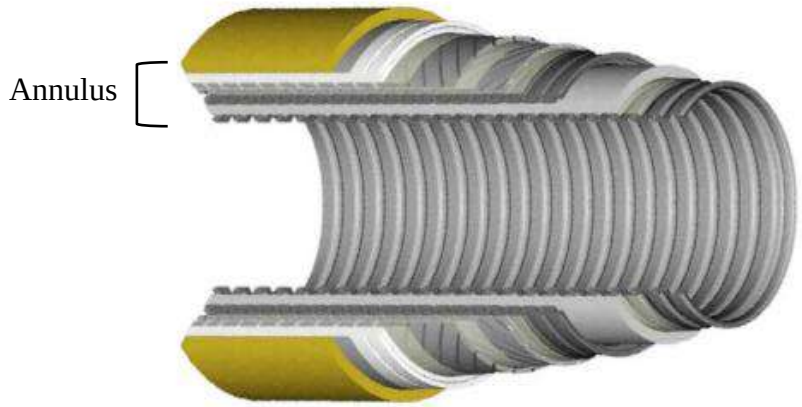


Figure 2 - Annulus configuration of flexible pipes presenting layers of tapes and armor steel wires in between the inner and the outer polymers (adapted from JHA *et al.*, 2013).

1.3. **The annulus environment**

A corrosive atmosphere may build up in the annulus of flexible pipes as a result of the permeation of transport, production or injection gases from the bore through the inner sheath, or seawater ingress due to damage to the outer sheath or improper sealing (DUGSTAD *et al.*, 2018, REMITA *et al.*, 2008a). The major challenge for industry is to predict the chemical composition and the electrochemical aspects. These data are important to determine the lifetime of the structure and minimizing risks and costs. The voids in the annulus may contain condensed water and gases permeating through the polymers. The permeation occurs when there is difference of partial pressure (chemical potential) of a fluid in contact with the polymer (PVDF, PA11, PA12) (RUBIN & GUDME, 2006). Only small molecules contribute significantly to the permeation through the polymers, such as methane (CH_4), carbon dioxide (CO_2), hydrogen sulphide (H_2S) and water (H_2O), coming from the bore of the structure. Seawater containing chloride,

[3] It is an oil-rich offshore reserve trapped beneath a 2000 m thick layer of salt.

calcium, magnesium and oxygen can also be present if there is any damage to the outer sheath or improper sealing. From there, an electrolyte is formed and electrochemical reactions start to present a corrosive potential in the presence of acid gases, such as CO_2 in contact with steel wires.

Corrosion in confined environments is commonly observed in localized corrosion cavities (pits, crevices, corrosion cracks, etc.). This configuration, where the volume limitation of the electrolyte must be considered, is also observed in the annulus of flexible pipes (REMITA *et al.*, 2008b, DUGSTAD *et al.*, 2020). Unlike the electrolytes considered infinite, the diffusion of species in confined environments generally affects corrosion mechanisms and accelerates its kinetics, causing a formation of massive corrosion products (REMITA, 2009, BAPTISTA, 1985). If they precipitate and are protective, the corrosion rate measured in the annulus usually presents 2 or 3 orders of lower magnitude than those predicted in classic models of CO_2 corrosion. As a result of the corrosion process, pH measurements tend to be significantly higher than those predicted in thermodynamic models, close to near neutral values (6.0 to 8.5) (CHEN *et al.*, 2002b, CEPA, 2015, JOHNSON *et al.*, 2000, CHEN, 2016, GU *et al.*, 1999, BEAVERS & JASKE, 1998). This is associated to the increase in alkalinity due to the accumulation of species from the dissolution of the iron in contact with the carbonic ions. This culminates in the precipitation of siderite ($FeCO_3$) at the interface between the electrolyte and the steel.

Under near neutral pH, the nucleation and growth of siderite often are the parameters controlling the corrosion rate of carbon steel in CO_2 environments. When siderite forms a dense and continuous layer on the steel surface, it acts as a diffusion barrier for the species that are produced or consumed by the corrosion process (DUGSTAD *et al.*, 2015, BERNTSEN *et al.*, 2013, SK *et al.*, 2017, MA *et al.*, 2018, SUN *et al.*, 2009, BURKLE *et al.*, 2017). In addition to the environmental conditions, the surface finish, chemical composition and microstructure of the steels affect the formation of the corrosion product films covering the steel surfaces. The adhesion of precipitated layers is commonly related to the presence, size and distribution of carbides in the steels, which are considered important "anchors" for a growing siderite film (DUGSTAD, 1998, FERREIRA *et al.*, 2016, LÓPEZ *et al.*, 2003a, CROLET *et al.*, 1998, DUGSTAD *et al.*, 2001, UEDA & TAKABE, 1999, TOMSON *et al.*, 1991, LIU *et al.*, 2015a, MORA-MENDOZA & TURGOOSE, 2002). The steels used in armor wires have a considerably high carbon

concentration and carbide content compared to rigid pipeline steels. If carbides play a key role in the corrosion mechanism, they may exhibit a different corrosion rate. It should also be noted that the armor wire steels develop adherent surface oxides in the manufacturing process, and these may also affect the corrosion reactions.

1.4. **SCC at near neutral pH**

The composition of trapped water in annulus is similar to the conditions that can induce SCC (stress corrosion cracking) in carbon steel, i.e. a relatively high bicarbonate concentration and a relatively low CO_2 partial pressure which result in a near neutral pH (ASHER *et al.*, 2007, J.A. COLWELL AND B.N. LEIS, 2005). The phenomenon was investigated in detail by National Energy Board in Canada where they found SCC in the external surface of buried pipelines in contact with soil in areas where the cathodic protection system did not work properly (MCCARTHY, 1997). The fractured surfaces were characterized as a quasi-cleavage; i.e., transgranular cracks, filled with corrosion products in the early stages, and followed by intergranular propagation of secondary cracks. The secondary cracks suggest that hydrogen produced by cathodic reactions plays a role in the cracking mechanism. The crack initiation process can start at defects where the hydrogen reduction rate is high.

At near neutral pH and under axial stresses, localized corrosion may act as crack initiation for SCC. This can be explained by the partial activation of the localized corrosion walls and local environment acidification. As a consequence, hydrogen may diffuse into the metal, creating intergranular and/or secondary cracks followed by primary transgranular cracks filled by corrosion products. That is, SCC at near neutral pH presents synergism of stress, hydrogen and anodic dissolution at the crack tip (TANG & CHENG, 2011).

Parkins and Zhou(PARKINS & ZHOU, 1997a) studied SCC of low carbon steels in CO_2-carbonate or bicarbonate solutions using slow strain rate tensile tests (SSRT). Transgranular cracks were associated with potential ranges where iron dissolves and intergranular cracking at electrochemical potentials where hydrogen discharge is possible. They also observed that crack growth increased with increasing HCO_3^- concentration, suggesting that HCO_3^- is directly involved in the crack mechanism.

1.5. **Research objective**

CO_2 corrosion of armor wire steels in the annulus of flexible pipes can create a solution containing high bicarbonate ion concentration and remain supersaturated with siderite for a substantial length of time leading to a near neutral pH. This may indicate the possibility of a total protective siderite film formation on the steel surface even at low temperatures (<40 °C), which is attributed to the peculiar spatial configuration of annulus (low V/S). However, if a partial siderite film forms, localized corrosion and hydrogen absorption are likely to occur.

The objective of this study was to investigate the conditions that can lead annulus to near neutral pH and the kinetics of siderite precipitation in such environments. Electrochemical responses and corrosion morphologies in armor wire steels were also studied. To do this, parameters that affect siderite precipitation and the corrosion processes were investigated, such as surface finishing, pCO_2, pH, salinity and temperature of the water. Thus, a better understanding of the chemical and electrochemical processes, and corrosion morphology in annulus are expected.

2 THEORY

2.1. Water acidification in presence of CO_2

The proposed mechanism of acidification of the water in presence of CO_2 involves four steps and the autoprotolysis of water. They are described below and are followed by their respective equilibrium constants (K). All reactions vary with the temperature according to the Arrhenius Equation (Equation 1), where *A* is a pre-exponential factor and E_a is the activation energy for nucleation (REMITA, 2009, FERREIRA *et al.*, 2016, YEAN *et al.*, 2008).

$$lnk = lnA - \frac{E_a}{RT} \quad \text{Eq. 1}$$

i. carbon dioxide dissolution

$$CO_{2(g)} \leftrightarrow CO_{2(diss)} \quad \text{Eq. 2}$$

The concentration of CO_2 (C_{CO2} (mol.mL^{-1})) in an ideal aqueous solution at equilibrium and at room temperature follows the Henry's Law (Equation 3), where H_{CO2} (mol.mL^{-3}.bar^{-1}) is the Henry constant for CO_2; and pCO_2 (bar) corresponds to the partial pressure of CO_2 in the gas phase.

$$C_{CO2(diss)} = H_{CO2}.pCO_2 \quad \text{Eq. 3}$$

ii. carbon dioxide hydration

$$CO_{2(diss)} + H_2O \leftrightarrow H_2CO_3 \quad \text{Eq. 4}$$

The equilibrium constant K_0 is dependent on temperature and the ionic strength of the solution. It is calculated by the ratio of carbonic acid (C_{H2CO3}) and dissolved carbon dioxide ($C_{CO2(diss)}$) concentrations in mol.mL^{-1}.

$$K_0 = \frac{C_{H2CO3}}{C_{CO2(diss)}} \quad \text{Eq. 5}$$

iii. first dissociation

$$H_2CO_3 \leftrightarrow H^+ + HCO_3^- \quad \text{Eq. 6}$$

Although this dissociation occurs according to the reaction described above, some authors, such as REMITA (2009), consider a directly dissociation from $CO_{2(diss)}$ due to the concentration of carbon dioxide dissolved in solution being difficult to measure. Thus, the reaction would be the expressed shown as below, followed by the equation of the equilibrium constant (K_1), where C_i (mol.mL^{-1}) is the concentration of *i* specie (Equation 8).

$$H_2O + CO_{2(diss)} \leftrightarrow H^+ + HCO_3^- \quad \text{Eq. 7}$$

$$K_1 = \frac{C_{H^+}.C_{HCO_3^-}}{C_{CO_{2(diss)}}} \quad \text{Eq. 8}$$

iv. second dissociation

$$HCO_3^- \leftrightarrow H^+ + CO_3^{2-} \quad \text{Eq. 9}$$

The second dissociation results in the formation of carbonate (CO_3^{2-}) from the dissociation of bicarbonate ion (HCO_3^-). The equilibrium constant of this reaction (K_2) is represented by Equation 10. As well as K_0, both, K_1 and K_2 are function of temperature, CO_2 pressure and ionic strength (IAEA, 2000).

$$K_2 = \frac{C_{CO_3^{2-}}.C_{H^+}}{C_{HCO_3^-}} \quad \text{Eq. 10}$$

v. autoprotolysis of water

$$H_2O \leftrightarrow OH^- + H^+ \quad \text{Eq. 11}$$

Finally, the dissociation of water follows the equilibrium condition according to Equation 12. It is important to note that although the proton is easily hydrated to form H_3O^+ or other hydrated ions, in this study all hydrated hydrogen ions will be represented only as H^+.

$$K_{H2O} = C_{OH-}.C_{H+} \quad \text{Eq. 12}$$

2.2. CO_2 corrosion in annulus

When CO_2 diffuses through the inner sheath to the annulus of flexible pipes, it maintains lower concentrations of CO_2 and carbonic acid in the water phase than in the bore[4]. However, substantial concentrations persist causing significant corrosion of the carbon steel wires. The corrosion mechanisms of dissolved CO_2 on carbon steels is extensively associated with the dissociation chain of the carbonic species, such as HCO_3^- and CO_3^{2-}, and the anodic dissociation of iron (DUGSTAD *et al.*, 2001, GRAY & ANDERSON, 1990, SUTCLIFFE *et al.*, 1972, PARKINS & ZHOU, 1997b, PENG & ZENG, 2015). The corrosion reactions are probably the same as encountered at higher CO_2 concentrations, but their relative contribution to the corrosion rate can be different (Equations 13-17).

$$2H_2CO_3 + 2e^- \rightleftarrows 2HCO_3^- + H_2 \quad \text{Eq. 13}$$

$$2HCO_3^- + 2e^- \rightleftarrows 2CO_3^{2-} + H_2 \quad \text{Eq. 14}$$

$$2H^+ + 2e^- \rightleftarrows H_2 \quad \text{Eq. 15}$$

$$2H_2O + 2e^- \rightleftarrows H_2 + 2OH^- \quad \text{Eq. 16}$$

$$Fe \rightleftarrows Fe^{2+} + 2e^- \quad \text{Eq. 17}$$

In pH < 7, CO_3^{2-} is the minority carbonic specie in the system. Then, HCO_3^- must to be considered as the precipitable ion and source of hydrogen, as described in Equations 18-20, where K is an equilibrium constant (CHEN *et al.*, 2002a, MORA-MENDOZA & TURGOOSE, 2002).

$$HCO_3^- = H^+ + CO_3^{2-} \quad \text{Eq. 18}$$

$$FeCO_3 + H^+ = Fe^{2+} + HCO_3^- \quad \text{Eq. 19}$$

$$K = \frac{a_{Fe^{2+}} \times a_{HCO_3^-}}{a_{H^+}} \quad \text{Eq. 20}$$

[4] Internal hole of flexible pipes for fluid transport.

In addition to the electrochemical reactions, the corrosive processes also involve mass transport through the solution. This is to fuel the cathodic reactions that take place in the interface metal solution and to bring the corrosion products into the bulk of the solution.

2.3. Siderite formation

Siderite is a solid product of CO_2 corrosion and is likely to be formed in the annulus. Its precipitation is often considered as the key parameter to reduce CO_2 corrosion kinetics in carbon steels. The reactions related to this process are shown in Equations 21-23 (HEUER & STUBBINS, 1999). Salinity, temperature, pH, exposure time and CO_2 partial pressure can influence corrosion process and film formation (PESSU *et al.*, 2020, FIORAVANTE *et al.*, 2019). When dense and uniform, the siderite acts as a diffusion barrier for the corrosive active species in the solution, leading to a decrease in the corrosion rate of the steel. Its nucleation and growth are controlled by the saturation rate ($SR_{(siderite)}$). When $SR_{(siderite)}$ is higher than 1 indicates that siderite precipitation is thermodynamically possible. $SR_{(siderite)}$ is a function of ferrous and carbonate ions activities and K_{sp}, as indicated in Equation 24 and 25, respectively (LÓPEZ *et al.*, 2003b).

Due to the particular geometry of the annulus, the K_{sp} of siderite, which is a function of ionic strength and temperature, may be easily exceeded even at low temperatures (< 40 °C). However, the formation of a siderite film with good protectiveness requires an expressive critical supersaturation (HONARVAR NAZARI *et al.*, 2010, BURKLE *et al.*, 2017, NEŠIĆ, 2007, DUGSTAD, 1998, KERMANI & MORSHED, 2003b). At the same time, the kinetics of siderite precipitation is so slow that $SR_{(siderite)}$ keeps values much higher than 1 for long time (CAMPOS *et al.*, 2021). Therefore, near neutral pH is possible in the annulus as the alkali components formed during the corrosion process, e.g. bicarbonate and/or carbonate ions, remain in solution even after of a massive siderite formation.

$$FeCO_3 = Fe^{2+} + CO_3^{2-} \quad \text{Eq. 21}$$

$$Fe^{2+} + 2HCO_3^- = Fe(HCO_3)_2 \quad \text{Eq. 22}$$

$$Fe(HCO_3)_2 = FeCO_3 + CO_2 + H_2O \quad \text{Eq. 23}$$

$$SR_{(siderite)} = \frac{a_{Fe^{2+}} \times a_{CO_3^{2-}}}{K_{sp}} \quad \text{Eq. 24}$$

$$K_{sp} = a_{Fe^{2+}} \times a_{CO_3^{2-}}$$ Eq. 25

The siderite precipitation basically occurs in three steps: supersaturation, nucleation and growth of the particles, being the latter the process that controls precipitation (DUGSTAD, 1998). This was analyzed by NEŠIĆ (2007) using experimental models. They reported that, regardless of the microstructure of the steels, nucleation is less crucial for the film formation and siderite growth. FERREIRA *et al.*, (2016) presented a model for siderite precipitation in a highly diluted solution. For them, heterogeneous nucleation occurs first in the substrate, followed by homogeneous nucleation inside the pores formed therein. Soon after, the process of crystalline film growth starts.

Siderite precipitation initiates from an instability in the solution due to the chemical potential the ions being higher than the ones present in the solid phase. Thus, to reduce the free energy of the system siderite forms, maintaining the concentration of balance of solution. Some authors, such as JIANG & TOSCA (2020), LIU *et al.* (2015b), believe that siderite crystals growth (R) presents a linear relationship with the relative supersaturation ($\sigma = SR_{(siderite)} - 1$) if $\sigma \geq 5$, while the nucleation rate (I) varies exponentially with σ, according to Equation 26 and 27, respectively. In the following equations h is the interplanar space, v is the frequency of molecular vibration, Q_f is the energy vibration, K is the Boltzmann constant, T is temperature, β is the rate at which atoms are added to the core, Ω s is the molecular volume, n is the number of molecules per volume , and r is the critical radius of crystal nucleation.

$$R = hv\ exp\left(\frac{-Q_f}{KT}\right)\sigma$$ Eq. 26

$$I = \beta n\ exp\left[\frac{-16\pi r^2 \Omega_s^2}{3k^3T^3\sigma^2}\right]$$ Eq. 27

However, as important as how siderite precipitates is how protective it can be to the steel corrosion process. According to DUGSTAD (1998) the protective effect of the film is inversely proportional to the degree of supersaturation in the system after siderite formation. The precipitation is accelerated by all parameters that restrict transport of surface reaction products such as viscosity, agitation and porosity. With proper adhesion, siderite minimize the transport of reagents and corrosion products, stabilizing pH and degree of supersaturation. There is a balance between corrosion rate, nucleation rate and transport speed. Therefore, it is assumed that to a protective siderite grow, the

precipitation rate must be higher than the corrosion. Otherwise, there is a higher probability of the film being porous and/or non-stick.

When in presence of seawater, precipitates in oilfield substrates can also include calcium, sodium, sulfate, magnesium and potassium products. The ion Ca^{2+}, for instance, can easily form calcite ($CaCO_3$) (Equation 28), which has greater solubility than siderite and contributes to the stability of a formed layer. Lower pH is also expected when Ca^{2+} is present (FERREIRA *et al.*, 2016). It is considered that calcite consumes part of the bicarbonate in electrolyte, causing a reduction in alkalinity, which increases, therefore, the solubility of Fe^{2+} (DUGSTAD *et al.*, 2018, ESMAEELY *et al.*, 2013, BERNTSEN *et al.*, 2013).

$$Ca^{2+} + CO_3^{2-} = CaCO_{3(s)} \quad \text{Eq. 28}$$

Moreover, the presence of ion chloride (Cl^-) can modify the corrosion mechanisms and products. In a solution with siderite, Cl^- can form intermediate products and $FeCl_2$, which increase the rate of anodic reaction and, thus, accelerate corrosion (Equations 29-32). This occurs because the small ionic radius of Cl^- allows it to spread among the solids and settle on the interface film/steel. Thus, the process of localized corrosion may occur (LIU *et al.*, 2015b, UEDA & TAKABE, 1999, PAUL *et al.*, 2014, KESAVAN *et al.*, 1989).

$$Fe^{2+} + 2Cl^- = FeCl_2 \quad \text{Eq. 29}$$

$$FeCl_2 + 2H_2O = Fe(OH)_2 + 2H^+ + 2Cl^- \quad \text{Eq. 30}$$

$$FeCl_2 + Cl^- = FeCl_3 + e^- \quad \text{Eq. 31}$$

$$Fe + 2H^+ = Fe^{2+} \quad \text{Eq. 32}$$

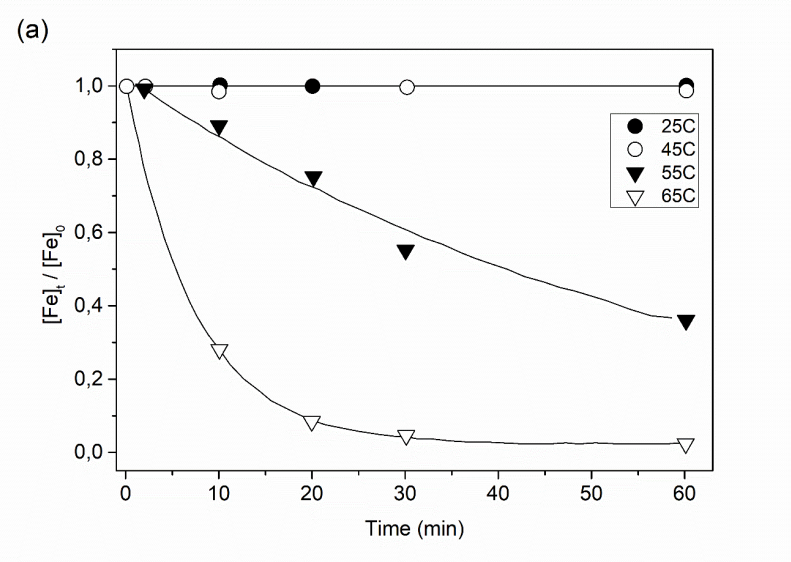
Besides the presence of salts, the presence of oxygen can occur depending on the depth of the outer sheath damage. This can directly affect the formation of siderite film, since it is generally formed under anaerobic conditions and appears unstable in the presence oxygen (DUGSTAD *et al.*, 2011). HEUER & STUBBINS (1999) analyzed the influence of oxygen in siderite films previously formed under anaerobic conditions for 48 h at 75 °C, presenting rhombohedral crystals and structures with low crystallinity as result. With the oxygen ingress, considering oxygen dissolved > 40 ppb, a rapid oxidation from

Fe^{2+} to Fe^{3+} occurs and the formation of a non-protective hematite (Fe_2O_3) is possible, as described in Equation 33 and 34.

$$FeCO_3 \rightarrow FeO + CO_2 \quad \text{Eq. 33}$$

$$4FeO + O_2 \rightarrow 2Fe_2O_3 \quad \text{Eq. 34}$$

The temperature and pressure influences CO_2 solubility and, consequently, the ionization of carbonic acid (H_2CO_3) and pH. Nevertheless, the protective films precipitation kinetics is directly affected by those factors, modifying the formation and properties of corrosion products, such as density, porosity and permeability. Low dissolved CO_2 reduces forces to cathodic reactions, increasing pH and $SR_{(siderite)}$, although the precipitation tends to be discontinuous and porous (KERMANI & MORSHED, 2003a). At high temperatures, the siderite solubility in solution is low, which increases the nucleation and growth rate (Figure 3) (SUN *et al.*, 2006). At lower temperatures (< 60 °C) there is a tendency for the solution remain supersaturated by corrosion products, and the layer formed on the substrate tends to be porous, heterogeneous and non-protective. Those characteristics may favor localized attacks. Any change in the parameters that increase precipitation kinetics (e.g. C_{Fe2+}, C_{HCO3-}, temperature and CO_2 partial pressure) can improve the crystallinity, adhesion and protectivity of the film (DUGSTAD, 1998, TOMSON *et al.*, 1991, UEDA & TAKABE, 1999, YEAN *et al.*, 2008). Figure 4 shows the influence of temperature and CO_2 partial pressure on the pH, $SR_{(siderite)}$ and Fe^{2+} in different salinity conditions at near neutral pH values, using simulated data.



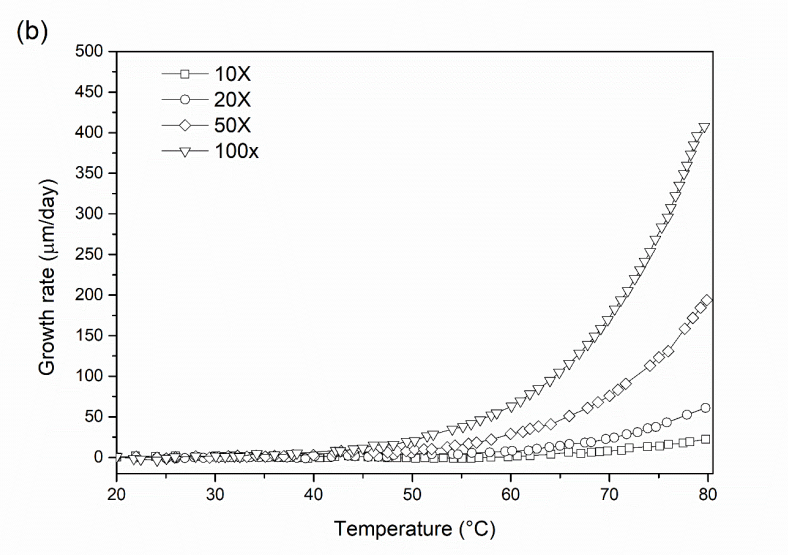


Figure 3 - (a) Ferrous ion concentration ratio in relation to time at 25, 45, 55 and 65 °C (adapted from YEAN *et al.* (2008)). (b) Siderite film growth rate as a function of temperature and at different levels of supersaturation (adapted from TOMSON *et al.* (1991).

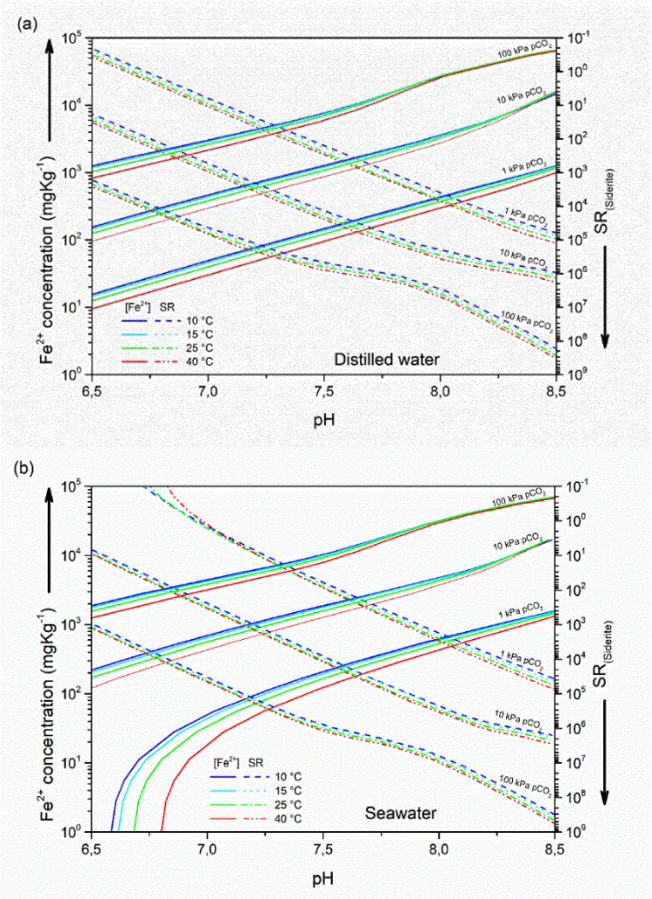


Figure 4 - Diagram built from simulated data showing the influence of temperature and CO_2 partial pressure on the pH, $SR_{(siderite)}$ and Fe^{2+} at (a) distilled water; and (b) seawater.

In addition to the environmental effects, it's known that chetablemical composition, microstructure and thermomechanical process of the steel may also affect the adhesion properties of the film, influencing the corrosion mechanisms (LÓPEZ *et al.*, 2003a, DUGSTAD *et al.*, 2000). In a steel composed by ferrite and cementite (Fe_3C), ferrite dissolves rapidly due to the lower electrical potential while cementite is not corroded by acting as a cathode site (LIU *et al.*, 2015b). Its surface usually presents grayish color, non-protective and porous character (FERREIRA *et al.*, 2016, LÓPEZ *et al.*, 2003a). As a consequence, cementite may be exposed on the steel surface as a result of CO_2 corrosion while siderite film is not formed, which increases the cathodic area and then intensify the corrosion process in anodic sites (ferrite) even after the film formation (MORA-MENDOZA & TURGOOSE, 2002). In such case, two distinct layers can form, the inner composed by cementite and siderite; and the outer, recrystallized on top of the first, forms only siderite (UEDA & TAKABE, 1999).

CROLET *et al.* (1998) said that the distribution of cementite layers can determine the protective factor of the film. The authors described the settings of protective corrosion products, where the siderite and cementite are in contact with the steel. It was attributed to the rapid saturation of Fe^{2+} in solution. If Fe^{2+} concentration takes place only after the initial stage of corrosion, only cementite forms in contact with the steel. In this case, the film is considered non-protective due to a significant galvanic couple formed between cementite and the metal, causing an internal acidification due to the reduction of H^+.

3. EXPERIMENTAL

3.1.Materials

The materials investigated in this study were three high strength carbon steels used in flexible pipes as tensile armor, called as Type 1-3, and a ferritic-pearlitic API X65 carbon steel as a standard for comparison called as Ref.

The exposed area, the chemical composition and mechanical properties of the test specimens are listed in Table 1. The surface finishes were as received from the fabrication process, referred to as "as received"; and machined and ground up to grit #1000 (FEPA P 1000) or #600 (ANSI 600), referred to as "machined". The layers on the surface of the "as received" wires Type 1 and Type 2 were analyzed by EDS (energy dispersive spectroscopy) after cleaned with isopropanol. On Type 1 steel, EDS results are consistent with the formation of iron oxide which in addition to Fe and O, contains Zn and traces of P (Figure 5 (a)). There are two phases at the surface of the "as received" Type 2 steel, that appear as light and dark areas in the picture in Figure 5 (b). The light phase contains Fe and C only, and is bare metal, while the dark phase is an iron oxide containing traces of Zn and Mn in addition to Fe, O and C.

Table 1 - Chemical compositions, mechanical properties and exposed areas of the tested steels for electrochemical and immersion tests (wt.%) (Fe in balance).

Material	Chemical composition (wt.%)								UTS (MPa)	Area (cm^2)
	C	Si	Mn	P	S	Cr	Ni	Mo		
Type 1	0.68	0.25	0.78	0.015	0.011	0.021	<0.015	0.003	1310	8.96
Type 2	0.66	0.24	0.76	0.018	0.018	0.043	0.02	0.005	1237	11.68
Type 3	0.51	0.22	0.73	0.010	0.007	0.03	0.02	<0.01	1200	3.60
Ref.	0.08	0.25	1.54	0.001	0.019	0.04	0.03	0.01	-	3.14

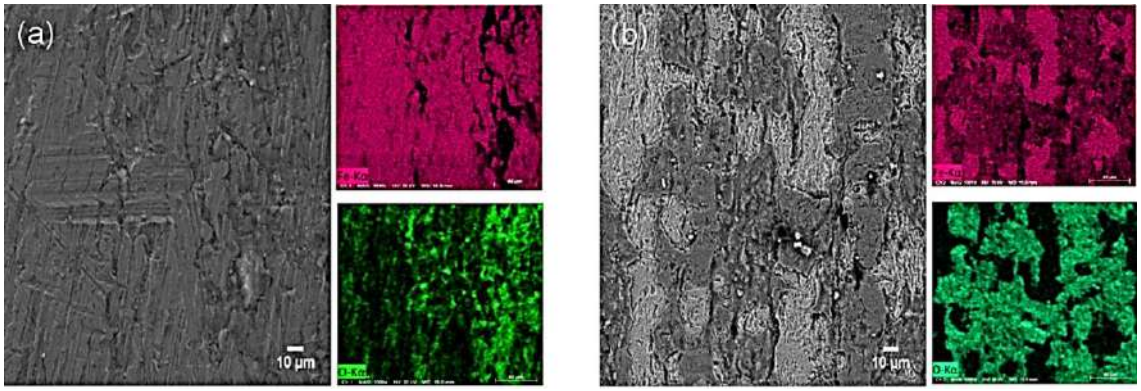


Figure 5 - SEM images and EDS maps of iron (pink) and oxygen (green) of SEM images and EDS maps of iron (pink) and oxygen (green) of “as received” surface morphology of steel wires Type 1 (a); and Type 2 (b).

For machined samples Types 1-3 and Ref., after being ground up using silicon carbide grit paper and prior to start the tests, they were cleaned with acetone then isopropanol in an ultrasonic bath. The steel microstructures are shown in Figure 6. By presenting carbon content close to the eutectoid composition, in wt.%, pearlite phase occurred almost exclusively in the armor wire steels with few ferrite islands. The Ref. exhibited a ferritic-pearlitic microstructure.

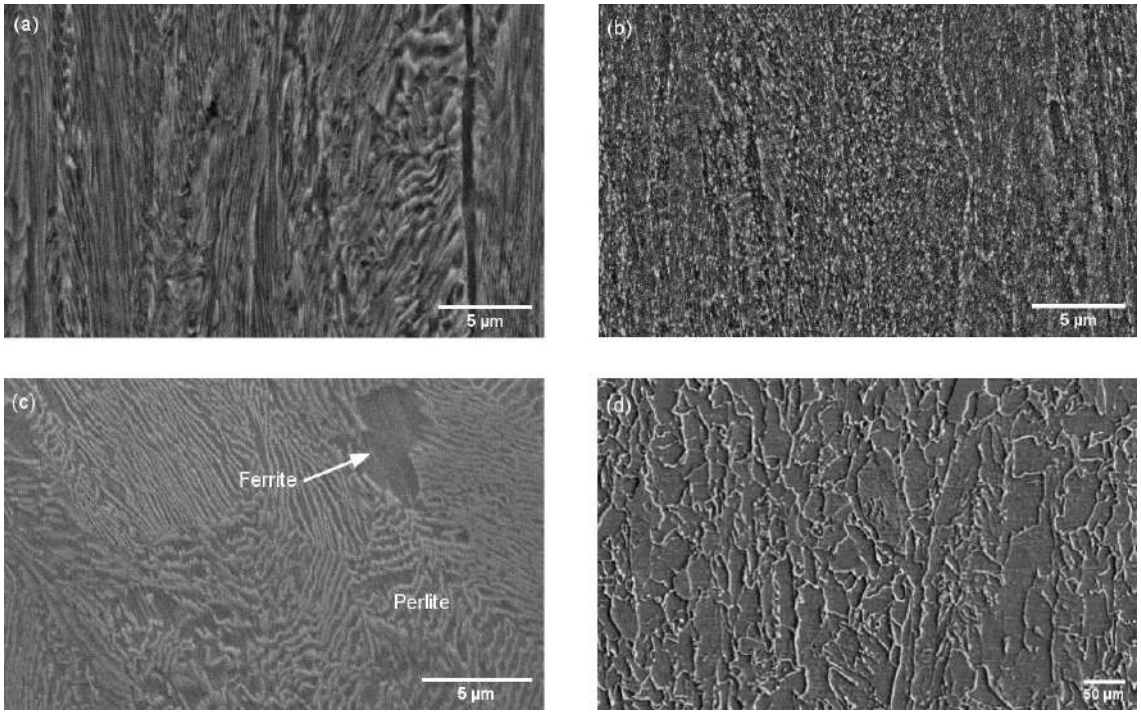


Figure 6 – SEM images of steel wires of (a) Type 1 (deformed pearlite), (b) Type 2 (spherozided carbides in ferrite matrix) and (c) Type 3 (pearlite with poligonal eutectoid ferrite (PF)) polished and etched with Nital (2%) to reveal the microstructure. (d) X65 standard specimen (Ref.) polished and etched in 3-4% picric acid in methanol with benzalkonium chloride (adapted from BERNTSEN (2017)).

3.2. **Solutions**

The test solutions – condensed water, water with 0.1 and 3.5 wt.% NaCl, and artificial seawater based on ASTMD1141 (2003) - were prepared using distilled water and 99% purity salts. The N_2 and CO_2 used for deoxygenation and purging during the experiments were 99.999% pure.

3.3.**Test setups and procedures**

3.3.1. Solid precipitation tests

The test setup for solid precipitation and solution evaluation consisted of a ferrous ion feeding unit and a test cell, as shown in Figure 7. The test cell was a 1 L jacketed glass reactor heated by a thermostatic bath. A thermoelement (Pt-100) placed in the cell was used to control the temperature within ±1 °C of the test temperature.

A feeding solution was prepared in the ferrous ion feeding unit with a capacity of 3 L. The unit was loaded with steel wool, deoxygenated solutions (0.1 wt.% NaCl or artificial seawater) and purged with CO_2 at 100 kPa. The steel wool corroded to give a solution with the required Fe^{2+} concentration. By keeping the liquid at 5-12 °C, it was possible to avoid siderite precipitation and maintain it highly supersaturated. Aliquots of the feeding solution were transferred to the test cell to give approximately 20 $mmol.kg^{-1}$ Fe^{2+} (1100 $mg.kg^{-1}$) and 40 $mmol.kg^{-1}$ alkalinity. The actual concentration was measured in all experiments.

The pressure in the test cell was 100 kPa and total gas flow rate was 200 $mL.min^{-1}$. The flow rate and the N_2 to CO_2 ratio in the gas was controlled by mass flow meters to give a CO_2 partial pressure of 9-10 or 5 kPa. The objective was to evaluate how changes in CO_2 partial pressure during the tests influence pH, $SR_{(siderite)}$ and Fe^{2+} concentration. Table 2 summarizes the conditions for the solid precipitation tests. The temperatures varied among 10, 15, 25 and 40 °C. The testes were carried out in 0.1 wt.% NaCl. However, at 25 °C the effect of seawater and the presence of corrosion coupons (tests that use the suffix "corr") in relation to the chemical evolution of solution were also evaluated. These corrosion coupons were inserted to monitor the corrosive behavior of the armor wire steels Type 1 and 2 at different salinities, whose procedure is described in item 3.3.2.1.1.

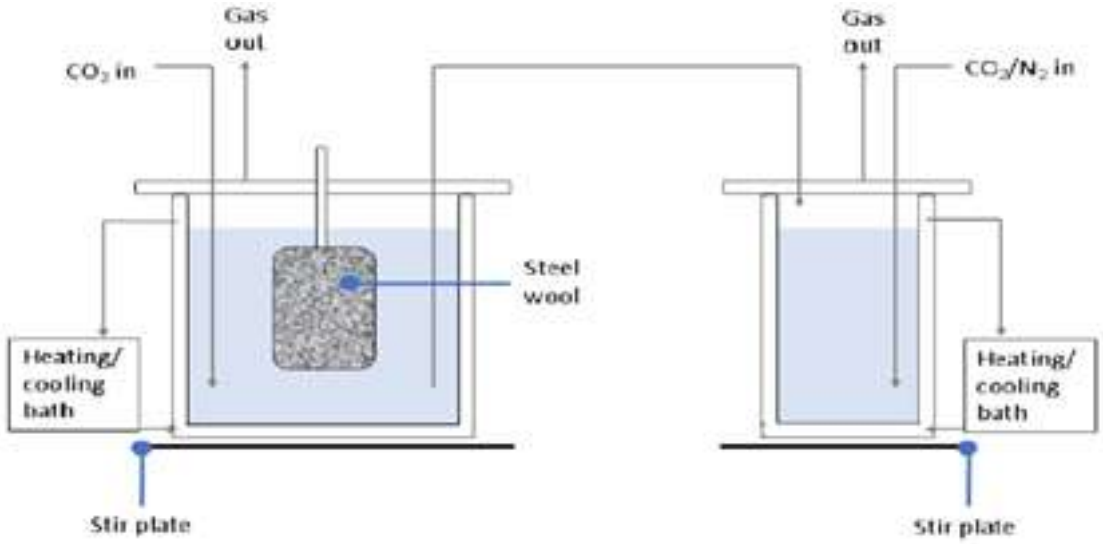


Figure 7 -Test setup scheme for solid precipitation tests showing ferrous ion feeding unit filled with steel wool (on the left) and the test cell (on the right).

Table 2– Solid precipitation test matrix (corr = presence of carbon steel coupons, SW = seawater).

Experiment	Initial conc. (mmol.kg^{-1})		CO_2 in gas (%)	T (°C)	Salt content
	[Fe^{2+}]	Alkalinity			
10C	18.50	37.00	10 to 5	10	0 wt.% NaCl
15C	18.20	36.40	10 to 5	15	0 wt.% NaCl
25C	18.54	37.08	10	25	0 wt.% NaCl
25C_corr	20.05	40.10	10	25	0.1 wt.% NaCl
25C_SW_corr	18.00	36.00	10	25	Artificial SW(ASTMD1141, 2003)
40C	21.45	42.90	10 to 5	40	0 wt.% NaCl

The pH was monitored throughout the tests using a data logger. The solutions were sampled for analysis every 1-3 days. The samples from the test cell and the ferrous ion feeding unit were filtered through 0.1 µm filters immediately after sampling. The dissolved Fe^{2+} was complexed as iron phenanthroline, and the concentration was measured by UV/visible spectrometry.

Temperature, pressure, and compositions of the gas and brine were used as input parameters in the MultiScale® 8.1 simulation software to estimate: CO_2 fugacity, pH, alkalinity speciation and siderite saturation ratio. The initial alkalinity was twice the Fe^{2+} concentration plus the alkalinity in the seawater. As shown by Equation 35, an alkalinity to Fe^{2+} ratio of two will be maintained when siderite precipitate in the 0.1 wt.% NaCl solution. The ratio will be somewhat different in the seawater experiments due to the

additional alkalinity and because calcium can precipitate as $CaCO_3$ or be incorporated in the siderite. The calculations take the corresponding alkalinity consumption into account.

$$Fe^{2+} + 2HCO_3^- = FeCO_3 + CO_2 + H_2O \quad \text{Eq. 35}$$

At the end of each experiment, the solid sediments in the test cell were collected and dried in the same gas mixture as used during the tests. The methods used for analyzing the dry solids were optical microscope (OM), scanning electron microscopy (SEM), energy dispersive spectroscopy (EDS), and x-ray diffraction (XRD). The scan range of the XRD spectra was 10 θ to 90 θ with step size 0.2 θ and holding time 12 s.

3.3.2. **Electrochemical tests**

Electrochemical measurements were performed in a 3-electrode set-up; with the carbon steel samples as working electrodes (WE), titanium wire as counter electrode (CE) and Ag/AgCl (3 M KCl) as reference electrode (RE).

The corrosion rate was determined by LPR and weight loss. The LPR scans were conducted every 30 min at 0.1 $mV.s^{-1}$, from -5 to +5 mV relative to the open circuit potential (OCP). The corrosion current density was calculated according to the Stern-Geary equation (Equation 36):

$$i_{corr} = \frac{B}{R_p A} \quad \text{Eq. 36}$$

where A is the specimen area; Rp is the polarization resistance (Equation 37), that is the ratio between the potential variation (ΔE) and current (ΔI); and B is the Stern-Geary constant calibrated based on the weight loss measured, or Tafel curves. When the material weight loss could not be used, i.e. for the "as received" coupons, nor even Tafel curves, the B value was set to 20 mV, the average value obtained for the "machined" specimens.

$$R_p = \frac{\Delta E}{\Delta I} \quad \text{Eq. 37}$$

Cathodic polarization sweeps were performed throughout the tests by varying the potential from +5 to -300 mV relative to OCP, at 0.1 $mV.s^{-1}$ sweep rate. Anodic polarization sweeps from -5 to +50 mV vs. OCP were done at the end of each test.

All polarization measurements were corrected for the solution resistance (R_s) determined by EIS. The EIS measurements were performed immediately before the cathodic sweeps. The frequency range was 0.05 to 10000 Hz, the AC voltage was 10 mV vs. OCP, and 6 points were recorded per decade.

3.3.2.1.**CO_2 corrosion in siderite supersaturated system**

The configuration and procedures for the electrochemical tests in siderite supersaturated systems were similar to those used in the solid precipitation tests, except for having electrochemical electrodes to corrosion tests and a test cell capacity of 3 L. Electrical wires were connected to some samples to provide connection with the potentiostat for electrochemical measurements in a regular 3-electrodes setup, as highlighted in Figure 8.

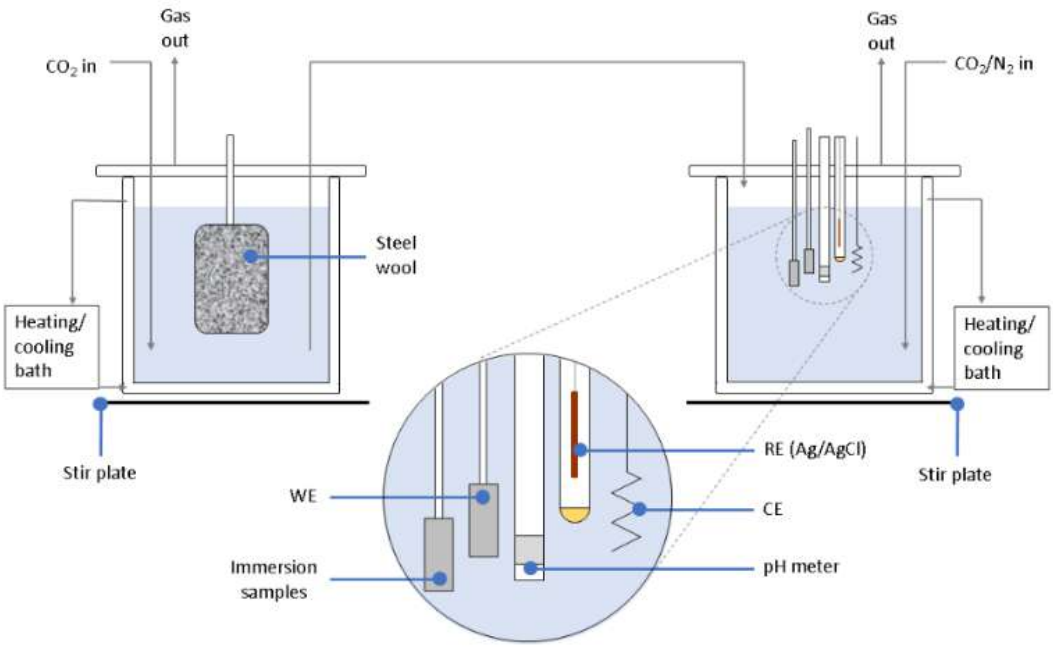


Figure 8 – Test setup scheme showing ferrous ion feeding unit filled with steel wool (on the left) and the test cell (on the right). The electrochemical electrodes and the immersion samples are in a close.

3.3.2.1.1. Effect of salinity and surface finish on steel wires

The effect of surface finishing ("M" = machined or "AR" = as received) of materials Type 1 and Type 2 was analyzed in 0.1 wt.% NaCl solution (25C_corr), at 25 °C and 10 kPa pCO_2. The corrosion behaviors of both AR samples were also evaluated in artificial seawater (25C_SW_corr). Table 3 summarizes the tests conditions.

The potentiostat was a Gamry® PCI 4 with multiplexer ECM 8 and the measurements were linear polarization resistance (LPR), potentiodynamic sweeps and electrochemical impedance spectroscopy (EIS). The working electrodes were inserted when the temperature and pH were stabilized after adding the concentrated Fe^{2+} solution.

At the end of each experiment, the corrosion coupons were rinsed with isopropanol and dried in an oven ventilated with N_2 at 60 ° for approximately 24 h. The methods used for analyzing the corrosion coupons were SEM and EDS.

Table 3 – Experimental test matrix (total pressure 100 kPa) (corr = corrosion, SW = seawater, M = "machined", AR = "as received").

Experiment	Initial conc. (mmol.kg^{-1})		CO_2 in gas (%)	T (°C)	Salt content	Steels tested
	[Fe^{2+}]	Alkalinity				
25C_corr	20.05	40.10	10	25	0.1 wt.% NaCl	Type 1 and Type 2 (M, AR)
25C_SW_corr	18.00	36.00	10	25	Artificial SW	Type 1 and Type 2 (AR)

3.3.2.1.2. Siderite growth and the effect of exposed cementite

To investigate the influence of exposed cementite as a consequence of corrosion process, the machined Type 3 steel went through a previous step called "acidic stage". The acidic stage consisted by immersing the samples into the solution without corrosion products. As a consequence, the pH remained approximately 5 during such periods, which provided the preferential corrosion of ferrite and exposure of cementite in pearlite. After about 12 h of the acidic stage, a system of pumps was used to replace the solution by the one produced in ferrous ion feeding unit, initiating the second step at near neutral pH called "precipitation stage". Table 4 presents a summary of the steps and conditions of the tests.

The addition of corrosion products in the system intended to identify the formed corrosion products morphologies at different salt content and temperatures, and their effect on the protection of the samples. By comparison, fresh samples were inserted as soon as the precipitation stage started to analyze the effect of the exposed cementite formed during the acidic stage on the corrosion responses.

For electrochemical measurements a potentiostat PalmSens® 3 with multiplexer was used, but for OCP monitoring, that used a Gamry® PCI 4 with multiplexer ECM 8. SEM images determined the growth of siderite crystals after 2, 4, 8 and 24 hours of exposure time to both acidic and precipitation stages. At the end of each experiment, the corrosion

coupons were rinsed with isopropanol and dried with hot air. An image processing software (ImageJ®) was used to measure the area covered by siderite in each image. This was done by manually covering the siderite crystals with a secondary layer. When isolated from the original one, it allowed the measurement of surface area covered by siderite. Only particles larger than 1 μm^2 were considered. To evaluate the corrosion morphologies, the samples were stripped using Clark solution, according to standard ASTM G1-03 (2017) and then cleaned with acetone followed by isopropanol in an ultrasonic bath. SEM and Confocal microscopy favored the analysis of the stripped samples. In cross section samples, EDS identified atoms present in localized corrosion morphologies.

Pourbaix-type diagrams, plots of the equilibrium potential of electrochemical reactions against pH, were built from Nernst equation to predict and better understand the corrosion mechanisms of armor wire steels related to pH, temperature and concentration of reacting species.

Table 4 – Summary of the tests carried out to analyse siderite growth and the effect of exposed cementite on electrochemical responses (i = initial). The solution with 3.5 wt.% NaCl is also called "brine" in this research.

T (°C)	**CO_2 in gas phase (bar)**	**NaCl content (wt.%)**	**Acidic stage (h)**	**Precipitation stage**	
				Time (h)	$c[Fe^{2+}]_i$ ($mg.Kg^{-1}$)
25	0.1	0.1	12	80	1020
40	0.1	0.1			1100
25	0.1	3.5			1050
40	0.1	3.5			1038

3.3.2.2.CO_2 corrosion at near neutral pH on film free surfaces

To analyze the corrosion behavior of surface-active steel wires at near neutral pH, $NaHCO_3$ was added in the test cell with corrosion coupons to avoid the formation of siderite. The test setup is shown in Figure 9.

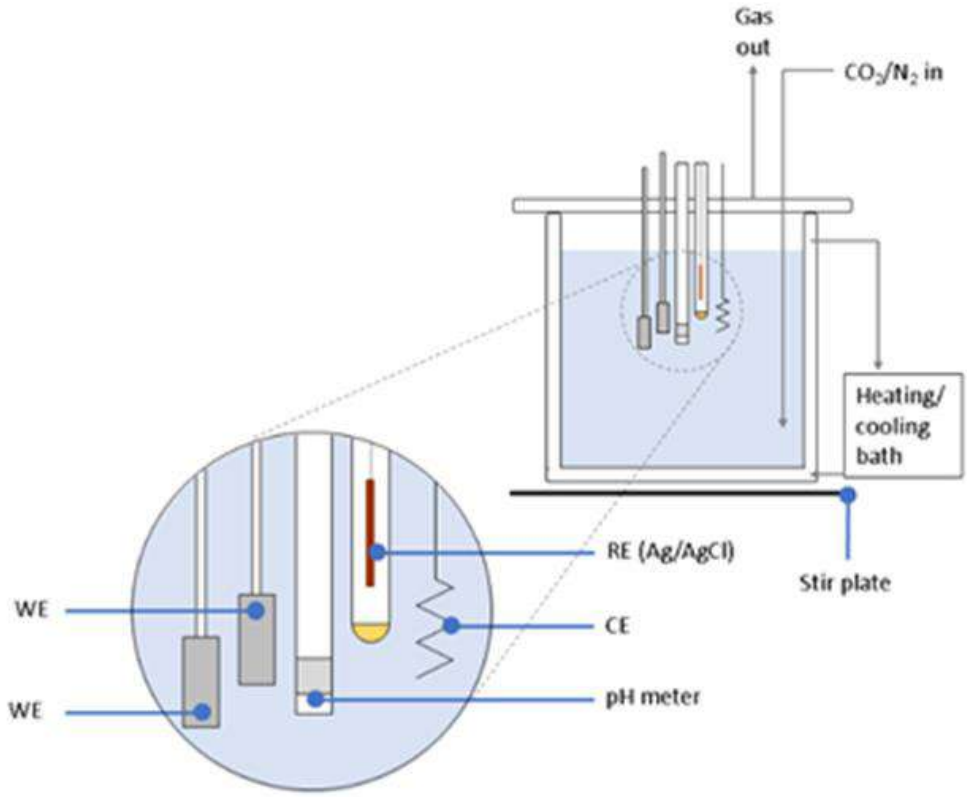


Figure 9 – Test setup scheme for electrochemical analysis of bare steels at acid and near neutral pH by $NaHCO_3$ addition.

Two distinct experimental procedures were performed. The first analyzed the effect of temperature (25 and 40 °C) and salinity (0.1 and 3.5 wt.% NaCl) on machined steel Type 3 previously submitted to the acid stage for cementite exposure. The test conditions are shown in Table 5. For electrochemical measurements a PalmSens® 3 with multiplexer was used.

The tests which conditions are shown in Table 6 were performed on machined steel Type 2 and were compared with machined API X65 (Ref.). The potentiostat was a Gamry® PCI 4 with multiplexer ECM 8 and the measurements were LPR, EIS and polarization sweeps. All tests were carried out at 25 °C in artificial seawater without Ca, Sr and Mg to avoid the reduction of the alkalinity due to precipitation. In this set of tests, the pCO_2, alkalinity and pH varied although they remained near to neutral in order to identify the effect of such variables on the active surface (without film) in both steel kinds.

Table 5 – Summary of test conditions in film free surfaces of Type 3 varying temperature and salinity (i = initial).

T (°C)	**CO_2 in gas phase (kPa)**	**NaCl content (wt.%)**	**Acidic stage (h)**	**Corrosion of free film surface tests**
				Initial c[HCO_3^-] (mmol.Kg^{-1})
25	10	0.1	18	36
25		3.5		
40		0.1		
40		3.5		

Table 6 – Summary of test conditions to calculate CR of the tested steels Type 2 and Ref. by varying pCO_2, alkalinity and pH in artificial seawater.

pH	**$NaHCO_3$ (mmol.kg^{-1})**	**pCO_2 (kPa)**
7.07	100	40
8.10	100	4
7.04	10	4
7.01	23	10
6.40	23	40
7.90	230	10

4. RESULTS AND DISCUSSION

4.1. Chemical evolution and morphological analysis of solid precipitation

The pH and Fe^{2+} concentration evolution over time at the different test temperatures are shown in Figure 10 (a) and (b), respectively. Figure 10 (c) shows the saturation ratio of siderite. The curves demonstrate how the precipitation rate decreases with decreasing temperature, due to the reduction of slopes with time. At 40 °C the Fe^{2+} concentration reached 100 $mg.kg^{-1}$ in 24 h, while it did not stabilize in 500 h at 10 °C. Changing the CO_2 partial pressure from 10 to 5 kPa, led to an immediate increase in pH, but it had marginal effect on the precipitation rate. The calculated pH if siderite precipitates to equilibrium is given in Table 7. The final pH at 150 to 500 h is higher at all temperatures. At 40 °C the difference is ca. 0.3 pH while it is ca. 1 pH at 10 °C.

The pH decreased as the solids precipitated. The decline is larger the higher the temperature (Figure 10 (a)). There was an immediate pH increase when the CO_2 partial pressure changed from 10 to 5 kPa, followed by a slow decline with time. Comparing the measured and equilibrium pH (Table 7) shows that the precipitation did not reach equilibrium and that the deviation increased with decreasing temperature. At 10 °C the pH after 350 h was 7.1 when the CO_2 partial pressure was 10 kPa, and after reducing the CO_2 partial pressure to 5 kPa, the pH only decreased from 7.4 to 7.2 in another 150 h. The pH followed the same pattern in the experiment at 15 °C. There were three experiments at 25 °C with some spread in the results. The spread is partly due to different conditions, i.e., seawater vs. 0.1 wt.% NaCl and with and without corrosion coupons. However, the stochastic nature of the solid precipitation will also give differences between parallel experiments. The pH after 150 to 250 h at 25 °C and 10 kPa CO_2 was 6.6 to 6.8. At 40 °C the pH decreased to 6.4 in 150 h at 9 kPa CO_2 and after reducing the CO_2 partial pressure to 5 kPa, it decreased from 6.7 to 6.6. The results show that solid precipitation in siderite supersaturated water is so slow, and that near neutral pH can be maintained for weeks at low temperature and low CO_2 partial pressure (BRAUN, 1991).

The faster pH decrease rate in the experiment in seawater (SW) than in low salinity solution at 25 °C with corrosion coupons, is an indication that $CaCO_3$ may precipitate initially. If it happens, it will give a lower $SR_{(siderite)}$ as indicated by the 25C_Corr_SW

curve in Figure 10 (c). However, it should be noted that the higher ionic strength of the seawater has a significant effect on the activity coefficient of Fe^{2+}.[42]

XRD analysis of the solid products collected at the end of the exposures confirmed that the precipitate was mainly siderite for all test conditions, see Figure 11. Chukanovite ($Fe_2(OH)_2CO_3$) was also detected in the solids formed at 25 °C (0.1 wt.% NaCl) and 40 °C. Some studies[43-46] claim that chukanovite is metastable and transforms to siderite depending on Fe^{2+} concentration, pH and CO_2 partial pressure, while others[21] consider that chukanovite follows siderite in the crystallization chain. NaCl was also detected in the solids from the artificial seawater experiment. It precipitates when the water dries up. None of the $CaCO_3$ polymorphs were identified in the solids collected from the experiments with seawater, so Ca^{2+} may have substituted Fe^{2+} in siderite rather than forming a separate phase. There is a slight shift to the left in the peaks in the XRD spectrum which is an indication of this.

The Fe^{2+} consumption due to precipitation was characterized by an initial fast concentration decay, followed by a slow decline (Figure 10 (b)). It may indicate a homogeneous nucleation due to high supersaturation initially and a subsequent slow growth of the suspended particles (JIANG & TOSCA, 2019, 2020). The solids did not precipitate at the cell walls initially, so heterogeneous nucleation is less likely. At 10 °C, the Fe^{2+} concentration was nearly constant for a few hours before it started to decrease. At 40 °C the Fe^{2+} concentration decreased to 120 $mg.kg^{-1}$ in less than 20 h. At 10 and 15 °C there was a slight, but evident decrease in Fe^{2+} concentration following the CO_2 partial pressure reduction to 5 kPa, occurring at ca. 350 and 220 h, respectively. The supersaturation increased immediately after the CO_2 reduction, before it continued to decrease at a slightly higher rate. Whether the higher precipitation rate at the higher SR is due to faster growth of the precipitated solids or new nucleation cannot be inferred.

The Fe^{2+} concentration and $SR_{(siderite)}$ decreased when CO_2 partial pressure was lowered at 40 °C (Figure 10 (b)), but did not reach equilibrium. The $SR_{(siderite)}$ remained at ca. 10. Accordingly, the pH was about 6.6, while the theoretical equilibrium value given in Table 7 is 6.18. A deviation at this order of magnitude may be caused by measuring errors, e.g. insufficient filtering, and inaccurate software, as discussed below. Besides, the filters had pore size 0.1 µm, so smaller particles may slip through. For the software, it is noted that the solubility product it predicts is slightly higher than recently published values ($logK_{SP}$

= -10.4 rather than -10.9 at 25.4 °C).[41] It should also be noted that formation of metastable chukanovite which did not transform to siderite, may also contribute to the high SR. Chukanovite was only observed in one experiment at 25 °C and at 40 °C.

The solubility of siderite is given in the chemical stability diagram in Figure 12. The diagram is for the initial CO_2 partial pressure applied in the experiments (9 kPa at 40 °C and 10 kPa at 10 °C). The evolution of Fe^{2+} concentration and pH in the experiments are overlapped in the diagram. The analysis clearly demonstrates that siderite has not precipitated to the estimated equilibrium. In the 40 °C experiment, the deviation is ca. 1 decade in $SR_{(siderite)}$ and 0.5 pH units at the end of the period with CO_2 partial pressure 10 kPa. The 10 °C experiment is far from the predicted equilibrium at the end (350 h). The results of experiments at 25 °C fall between the two extremes.

Both experimental errors and uncertainties in the calculations may contribute to overestimated $SR_{(siderite)}$ values. In addition to the small particles that may have slipped through the filters (< 0.1 µm), the formation of Fe^{2+} based complexes or ion pairs not included in the calculations, cannot be excluded. Both factors will result in an overestimation of Fe^{2+} concentration and alkalinity giving a high $SR_{(siderite)}$. The filtering error was minimized by letting the solution settle and sample the solution close to the surface. If stable complexes or ion pairs formed, one should expect that the Fe^{2+} concentration should reach a stable value, which was not the case. Such species would also tie up HCO_3^-, CO_3^{2-} and/or OH^- in the solution and thus decrease the pH. That was not observed, on the contrary, the pH was higher than estimated. It is concluded that complexes or ion pairs have marginal effect on the results. Filtering limitations may explain the deviation in $SR_{(siderite)}$ at 40 °C, but at the lower temperatures it is believed that the supersaturation was significant till the end of the experiments.

For the electrochemical studies presented in Item 4.2, two experiments were carried out in presence of corrosion coupons at 25 °C and 10 kPa CO_2, one with 0.1 wt.% NaCl and one with artificial seawater. The presence of solid $CaCO_3$ (expected to form in artificial seawater) and corroding surfaces may serve as sites for heterogeneous siderite precipitation, boosting its nucleation rate. However, the difference in de-supersaturation rate at 25 °C (Figure 10(c)) is not sufficient to conclude that presence of Ca^{2+} or corroding steel affects the precipitation rate.

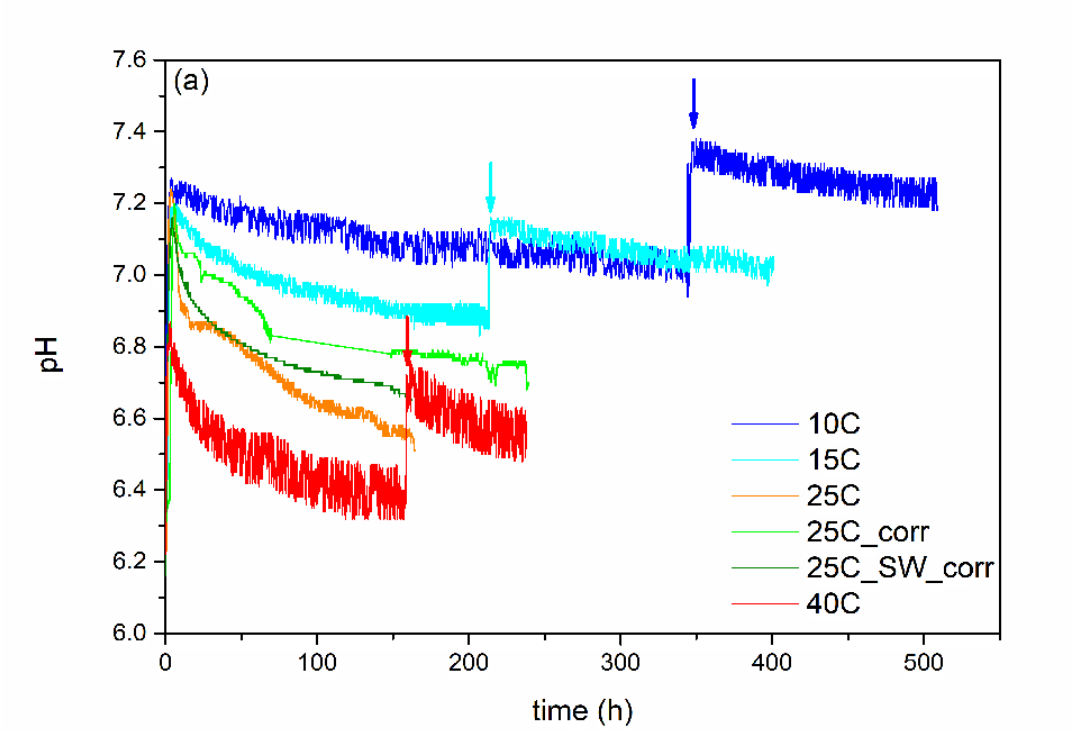
Table 7 - Calculated pH at siderite saturation as a function of temperature and CO_2 partial pressure in 0.1 wt.% NaCl and artificial seawater solution (SW).

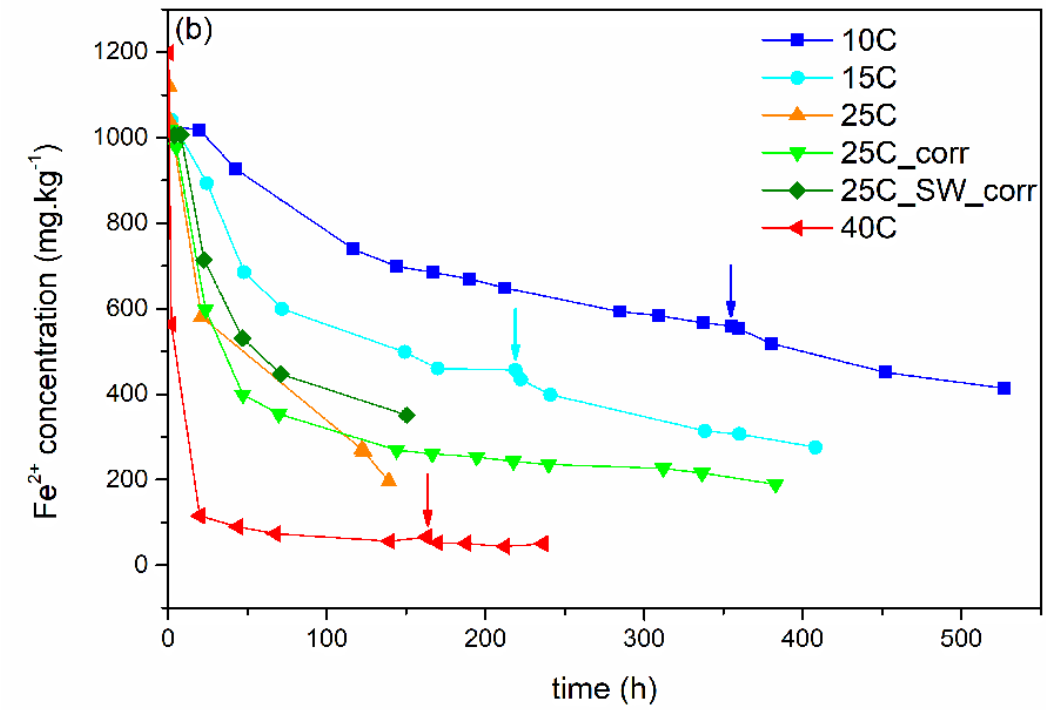
Temperature		**10 °C**	**15 °C**	**25 °C**	**25 °C_SW**	**40 °C**
pH at equilibrium	**10 kPa CO_2**	6.07	6.05	6.01	6.17	5.98
	5 kPa CO_2	6.27	6.25	6.21	6.37	6.18

Figure 13 shows OM and SEM images of the solids after the drying process in oxygen-free environment. Visually, the siderite presented different colors, ranging from greenish to brownish, which suggests that, although not detected by XRD, the precipitates were oxidized during the drying process. At low temperatures (10 and 15 °C) the precipitation of siderite was delayed, although the system was in metastable disordered state due to high $SR_{(siderite)}$. In such conditions the nucleation of solids occurred mostly in heterogeneous harnessing the surface free energy interfaces, such as the glass cell and probes (KHALEGHI *et al.*, 2020). In those cases, the formed solids were integrally glued to the available surfaces, forming well-adhered films. Samples were collected by scraping and showed vitreous luster, attributed to growth from the glass surface (Figure 13 (a,b)). SEM images show pieces of siderite presenting two types of texture. A smooth and homogeneous side that interfaced the cell walls and another that evidences the growth of siderite crystals which the surface was in contact with the solution.

At higher temperatures, 25 and 40 °C, the solids exhibited rounded morphology and higher precipitation kinetics. In the first hours of the test, the solutions became opaque, which, in principle, indicated homogeneous nucleation of siderite. The lower solubility limit of siderite under such conditions led to a rapid decantation of solids to the bottom of the cell, forming isolated crystals (JIANG & TOSCA, 2019, SUN *et al.*, 2009, JIANG & TOSCA, 2020).

At 25 °C the effect of ionic strength was also evaluated with the addition of corresponding salts to synthetic seawater (see item 3.2). In this case, smaller crystals were observed, which can be explained by the greater solubility of siderite in solutions that present higher ionic strength. There are also rhombohedral shaped precipitates, which, by analyzing the XRD results (Figure 11), can be also attributed to NaCl crystals formed from the drying process of the solution.


(a)
pH
time (h)
10C
15C
25C
25C_corr
25C_SW_corr
40C


(b)
Fe2+ concentration (mg.kg-1)
time (h)
10C
15C
25C
25C_corr
25C_SW_corr
40C

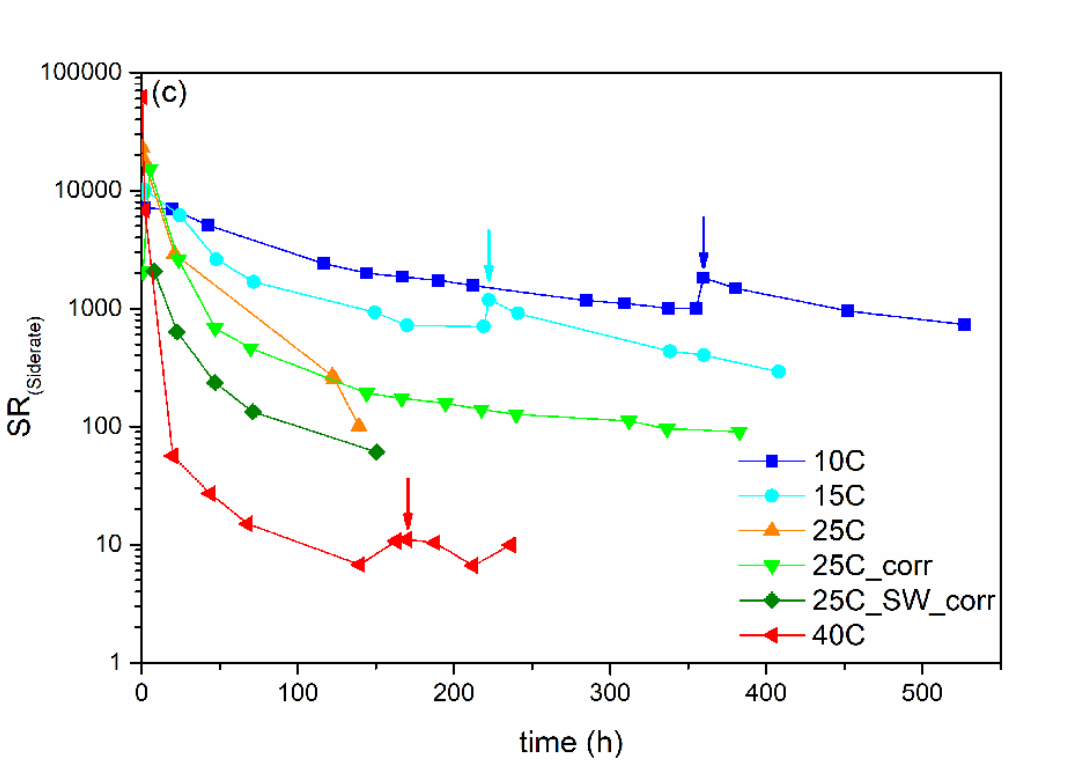


Figure 10 - Measured and calculated parameters in the de-supersaturation experiments (a) measured pH; (b) measured Fe^{2+} concentration; (c) calculated saturation ratio for siderite ($SR_{(siderite)}$). The arrows show when the CO_2 partial pressure was decreased from 10 to 5 kPa (SW = artificial seawater solution, corr = tests with corrosion coupons).

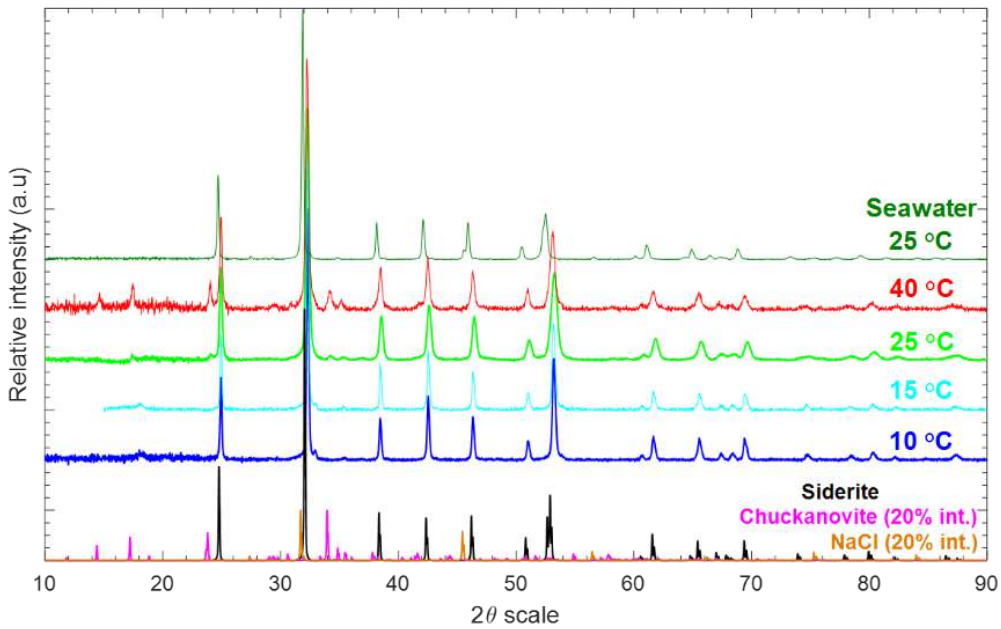


Figure 11 - XRD spectra of the bulk precipitate formed at different temperatures and reference spectra of siderite, chuckanovite and NaCl (halite).

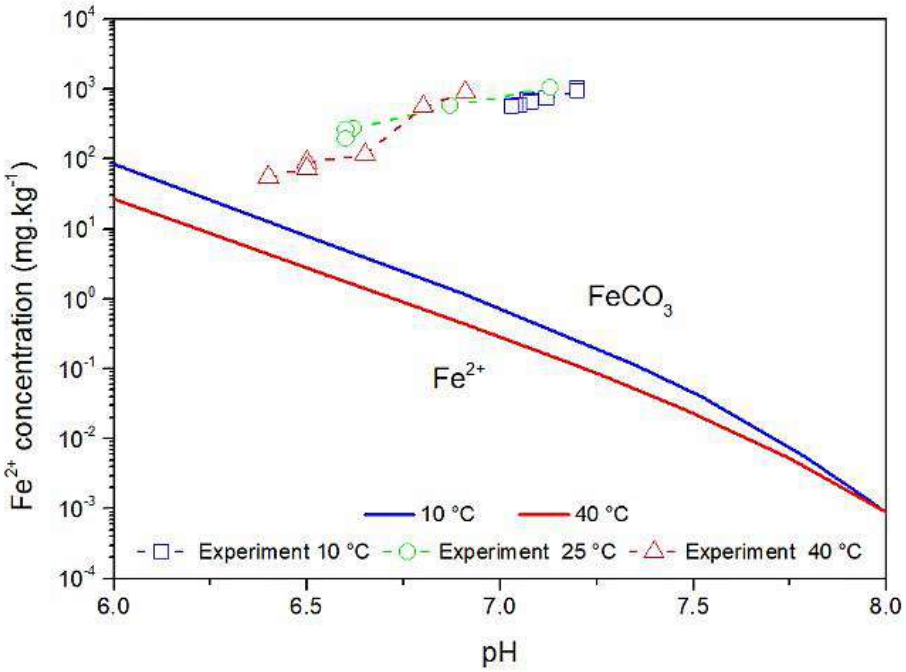
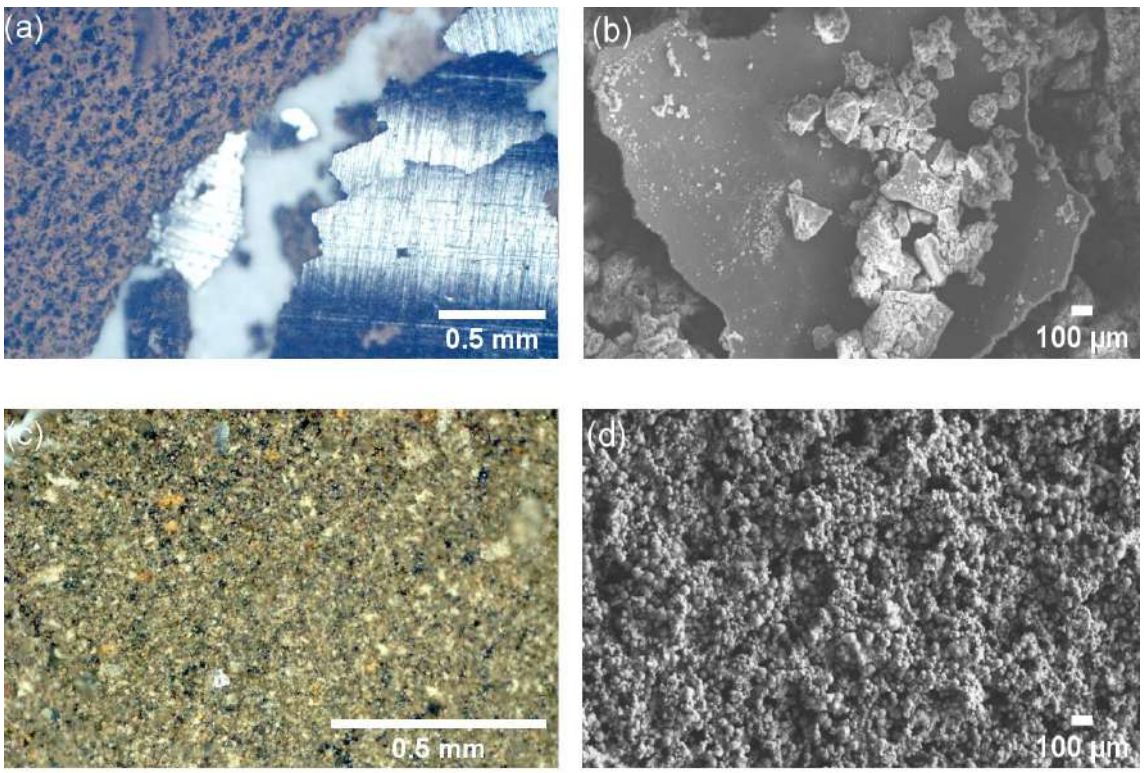


Figure 12 -Chemical stability diagram for Fe^{2+} and siderite ($FeCO_3$) at partial pressure of CO_2 equal to 9 kPa at 40 °C and 10 kPa at 10 °C (10% CO_2 in purging gas at 100 kPa total pressure). The solid lines give the Fe^{2+} solubility vs. pH at equilibrium at 40 °C (red) and 10 °C (blue). The dotted lines show the Fe^{2+} concentration vs. pH in the experiment with the start point at the high pH.



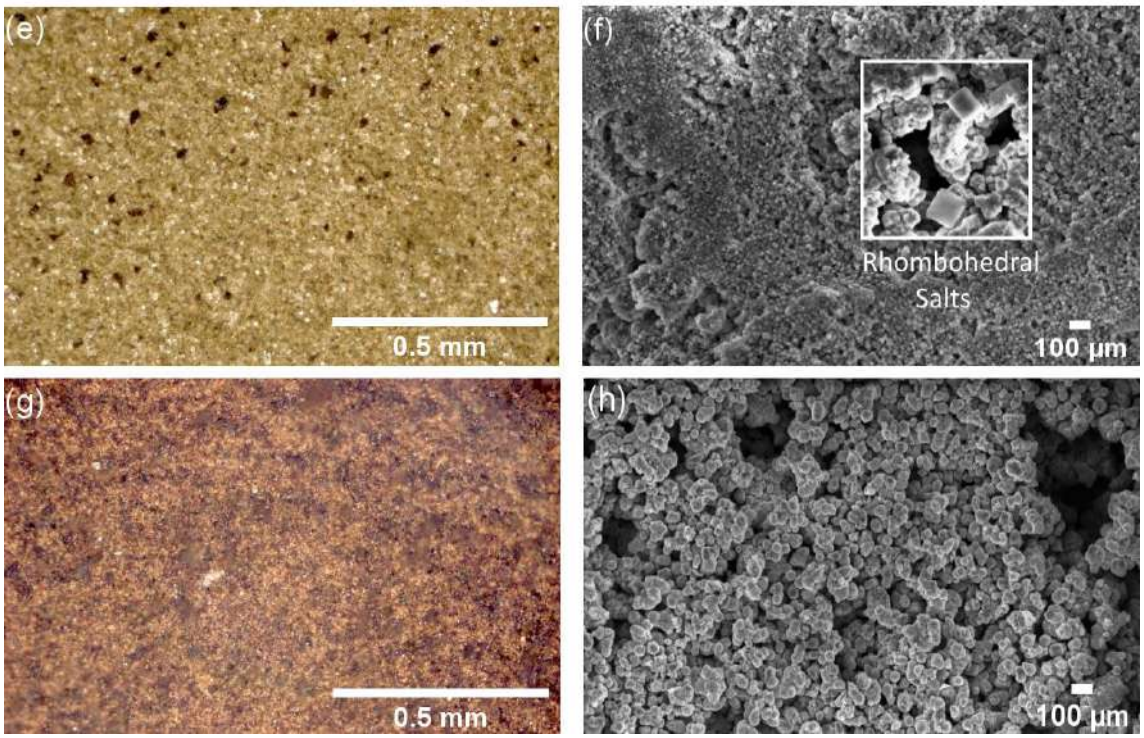


Figure 13 – OM and SEM images showing morphological differences among precipitates formed at 10 °C (a, b), 15 °C (c, d), 25 °C and seawater (e, f) and 40 °C (g, h).

4.2. Effect of as received layers and salt content on corrosion of armor wire steels

4.2.1. Corrosion in 0.1 wt.% NaCl solution

The corrosion rates of Type 1 and 2 steels at 25 °C and 10 kPa CO_2, with different surface finish ("machined" or "as received"), are shown in Figure 14. Initially, the corrosion rate was within 0.1 to 0.4 mm.y^{-1}. After a few hours it decreased to less than 0.01 mm.y^{-1} and remained low throughout the experiment. The discontinuities in the corrosion rate curves were due to the cathodic sweeps performed during the experiments, resulting in disturbances of the surface of the samples. This was also observed in the artificial seawater test, shown in Figure 18. The low corrosion rate was due to the formation of a protective $FeCO_3$ layer, see Equations 19, 21 and 23 (NEŠIĆ, 2007, KAHYARIAN *et al.*, 2016, LÓPEZ *et al.*, 2003a). The "machined" coupons exhibited a slightly higher corrosion rate than the "as received" materials. This may be related to the presence of oxides on the surface of the "as received" materials, as shown in Figure 5. Due to similarity of the corrosion rate obtained in the tests performed in 0.1 wt.% NaCl solution

for “machined” and “as received” samples, only the “as received” samples were used in the following electrochemical studies and surface characterizations of Type 1 and 2 samples, as well as in seawater experiments.

According to the potentiodynamic sweeps shown in Figure 15, the cathodic current density limit of “as received” samples decreased with time for both materials. It indicates that the cathodic reaction is under diffusion control due the depletion of bicarbonate ions and/or protons at the corroding surface. The porous layer of corrosion products on the steel surface limits the mass transport to the reaction sites (BERNTSEN *et al.*, 2013, AL-HASSAN *et al.*, 1998). When a fully protective layer is formed, it is observed that the OCP shifts to higher values (GADALA & ALFANTAZI, 2015, ROGOWSKA *et al.*, 2016). Steel Type 2 showed this behavior, while Type 1 exhibited a drop in OCP after 144 h (Figure 15 (a)) and a slight increase in the corrosion rate (Figure 14). This may suggest chemical and/or morphological changes in the carbonate layer and its protective properties.

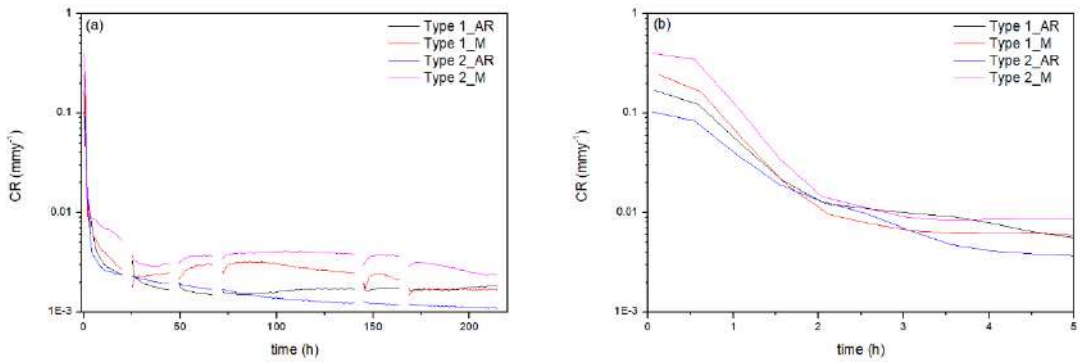


Figure 14 - Corrosion rate of steels Type 1 and Type 2 with “machined” (M) and “as received” (AR) surface finish in 0.1 wt.% NaCl solution (25C_corr in Table 3). The close-up on the right shows the corrosion rate of the materials in the first 5 h.

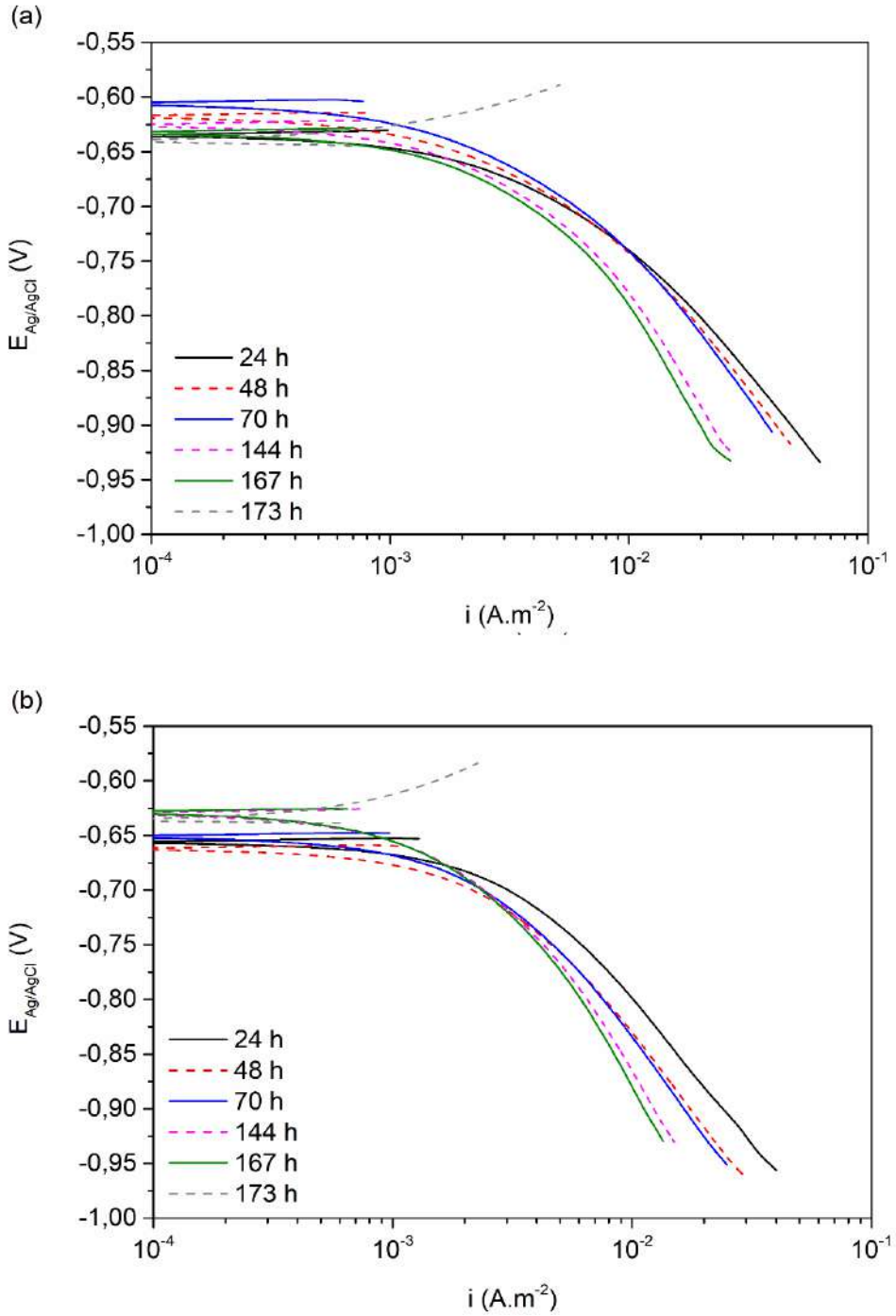


Figure 15 - Development of potentiodynamic sweeps over time for "as received" surface finish Type 1 (a) and Type 2 (b) in 0.1 wt.% NaCl solution (25C_corr in Table 3).

Figure 16 shows impedance Nyquist and Bode plots recorded throughout the tests. They confirm the development of a protective layer. At 2 h there was a single semicircle in the Nyquist plot, representing a charge transfer resistance, corresponding to a corrosion rate of about 0.02 $mm.y^{-1}$. Further on, the Nyquist plot exhibited two capacitive loops, which indicates the development of a more complex interfacial structure, e.g. an adherent layer

of corrosion products at the reaction sites. The development of the impedance of the layer was reflected in the corrosion rate, which reached 0.001 mm.y^{-1} for "as received" steel coupons. At 144 h, the Bode plot of the impedance of steel Type 1 had a third capacitive loop at 1-10 Hz. It coincides with the changes in OCP and a slightly increase in corrosion rate.

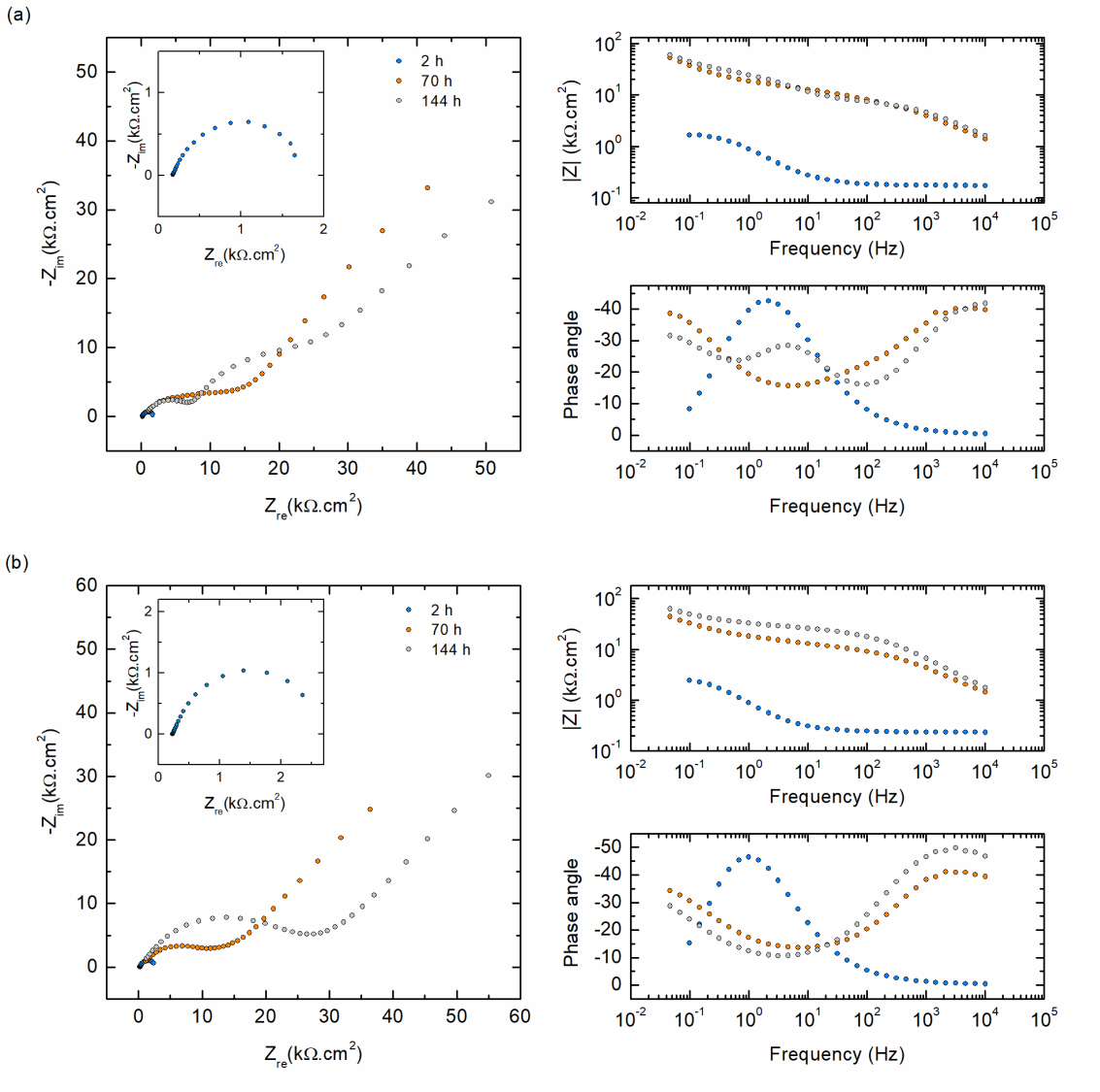


Figure 16 - EIS plots for "as received" steels (a) Type 1, and (b) Type 2 tested in 0.1 wt.% NaCl solution (25C_corr in Table 3).

The characteristics of the layers developed on the surface of the materials are shown in Figure 17. Both steel types were completely covered with spherical siderite with some platelets of chuckanovite on top. Chuckanovite was identified by XRD (Figure 11), and it has this characteristic plate morphology (SCHLEGEL *et al.*, 2010, BÉNÉZETH *et al.*, 2009). Higher magnification revealed that the siderite spherules consisted of subunits

with pyramids protruding the spheres. Others have observed the same morphology and suggest that the spherules are formed by aggregation of small siderite crystallites (INGHAM *et al.*, 2015, QU *et al.*, 2011, YU *et al.*, 2004). Chukanovite appears to adhere to the spherical siderite. Its formation can be related to the ratio of carbonate, hydroxide and Fe^{2+} ions in the solution (JIANG & TOSCA, 2019). Cross-section analysis revealed a layer thickness of about 5.4 μm and 4.9 μm in Type 1 and Type 2 samples, respectively. Pronounced voids in the layer of the Type 2 steel are highlighted in Figure 17 (c). However, no evidence of localized corrosion was found on stripped samples.

In summary, the results show that the high initial siderite saturation ratio led to fast growth of a carbonate layer at the steel surfaces. The layer had a high impedance which gave a low corrosion rate.

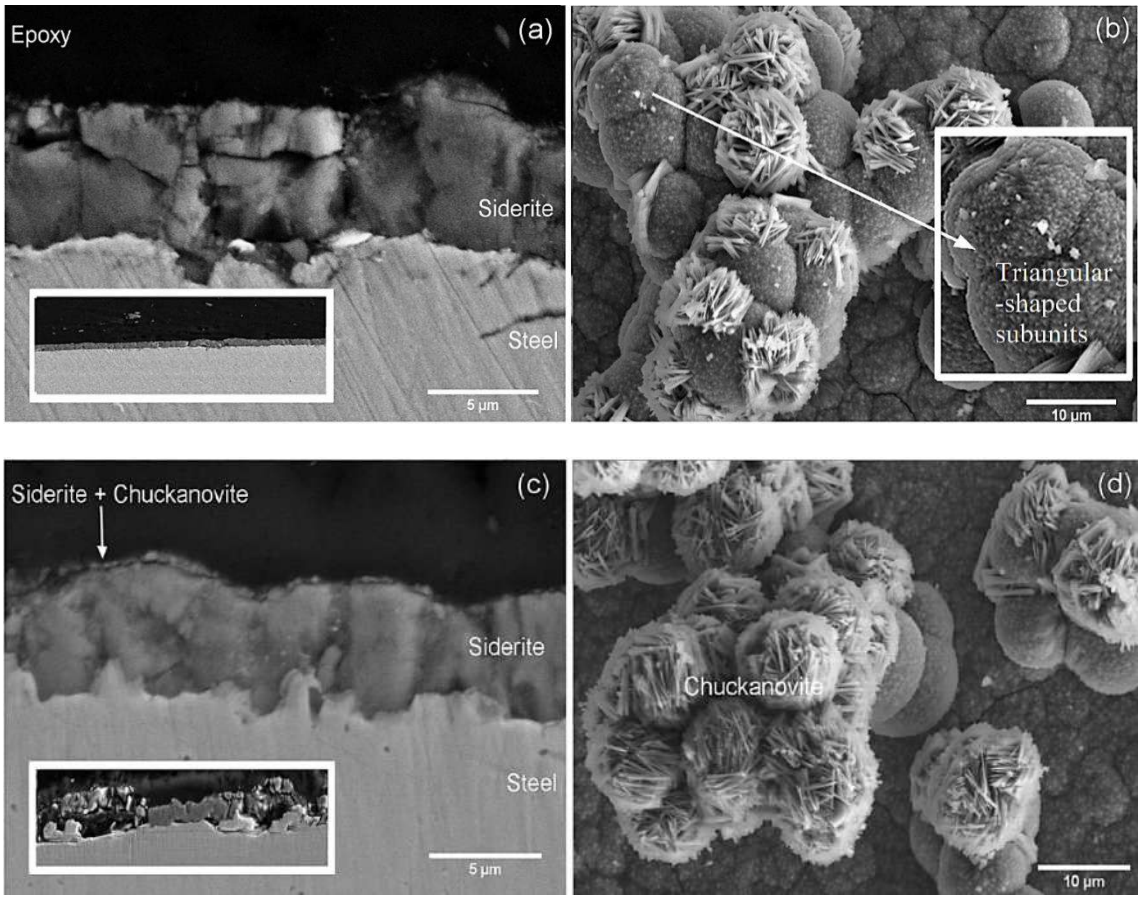


Figure 17 - SEM images of corrosion layers formed in 0.1 wt.% NaCl solution with high initial Fe^{2+} concentration and alkalinity (25C_corr in Table 3). (a) and (c) cross-sections of "as received" steels Type 1 and Type 2, respectively; (b) and (d) the surface of "as received" steels Type 1 and Type 2, respectively.

4.2.2. Corrosion in artificial seawater

Figure 18 shows the corrosion rate of the "as received" steel samples in artificial seawater supersaturated in siderite at 25 °C and 10 kPa CO_2. The evolution of the corrosion rate was similar to the one observed in low salinity solution. Initially the corrosion rate was 0.4 to 0.1 mm.y^{-1}, but it decreased to less than 0.01 mm.y^{-1} after a few hours of immersion. The corrosion rate remained stable and low throughout the experiment. It is an indication that corrosion products blocked the reaction sites.

The cathodic polarization sweeps (Figure 19) were similar to the ones recorded in 0.1 wt.% NaCl, indicating diffusion-controlled reactions of carbonic species at potentials below the OCP. However, the reduction in the derivative of polarization sweeps of steel Type 1 at about -0.3 V vs. OCP suggests that specific species may be reduced. The cathodic limiting current decreased over time, suggesting that the precipitated layer became more protective. The impedance spectra (Figure 20) confirm the formation of a protective layer at the surface and that it may have several sublayers with different impedance.

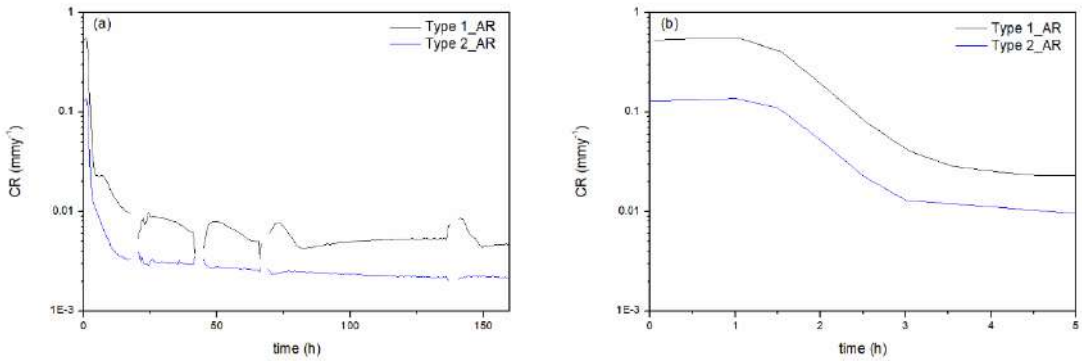


Figure 18 - Corrosion rate of "as received" steels Type 1 and Type 2 (25C_SW_corr in Table 3). The close-up on the right shows the corrosion rate of the materials in the first 5 h.

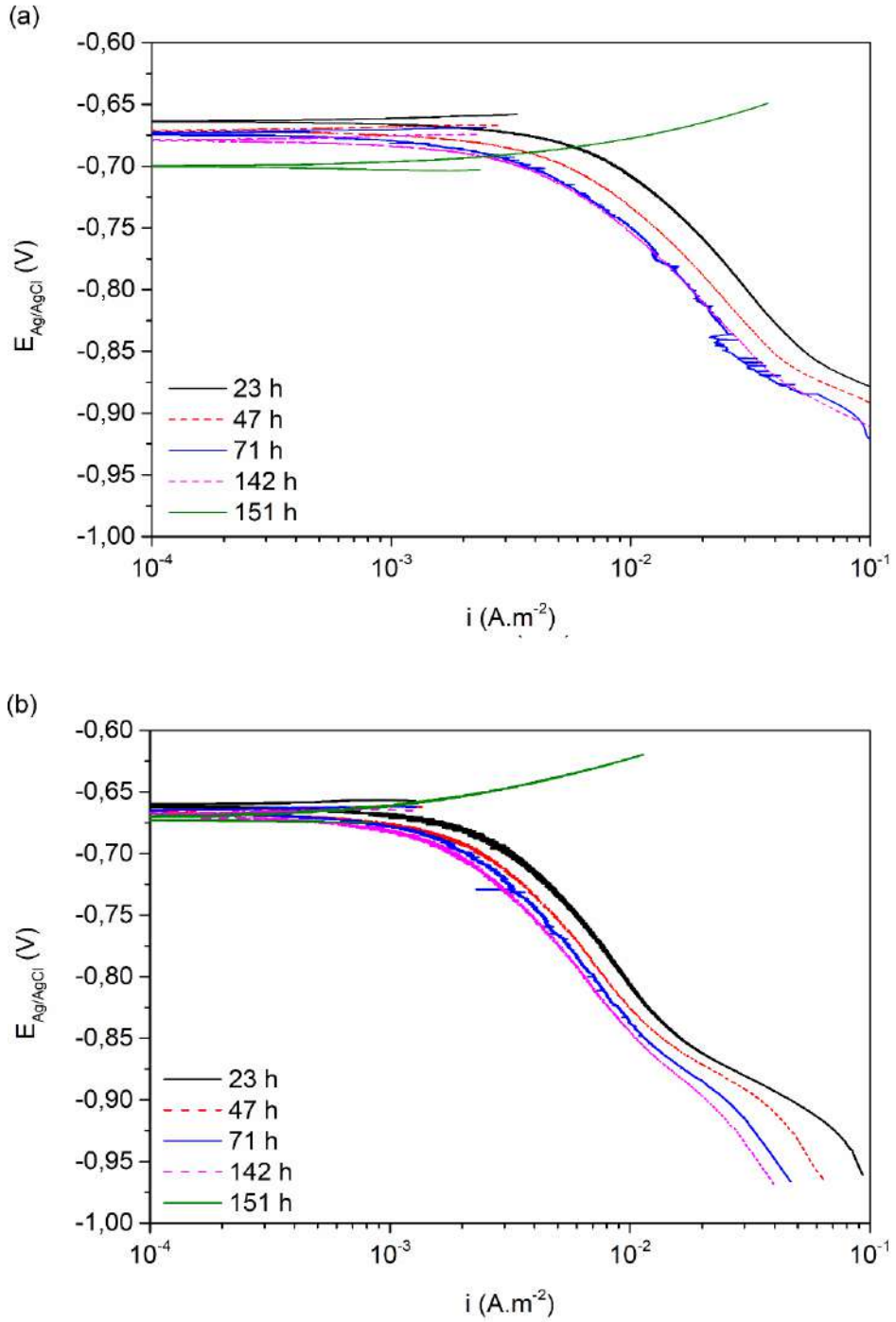


Figure 19 - Development of potentiodynamic sweeps over time for “as received” steels (a) Type 1 and (b) Type 2 in artificial seawater (25C_SW_corr in Table 3).

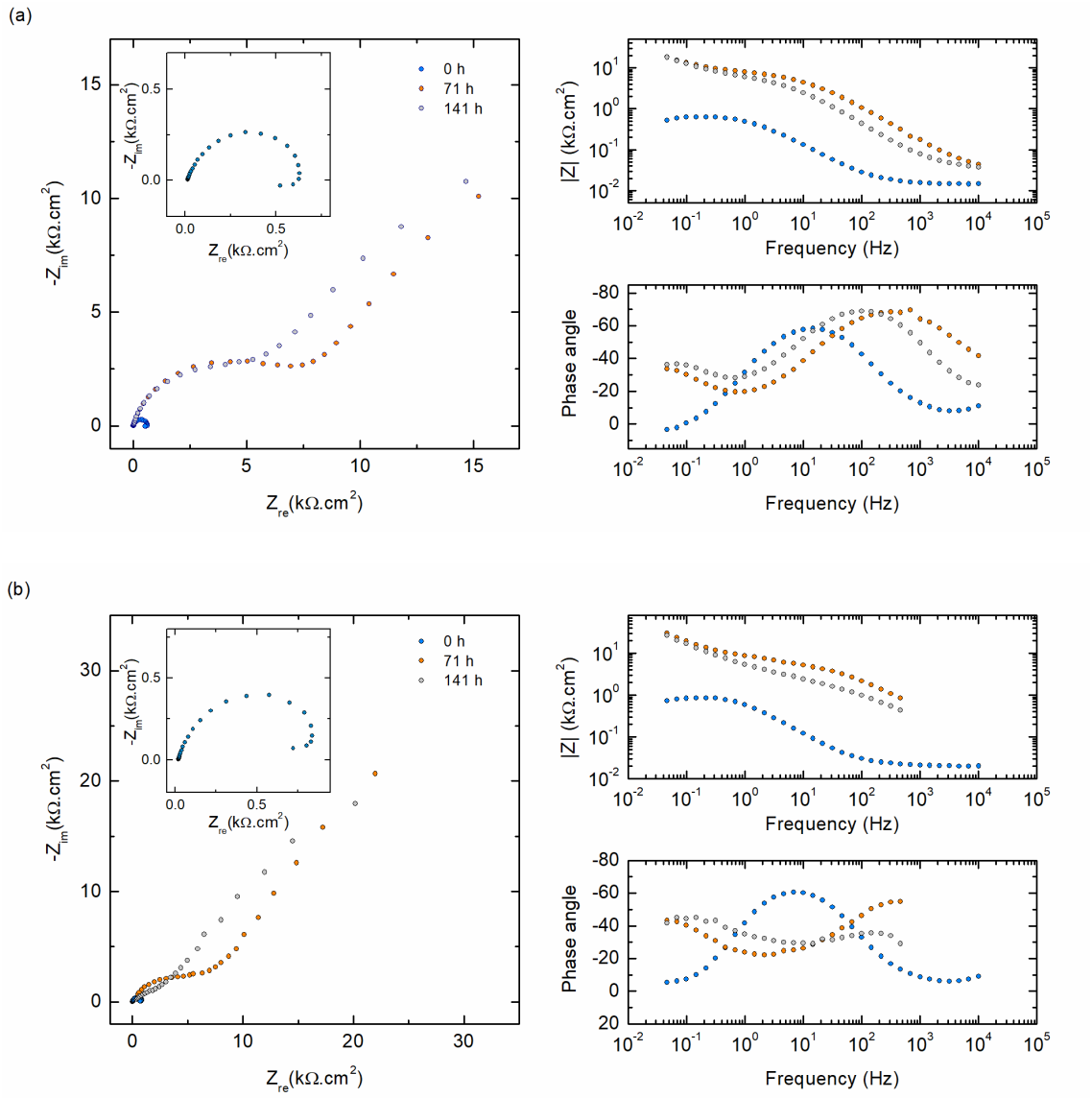


Figure 20 - EIS plots for "as received" steels (a) Type 1 and (b) Type 2 in artificial seawater (25C_SW_corr in Table 3).

The high ionic strength of the artificial seawater affects the activity coefficient of Fe^{2+}, hence, the $SR_{(siderite)}$ was lower despite a higher pH, alkalinity and Fe^{2+} concentration compared to the 0.1 wt.% NaCl water, as shown in Figure 10 (b) and (c). Thus, a slower growth rate of siderite may be expected compared to the low-salinity solutions. This may explain why the corrosion product layer was thinner; 1.8 µm and 1.6 µm on the samples Type 1 and Type 2, respectively, compared to the ca. 5 µm layer formed in the low salinity solution (Figure 21 (a) and (c)).

The cross-section images showed that Type 1 steel developed a uniform corrosion product layer, while two different phases can be observed on Type 2 steel. EDS analysis showed

that the inner layer on Type 2 steel contained traces of Mn and Zn, as established in the oxide on "as received" samples. The main part of the layer was siderite for both steel types.

Figure 21 (b) and (d) are top views of the corrosion product. The pyramidical crystals are typical for siderite. No chukanovite was detected, in accordance with the XRD (Figure 11). Others have also concluded that siderite is the final corrosion product on carbon steel in CO_2-brine systems at low temperatures rather than transient phases (TANUPABRUNGSUN *et al.*, 2012, XIA *et al.*, 1989). However, it should be noted that the $a_{CO_3^{2-}}/a_{Fe^{2+}}$ ratio at the end of the seawater test was 0.0030, while this ratio in the low salinity solution was 0.0018. This difference could be the reason why chukanovite was formed in the low-salinity solution, since it is considered the dominant phase in solutions with low $a_{CO_3^{2-}}/a_{Fe^{2+}}$ ratio (JIANG & TOSCA, 2019).

The corrosion products appear to be porous at the surface, but as shown in the cross-section images (Figure 21 (a) and (c)), the layer is dense at the metal interface. Although Type 2 steel had a slightly lower corrosion rate in both solutions, the preparation of the cross-section samples indicated that the precipitated layer was more brittle, and easily disbonded from the steel surface in some regions. This may be related to poor adhesion of corrosion products to the oxides present on the "as received" surface.

EDS spectra indicated that the siderite contained some calcium. It is possible that the precipitated carbonate was a mixed ($(Fe,Ca)CO_3$) phase. It is likely to occur since siderite and calcite are isostructural (YU *et al.*, 2004). As discussed above, the XRD spectra also indicated Ca^{2+} dissolution in the siderite that precipitated in the bulk solution.

The results show that siderite precipitation is so slow, that at 25 °C solutions can stay supersaturated and maintain a pH between 6.5-6.8 for 150-250 h, regardless of salinity of the solution (Figure 10 (a)). The "as received" oxidized surface and the development of the protective siderite layer leading to low corrosion rates and corresponding low corrosion current density should not promote SCC (PARKINS, 1979, LIU *et al.*, 2012). Under such conditions, the layer must be stressed to promote cracking and induce SCC. Based on the models, the recoverability of the siderite layer would act as one determining factor for SCC susceptibility. Another factor is defects in the layer where H^+ and/or HCO_3^- can migrate to the metal surface. The microstructural differences between the

steels Type 1 and 2, such as the texture and distribution of the phases, may also affect the diffusion and solubility of hydrogen into the active sites and, therefore, on cracking susceptibility (LIBERTO & GABETTA, 1998, BOGDANOV *et al.*, 2019).

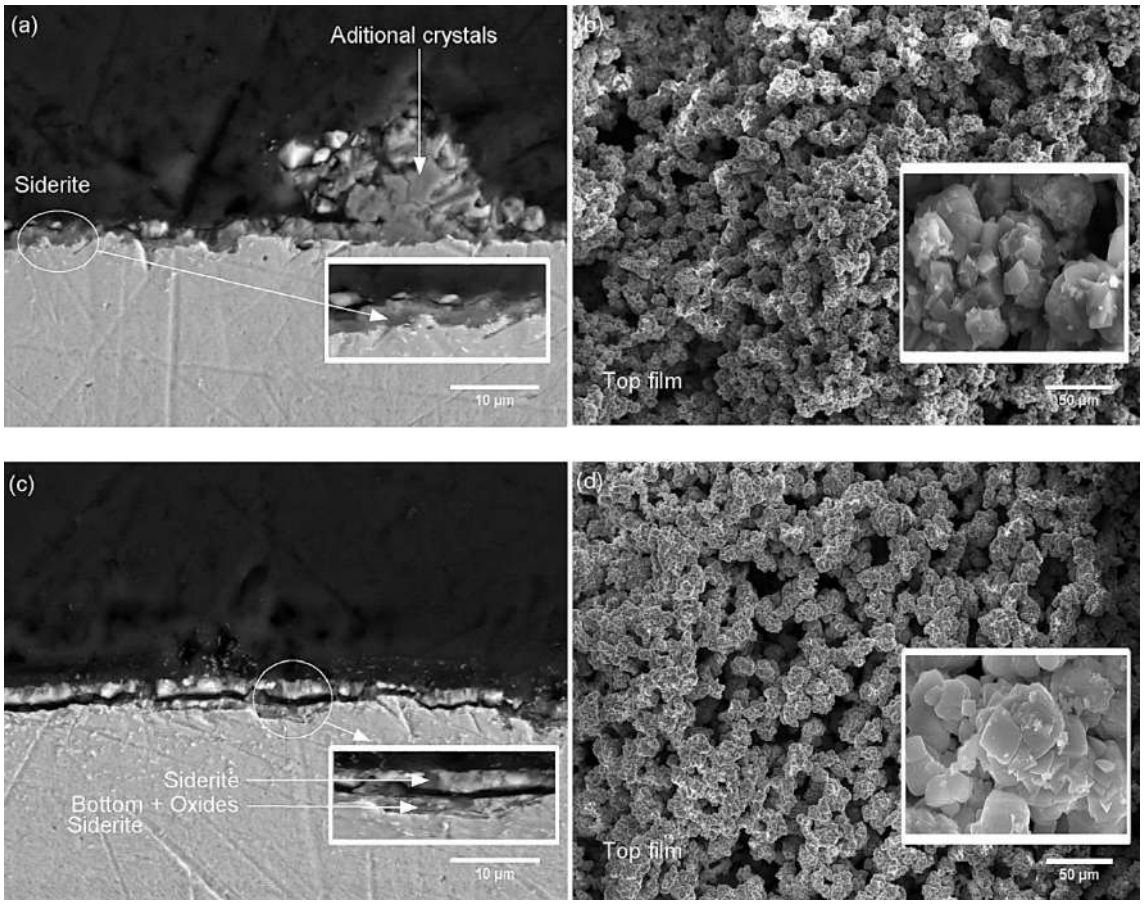


Figure 21 - SEM images of corrosion layers formed in artificial seawater solution (25C_SW_corr in Table 3). (a) and (c) cross-sections of "as received" steels Type 1 and Type 2, respectively; (b) and (d) surfaces of "as received" steels Type 1 and Type 2 steel, respectively.

4.3. Effect of exposed cementite on corrosion of armor wire steels

Under real annulus operating conditions, the enrichment of the solution with ferrous ions occurs from the direct contact of the material with CO_2 environment. This implies an initial solution acidification followed by a continuous increase of ferrous ions until it reaches a maximum value and precipitation starts. Although the ferrous ion production in annulus is high due to its particular spatial configuration (low V/S), the initial acidification promotes particular changes on steel surface that can impact on corrosion processes. Those changes are presented and discussed above using the steel Type 3, whose characteristics are listed in Table 1 and Figure 6 (c). Machined samples were

chosen for a good superficial and electrochemical characterization. Table 4 lists the environmental conditions used into this investigation.

4.3.1. Cementite exposure at acidic stage

All samples immersed in the tested solutions at acidic stage exhibited dark and opaque areas partially covering the surface in macroscopic scale after the first hours. Such color is related to the exposure of undissolved, porous and non-protective cementite. It appears after the preferential α-ferrite anodic dissolution at and around the pearlite in a deoxidized systems, as shown in Figure 22 (CORCORAN *et al.*, 2019, MORA-MENDOZA & TURGOOSE, 2002, AL-HASSAN *et al.*, 1998, OCHOA *et al.*, 2015, CROLET *et al.*, 1998, SUN *et al.*, 2012). Layers of cementite near ferrite are known to cause galvanic coupling between the phases, as mentioned in introduction of this work, which intensify the anodic dissolution of iron contained in the ferrite. Internal acidification caused by aqueous phase trapped into the pores of cementite is also considered a reason that contributes to the carbonic species reduction on the steel surface (CROLET *et al.*, 1998, NESIC *et al.*, 1996, CLOVER *et al.*, 2005).

While electrochemical processes occurred, corrosion products developed. The test cell presented V/S value 4 orders higher than the annulus. Therefore, the evolution of dissolved iron in the bulk solution was very low, achieving no more than 10 $mg.Kg^{-1}$ Fe^{2+} concentration, which prevents siderite formation (DUGSTAD, 2015). However, it was sufficient to increase the pH from 4.0 to 5.5, as a result of the production of alkalinity (HCO_3^-) and H^+ consumption caused by the direct reduction of carbonic acid (Equation 13) (HATAMI *et al.*, 2016, HONARVAR NAZARI *et al.*, 2010, NESIC *et al.*, 1996, KAHYARIAN *et al.*, 2018).

The effect of acidic conditions (pH 4.5-5.5) on the corrosion rate of the carbon wire steel is shown in Figure 24. In all tested conditions, the values were between 0.17 and 0.30 $mm.y^{-1}$ through the acidic stage, which lasted about 12 h. However, CR were calculated based on the B values found on the slopes of Tafel at the end of the precipitation stage, which tends to decrease their numbers. Thus, the CR calculated in the acid conditions, referring to the tests in Table 4, were recalculated in the tests of bare steels (Table 5) and are presented below. Despite showing some variation, all CR remained in the same order of magnitude and, therefore, can be considered valid. For the

discussion of the next topic, these values were important to evidence the effect of siderite precipitation on the reduction of CR in different scenarios.

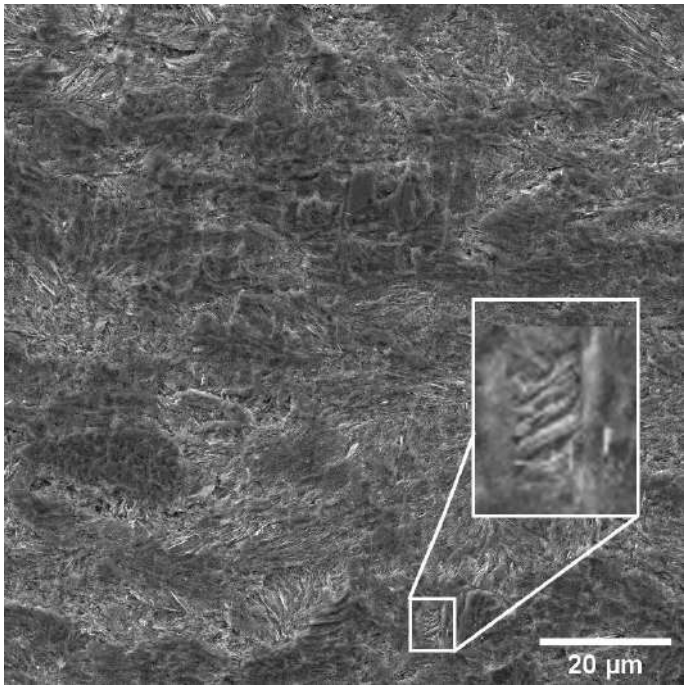


Figure 22 – SEM image of type 3 steel after acidic stage at 25 °C and 3.5 wt.% NaCl with a close-up on exposed cementite.

4.3.2. The effect of siderite precipitation on corrosion of armor wire steel

After the acidic stage, solids started to form on the steel surface as soon as the ferrous ion rich solution was transferred from the ferrous ion generator to the test cell, starting the precipitation stage. The increase in ferrous ion concentration was followed by an increment and stabilizing of pH between 6.75 and 7.25. According to the Pourbaix diagram Fe-H_2O-CO_2, calculated with 1000 g.Kg^{-1} Fe^{2+} concentration, at 25 °C and 40 °C and 10 kPa pCO_2 (Figure 23), at such pH range, salinity and OCP of the material, about -0.7 V in relation to reference electrode Ag/AgCl, the siderite is likely to form. In this pH range, the predominant cathodic reaction is the reduction of bicarbonate ions, although keeping in buffer region (HONARVAR NAZARI *et al.*, 2010, FIORAVANTE *et al.*, 2019). As expected, the diagram shows that decreasing salt content and increasing temperature shifts the region of siderite formation to lower pH.

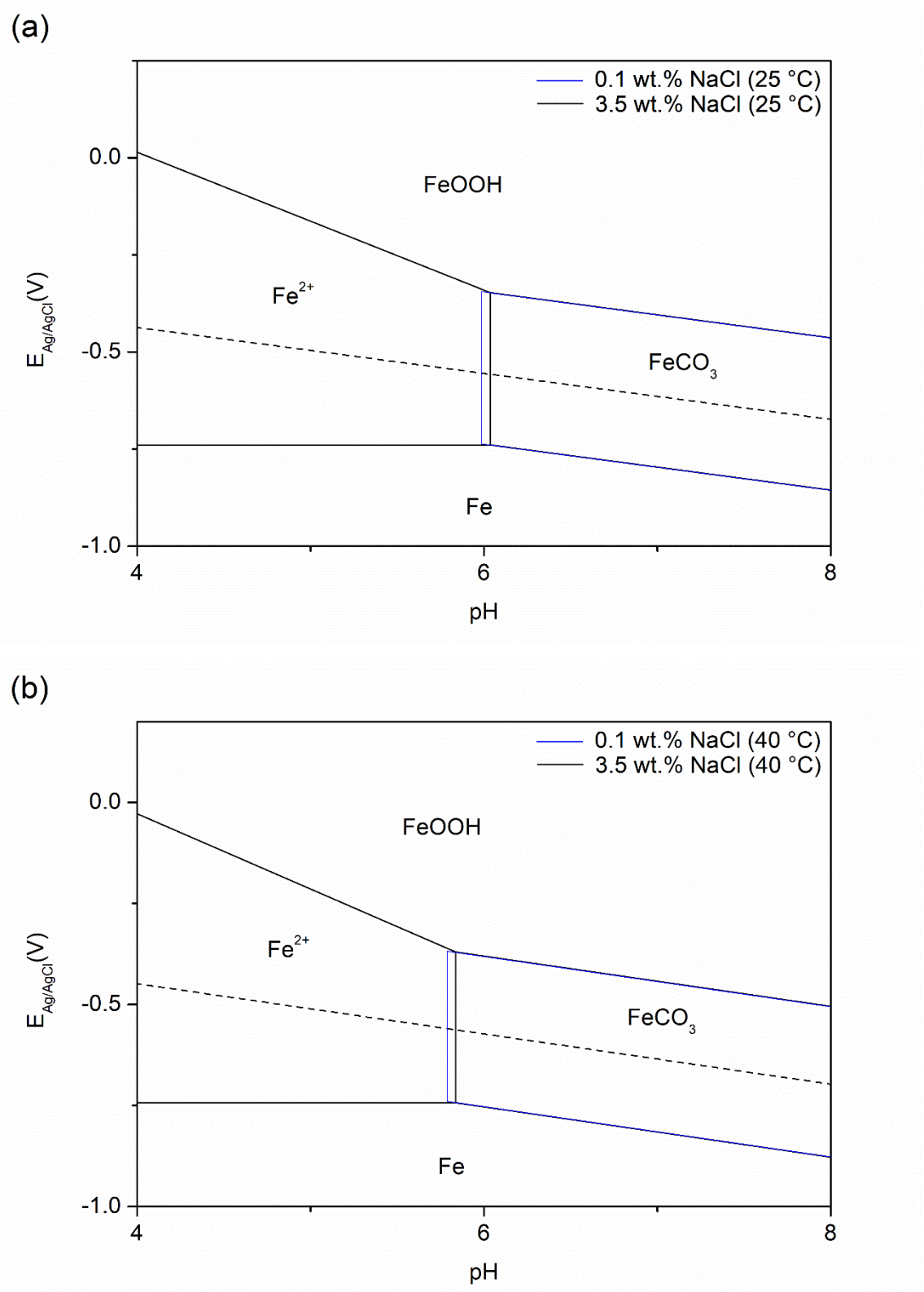


Figure 23 - Pourbaix diagram Fe-H_2O-CO_2 at (a) 25 °C; and (b) 40 °C and 10 kPa pCO_2, varying salinity.

The electrochemical influence of the exposed cementite was evaluated. For that, fresh samples were added from the precipitation stage for comparison. Contrary to literature

findings, as presented by (CROLET *et al.*, 1998, MORA-MENDOZA & TURGOOSE, 2002), the corrosion rates were higher in samples with pre-formed cementite on surface layer. In the case of an occluded and supersaturated environments of corrosion products, the presence of cementite may be considered a preferred area for cathodic reactions reducing HCO_3^- and acidifying the solution imprisoned within the layer. Furthermore, there is an important contribution of homogeneous nucleation in the formation of siderite on steel surfaces under supersaturation, which may suppress the relevance of cementite substrates. Thus, the well-known anchor effect of the carbides did not show to be determinant in annulus conditions.

After a couple hours immersed in Fe^{2+} rich solution, the corrosion rates of the samples dropped to values bellow the presented in acidic stage regardless of the temperature, salinity and initial surface conditions (Figure 24 (a)). The samples previously submitted to the acidic stage showed a reduction of an order of magnitude in the corrosion rate followed by a significant increase, but the condition at 25 °C, 3.5 wt.% NaCl that stayed above 0.12 $mm.y^{-1}$ throughout the test. The initial drop in CR values could be attributed to the adsorption of CO_2 bubbles onto the steel surfaces caused by transferring the solution (LOTZ & SYDBERGER, 1988). Bubbles adhering to metal surface insulates part of it from the electrical signal applied during electrochemical measurements, which leads to uncertainties in electrochemical responses, including changes in potential (FELIU *et al.*, 2017, SHI & ATRENS, 2011). Another possibility are the disturbances in the first siderite crystals causing loss of protectiveness, an effect attributed to Fe_3C due to an increase of cathodic reactions by having a lower overpotential for the hydrogen evolution reaction (MORA-MENDOZA & TURGOOSE, 2002, LOTZ & SYDBERGER, 1988, ZENG *et al.*, 2016).

The steel exposed to 25 °C and 0.1 wt.% NaCl with previously formed cementite layer on the surface, achieved a minimum CR about 0.012 $mm.y^{-1}$. After that, it reached the maximum value after 33 h immersed in the solution with high Fe^{2+} concentration, 0.075 $mm.y^{-1}$. With 91 h of test and pH 6.77, the CR was 0.071 $mm.y^{-1}$, which indicates a small downward trend. The sample added in precipitation stage reduced the CR from 0.23 to 0.01 $mm.y^{-1}$ in about 6 h, and maintained below this value throughout the test (Figure 24 (b)). At 25 °C and brine, the CR of the pre-corroded sample in acidic stage varied between 0.12 – 0.21 $mm.y^{-1}$ and showed an upward trend under pH about 7. While

the bare steel sample presented initial CR of 0.23 $mm.y^{-1}$ and finished around 0.07 $mm.y^{-1}$.

In 0.1 wt.% NaCl at 40 °C, the samples with and without exposed cementite on the surface presented basically the same trend in CR curve, achieving ca. 0.02 $mm.y^{-1}$ at the end of the tests (Figure 24 (a,b)). However, the sample that passed through the acidic stage presented a decay of CR at the beginning of precipitation stage, from 0.2 to 0.02 $mm.y^{-1}$, and had a rapidly increase to 0.1 $mm.y^{-1}$ after a few hours, when started to decline again.

At 40 °C and 3.5 wt.% NaCl, the pre-corroded sample kept high CR values during the test. After a small decay at the beginning, ca. 0.02 $mm.y^{-1}$, the CR exceeded the value of 0.1 $mm.y^{-1}$ after 15 h at near neutral pH conditions and maintained it until the end of the test (~100 h). In the same environmental conditions, but without exposed cementite on the surface, the steel reached 0.01 $mm.y^{-1}$ after 50 h of exposure. Without important cathodic areas, the siderite quickly covered the surface due to high temperature and reduced the CR. Elevated temperatures also reduce the solubilizing effect of halide ions which together reduce the activity of carbonic ions.

In summary, at 25 °C the surface condition was important only in solution with low NaCl content, where high CR values were found in presence of exposed cementite on the steel surface. With salt, both samples kept high CR values. Then, low temperatures must be a condition of concern, especially in brine. Comparing the results obtained at 40 °C, in siderite supersaturated systems CR cannot be directly attributed to the changes in chemical and the electrochemical reactions due to the increase in temperature and decreasing in viscosity (HATAMI *et al.*, 2016). In such cases, the effect of chloride ions on exposed areas of cementite must be considered, since it was the only one that presented high CR. As seen, CR of initial bare steel samples corroded the least and the samples pre corroded in acidic stage forming a cementite layer on the surface corroded the most. That reinforces the influence of cementite prevents adherent and protective siderite deposition in annulus conditions. Besides, iron dissolution from the armor wire steels is the expected condition in the field. Thus, only samples exposed to the acidic stage continued to be studied.

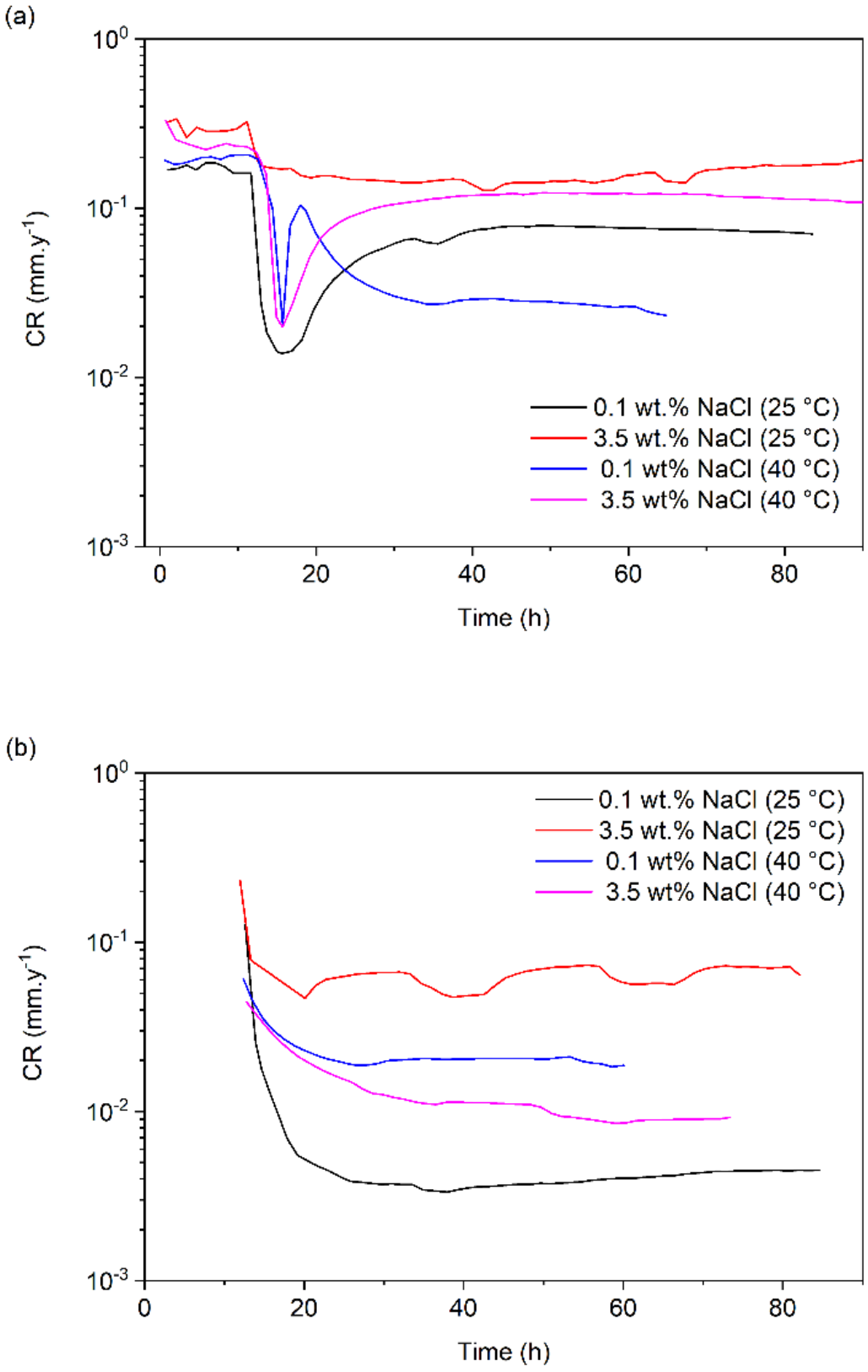


Figure 24 – Corrosion rate of the steel Type 3 analysing the effect of NaCl content and temperature of the system (a) with exposed cementite on steel surface; and (b) bare steel.

The $SR_{(Siderite)}$ and OCP reached the highest value as soon as the iron ion rich solution was transferred, then both decreased over time, although kept values above the ones obtained in acidic stage, as shown in Figure 25 and Figure 26, respectively. The decreasing in $SR_{(siderite)}$ during the precipitation stage suggests the occurrence of precipitation of siderite. The highest rates of reduction in the first hours of the tests were at 40 °C in 2-3 hours of near neutral pH exposure, indicating, again, that the precipitation is temperature dependent. At 25 °C and 0.1 wt.% NaCl, $SR_{(siderite)}$ showed a significant decrease throughout the test, while at the same temperature, but in brine, the $SR_{(siderite)}$ value remained practically the same, which increases the possibility of a precipitate with low protectiveness. This corroborates with the CR above 0.07 $mm.y^{-1}$ of both samples tested in this scenario (with and without cementite exposed on the surface). After 90 h, the $SR_{(siderite)}$ of all tested conditions were low and in the same order of magnitude. If there are no major disturbances in the systems, it should be considered that the precipitation rate would remain constant over longer time intervals, although equilibrium has not been reached ($SR_{(siderite)} > 1$).

The anodic shift in the potential right after the ferrous ion solution transference, suggests the limitation of active sites due to siderite precipitation and/or CO_2 bubbles attached on the surface, as mentioned before. Those increment on OCP were kept discrete for testing at 40 °C and 3.5 wt.% NaCl (< 10 mV). However, no change in OCP was maintained at 25 °C and 3.5 wt.% NaCl. Regardless of temperature, in 0.1 wt.% NaCl solutions the increase on OCP was more expressive, around 30 mV, followed by a significantly retarded corrosion rate (one order of magnitude less). This behavior is the opposite of expected when cathodic reactions decrease due to a diffusion limitation, which indicates a pseudo-protection of the mild steel surface characterized by a layer formation (LI *et al.*, 2014). However, the solids are not completely stable under such conditions, so the pseudo-protection may be transient. The OCP at 25 °C and brine returned to the same level as the previous stage at the end of the experiments, although the corrosion rate has decreased in relation to the acidic stage. In such case, the precipitates could retard the diffusion of the reductive species on the metal surface (PESSU *et al.*, 2016, GAO *et al.*, 2014, ALAM *et al.*, 2016).

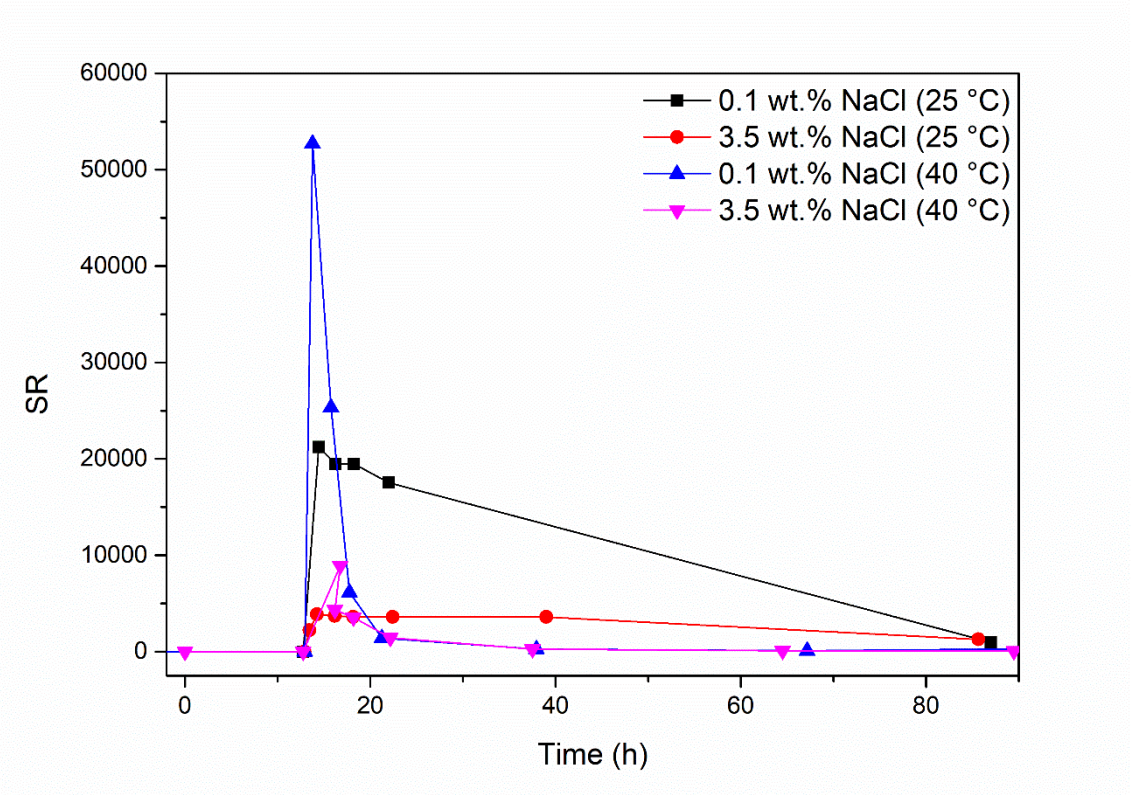


Figure 25 – $SR_{(siderite)}$ vs. time of the tests listed in Table 4.

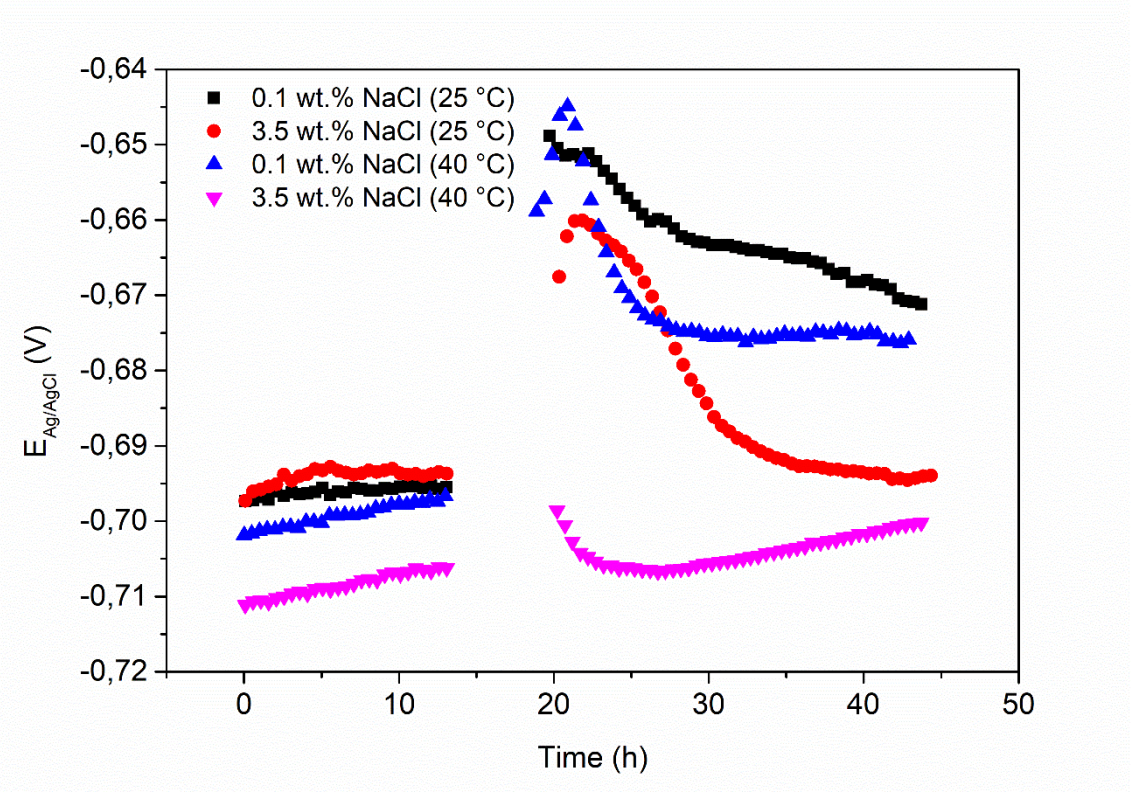


Figure 26 - Measured values of OCP over time of sample Type 3.

EIS tests were performed to assist in the study of electrochemical process of steel wires under different conditions of salinity, temperature and pH, determining both polarization and solution resistance. The impedance spectra measured at several immersion times are presented in Nyquist and Bode plots Figure 27 (a-d). Changes in pH from acidic to precipitation stage grew siderite and formed a layer coverage on the surface attributed to the increment of the slopes at lower frequencies in Nyquist plots, between 0.01 and 10 Hz. The Bode plots showed a sharp increase in resistance followed by a decay, except for the 25 °C brine condition, which agrees with the LPR measurements (Figure 24). That was attributed the reversible anodic iron dissolution and a film formed on the steel surface, which restricted the diffusion of ions through the surface film and/or CO_2 bubbles on the steel surface. For all conditions, the formation of an initial porous phase is assumed and it is attributed to the occurrence of massive precipitation from the bulk solution. In simulated equivalent electrical circuit (ECC) of Figure 28 (a) shows a second resistance (R_p) and capacitance (Q_p) related to the porous film formed on the steel surface, besides the non-ideal double layer capacitance (Q_{dl}) and the solution resistance (R_s).

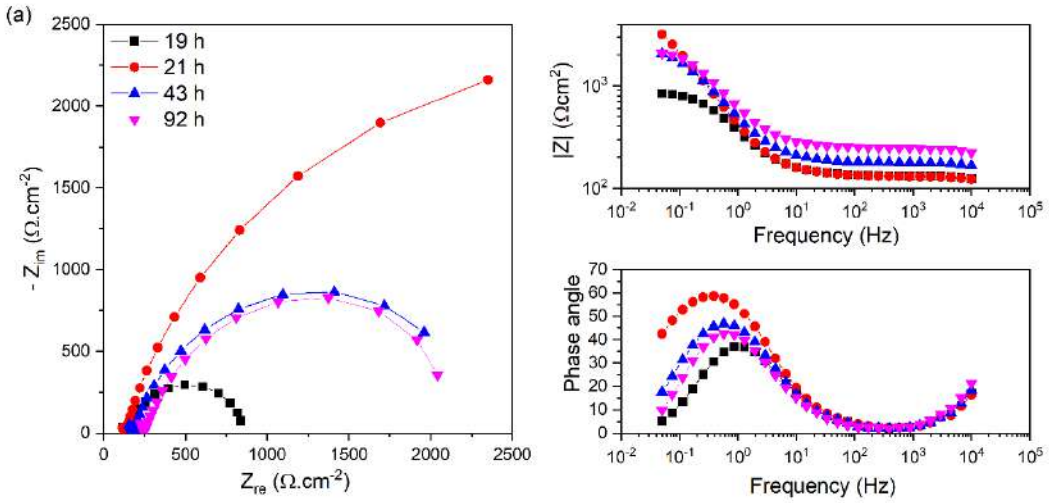
In both tested temperatures at 0.1 wt.% NaCl, the Nyquist plots showed not one, but two depressed semicircles with different amplitudes, as shown in Figure 27 (a,c). That suggests a formation of dissimilar corrosion products. So, the simulated ECC presented a third resistance (R_d) and capacitance (Q_d) at high frequencies (> 1000 Hz) (Figure 28 (b)). At 25 °C, the semicircles at high frequencies expanded very slightly throughout the test and no important changes in EIS resistivity were noted. The higher slope in Nyquist plot was measured at 21.3 h (after about 8 h of the pH increment - 21.3 h of test), which corresponds to the higher resistivity at frequencies from 10 to 0.1 Hz (3 kohm.cm^2), as shown in Bode plot (Figure 27 (a)). Up to this point, the charge resistance increased progressively, the pH was above 7, the Fe^{2+} concentration superior to 1000 mg.Kg^{-1} and $SR_{siderite}$ > 15000. At the same time, the respective OCP destabilized (Figure 26) and CR achieved the lower value, about (0.012 mm.y^{-1}) (Figure 24 (a)). At 43.2 and 92.1 h, the charge transfer resistance decayed to about 2 kohm.cm^2. It was assumed that the porous phase transformed and caused an unstable state on the electrode surface.

The resistance of the siderite achieved the highest value and presented a continuous increment at 40 °C and 0.1 wt.% NaCl, although pH 6.7 and SR below 100. That was also the only condition that the material exhibited low CR, up to 0.02 mm.y^{-1}, regardless of the presence of cementite (Figure 24). Thus, the two capacitive semi-circles in the Nyquist

plots at 40 °C is attributed a dense and very protective layer of siderite over the surface. The other scenarios presented dissolution of the formed solids during the tests.

In the brine conditions tested for both temperatures, 25 and 40 °C, the EIS Nyquist plots consisted of only one capacitive semi-circle, presenting no positive inflections in the impedance profile. The capacitive semicircles at lower frequencies are attributed to double layer capacitance and the charge transfer resistance. Those curves increased until around 2 and 4 hours after the step-change and then decreased, indicating such instability on the steel surface. Those were the conditions that maintained CR up to 0.1 $mm.y^{-1}$ and low $SR_{siderite}$ decay rate. Even at near neutral pH, the both situations presented localized corrosion, as will be discussed in the following topics. So, the equivalent circuit representing the steel surface at the end of the experiments in brine conditions are provided in Figure 28 (a).

In summary, those results confirmed that siderite formed under highly siderite supersaturated system even at low CO_2 and low temperature. This work also confirmed that the protectiveness of the film is a function of exposure time, temperature and solution salinity of the test.



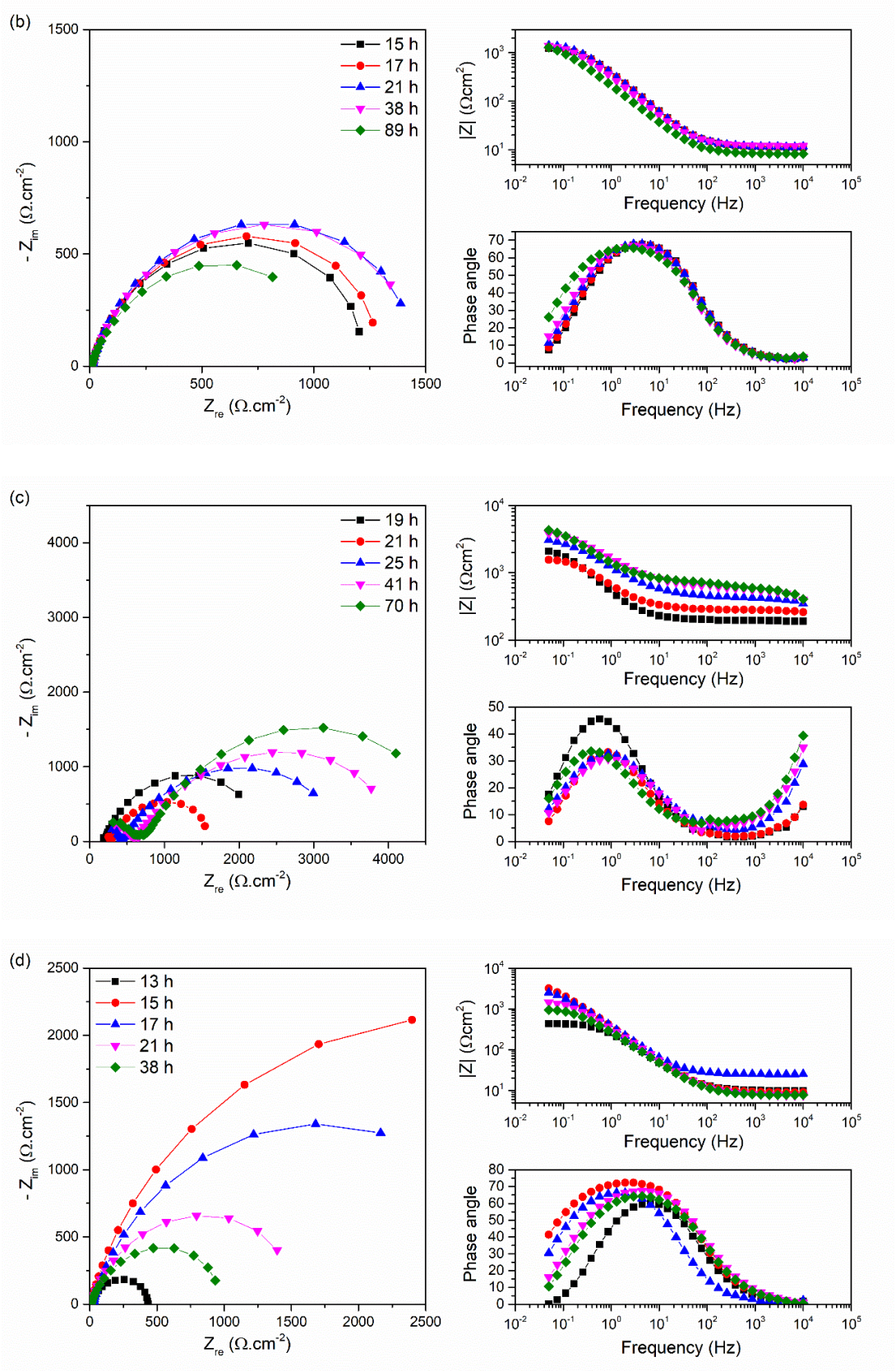


Figure 27 – EIS plots showing the effect of film formation over time on corrosion of the steel Type 3 in different salinity and temperature. (a) 0.1 wt.%NaCl 25 °C; (b) 3.5 wt.%NaCl 25 °C; (c) 0.1 wt.%NaCl 40 °C; and (d) 3.5 wt.%NaCl 40 °C.

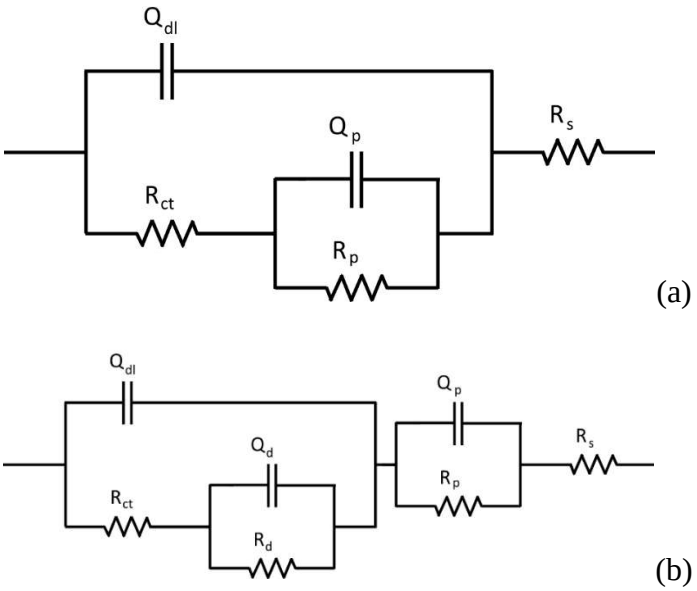


Figure 28 – ECC used for modelling the impedance spectra recorded for (a) 3.5 wt.% NaCl; and (b) 0.1 wt.% NaCl.

Figure 29 shows SEM images with the early stages of siderite precipitation on the steel surfaces with exposed cementite. According to the images, the morphology, size and distribution of siderite were affected by the solution salinity, temperature and immersion time. Those influences are in good agreement with the results obtained in the electrochemical and chemical evolution analysis. In short periods, 2-4 hours, the surface layer was non-uniform and some scratches due to the polishing process were observed. The precipitation kinetics of siderite was higher at 40 °C in solution with 0.1 wt.% NaCl. Larger portions of the surfaces were covered with compact crystals in the first 8 h of test. This occurred due to the decrease of siderite solubility at higher temperatures (HONARVAR NAZARI *et al.*, 2010). At 25 °C and 0.1 wt.% NaCl, the surface of the samples was completely covered with round siderite crystals after 24 h. However, in brine conditions for both tested temperatures, the precipitation rate was low and the crystals tended to gather in clusters.

For all studied cases, the siderite exhibited spherical shape, as reported by CAMPOS *et al.* (2021). An image processing software was used to measure the area covered by siderite in each image. Those results are displayed in Figure 30. In general, all samples showed a large initial growth rate of the siderite, reaching more than 70% of the area covered in the siderite after 24 h of exposure. At 40 °C and 0.1 wt.% NaCl the siderite covered 90% of the steel surface in the first 4 h. The sample exposed to 25 °C and

3.5 wt.% NaCl was the latest to form siderite on the surface, achieving about 23% in the first 8 h, while the others already reached a mark above 70% of coverage.

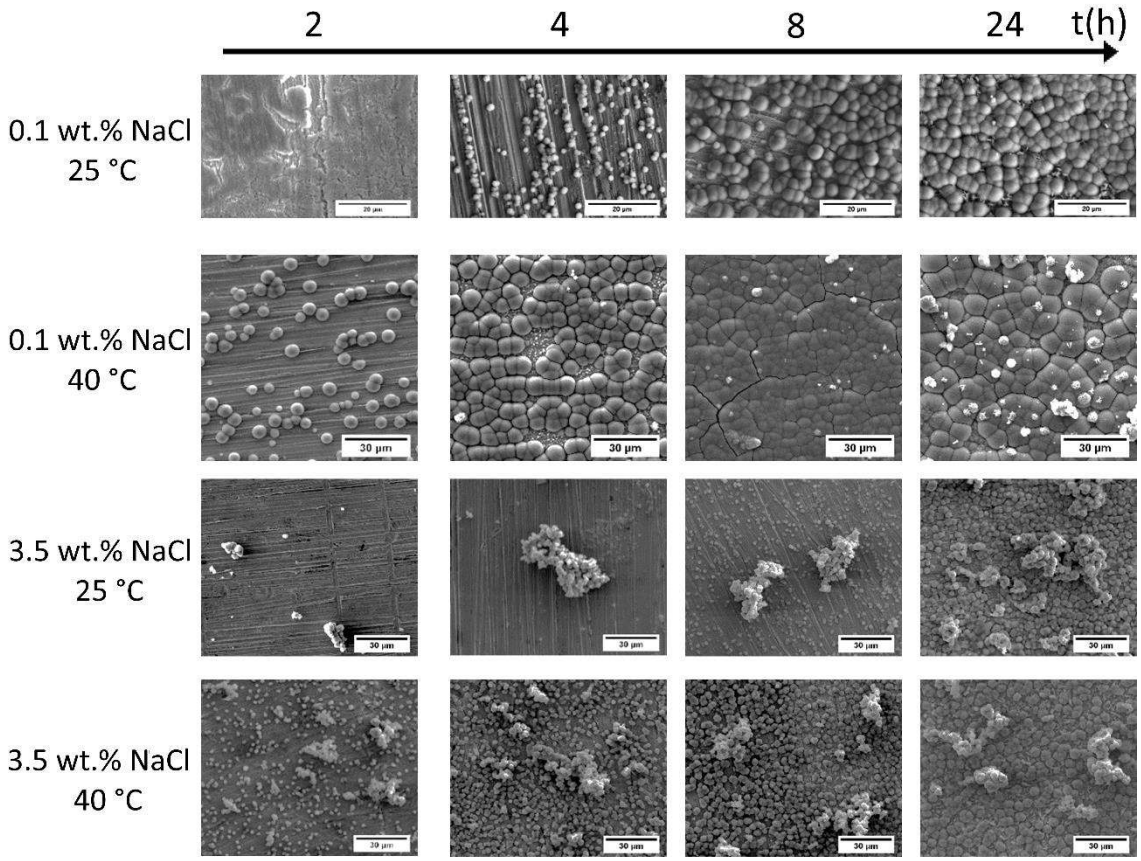


Figure 29 – The effect of salinity and temperature on the precipitation and growth of siderite crystals over time in steel Type 3.

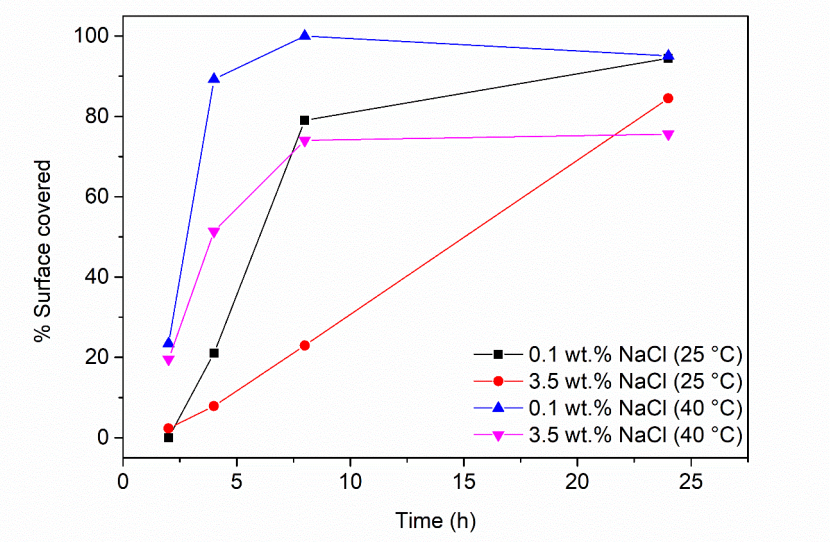


Figure 30 – Area covered by the siderite layer over time in steel Type 3 under different salinity and temperature (in %).

At 25 and 40 °C and 0.1 wt.% NaCl, the cross-section samples showed general corrosion, as shown in Figure 31 and Figure 32, respectively. EDS analysis revealed that the ratio of atomic of Fe, C and O is far from 1:1:3 as expected for siderite (Table 8 and Table 9). Those results suggests that the films were oxidized. Some studies using XRD revealed that Fe_2O_3 may be formed from hydroxyl groups (e.g. α-FeOOH) as a result of adsorption of water or oxygen on siderite (HEUER & STUBBINS, 1999, ZHOU *et al.*, 2017). This was attributed to the lack of time and temperature for Otswald ripening[5] to stabilize siderite, not only during the tests but also in the drying and storage processes. The condition at 25 °C and 0.1 wt.% NaCl presented two kinds of precipitates: light siderite crystals encrusted in a dark layer of precipitates. The total thickness of the layer was about 4.7 µm. At 40 °C and the same salinity condition, the cross-section images revealed a layer thickness of 10.3 µm. Two distinctive colors of precipitates are also seen, an outer and darker that presented elevated O atom%, and an inner and lighter. In the steel surface there are areas presenting cementite that was probably formed during the acidic stage. Those double layers of precipitates are in good agreement with the results found by EIS under 0.1 wt.% NaCl conditions. The stripped samples are present in Figure 36 (a, b) related to the tests performed at 25 and 40 °C, respectively. At 25 °C there are small and shallow spots that were not visible in the cross-sectional analysis of the sample. At 40 °C the spots were larger, though also shallow, with depth ca. 5 µm.

In brine conditions occurred localized corrosion, as shown in Figure 33 and Figure 34 for the tests at 25 and 40 °C, respectively. This is in agreement with the low $SR_{(siderite)}$ and a display of thin and heterogeneous corrosion products compared to samples tested with low wt.% NaCl content. Heterogeneous corrosion products may promote areas that are more reactive than surround surface. The layer thickness of the sample tested at 25 °C was 1.6 µm. At 40 °C this value was 3.5 µm.

EDS analysis presented Cl element in brine conditions, besides Fe, C and O related to siderite (Figure 33 (b) and Figure 34 (b)). That may be a result of the final dry process on the top of the precipitates, forming NaCl, and/or due formation of soluble Fe^{2+} chloro-complexes species produced during steel corrosion in the localized corrosion tips. The possibility of Fe^{2+} chloro-complexes formation raised once Na was not detected in EDS

[5] Ostwald ripening is a balance equation that describes the rate of change of the particle density.(VAN WESTEN & GROOT, 2018)

maps. The presence of chlorine element in localized corrosion confirms its influence on the development of the localized attack, suggesting that in brine conditions, specially at lower temperatures, the siderite precipitation is very slow and partially protective, even at near neutral pH and supersaturated with corrosion products. This can be attributed to the reduced Fe^{2+} activity in the presence of Cl^-, which hinders the locally formations of siderite layer on the steel surface. The potential of siderite is higher than the bare steel, which immersed in an corrosive electrolyte, localized corrosions may occur and propagate (HAN *et al.*, 2010, GAO *et al.*, 2014).

Figure 35 shows Pourbaix-type diagram Fe- Cl^--H_2O calculated for conditions at 25 and 40 °C considering Fe^{2+} 0.02 M (around 1100 $mg.Kg^{-1}$) in pH between 4 and 8. The increase in temperature from 25 to 40 °C decreased the Fe^{2+} chloro-complexes areas, limiting its formation to pH ca. 0.3 units down. According to the graph, $FeCl^+$ is thermodynamically favored in potentials above 0.7 V, in agreement with OCP measurements (Figure 26), and if the Cl^- concentration is higher than 1.6 M. That molality corresponds to about the triple of Cl^- concentration in bulk of the solutions with 3.5 wt.% NaCl. That is, an accumulation of chloride ions with time in the localized corrosion must be considered, which increases the overall corrosion rate (SUZUKI *et al.*, 1973, MANKOWSKI & SZKLARSKA-SMIALOWSKA, 1975, GIL *et al.*, 2018). The accumulation of chloride ions can occur as a result of electrochemical mechanism reactions related to localized attack and caused by a pronounced oxidation process. This leads to an excess of positive ions and induces chloride ions to migrate towards them to maintain electrical neutrality. Equation 38 proposes the reaction to form $FeCl^+$ in the pit. After formed, $FeCl^+$ can react with water and then produce hydrogen ion (H^+), which lowers the pH in the localized corrosion, as shown in Equation 39 (SALLEH, 2012).

$$Fe^{2+} + Cl^- \rightarrow FeCl^+ \qquad \text{Eq. 38}$$

$$FeCl^+ + H_2O \rightarrow FeOH^+ + H^+ + Cl^- \qquad \text{Eq. 39}$$

Evidences of localized corrosion morphology were also found on stripped samples analyzed by SEM (Figure 36 (c) and (d)) and confocal microscopy (Figure 37 (a) and (b)), whose voids showed ca. 20 µm of depth. The samples tested at 40 °C and 3.5 wt.% NaCl seemed to be less affected by the corrosive environment than at 25 °C not only because the lower CR, but also for maintaining the surface roughness of the sanding

process. This is related to the influence of temperature on the siderite formation and CO_2 solubility.

As seen in all cross-section images, precipitates had cracks. That were possibly caused during preparation of the samples (embedding and sanding) or/and due to the oxidation of the film, indicated by EDS results. Therefore, it is not possible to say whether the adhesion of prior siderite could provide good protection to the steel.

According to the results, the brine conditions were the most severe if compared to the low salinity ones. Changes in the ionic strength of the solution led to destabilization of the siderite, such as lower temperatures and higher Cl^-, resulting in the formation of localized corrosion. Cl^- is known to affect the process of localized corrosion of carbon steels in CO_2 environments being considered the key to initiate localized corrosion (GAO *et al.*, 2014, LIU *et al.*, 2014). This shows that the effect of Cl^- on destabilize the siderite is preponderant on the effect of decreasing CO_2 solubility by the increment of Cl^- concentration in siderite supersaturated solutions. However, regardless of test temperature and salinity, the corrosion products showed some protection, once the corrosion rates decreased as soon as the pH increased, being even more effective in the condition at 40 °C.

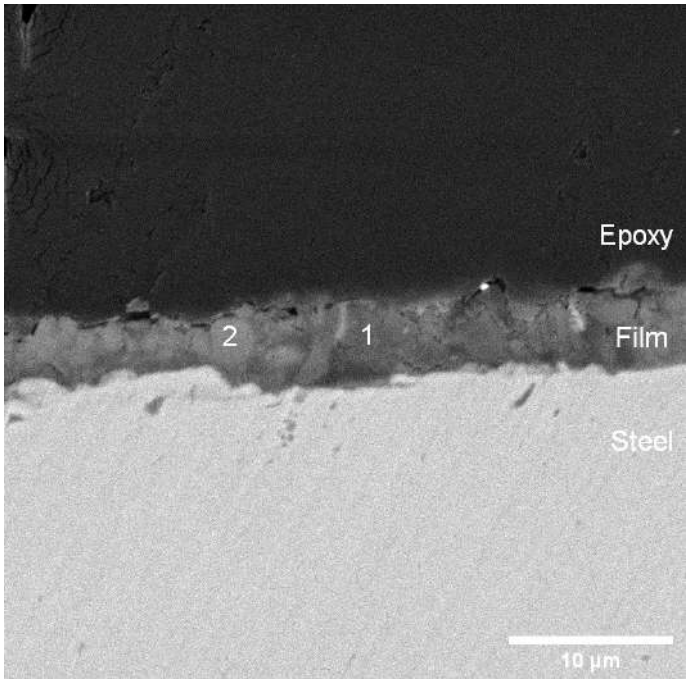


Figure 31 – SEM image of cross-sectioned sample Type 3 tested at 25 °C and 0.1 wt.% NaCl showing light siderite crystals (n. 2) encrusted in a dark layer of precipitates (n. 1).

Table 8 – EDS analysis in the areas indicated in Figure 31.

EDS atom %	Fe	O	C	Si	Al
1	36.56	33.99	27.68	1.77	-
2	12.85	50.43	35.42	-	1.31

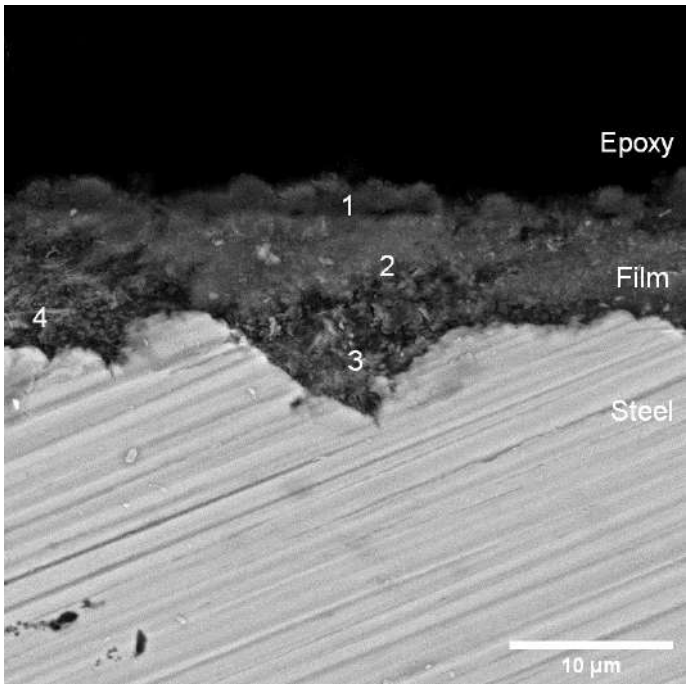


Figure 32 – SEM image of cross-sectioned sample Type 3 tested at 40 °C and 0.1 wt.% NaCl showing an outer and darker layer (n. 1); an inner and lighter (n. 2); and areas presenting cementite (n. 3 and 4).

Table 9 - EDS analysis in the areas indicated in Figure 32.

EDS atom %	Fe	O	C	Mn
1	23.33	41.41	35.05	-
2	33.01	30.29	36.70	-
3	63.1	-	36.18	0.72
4	78.24	-	21.46	-

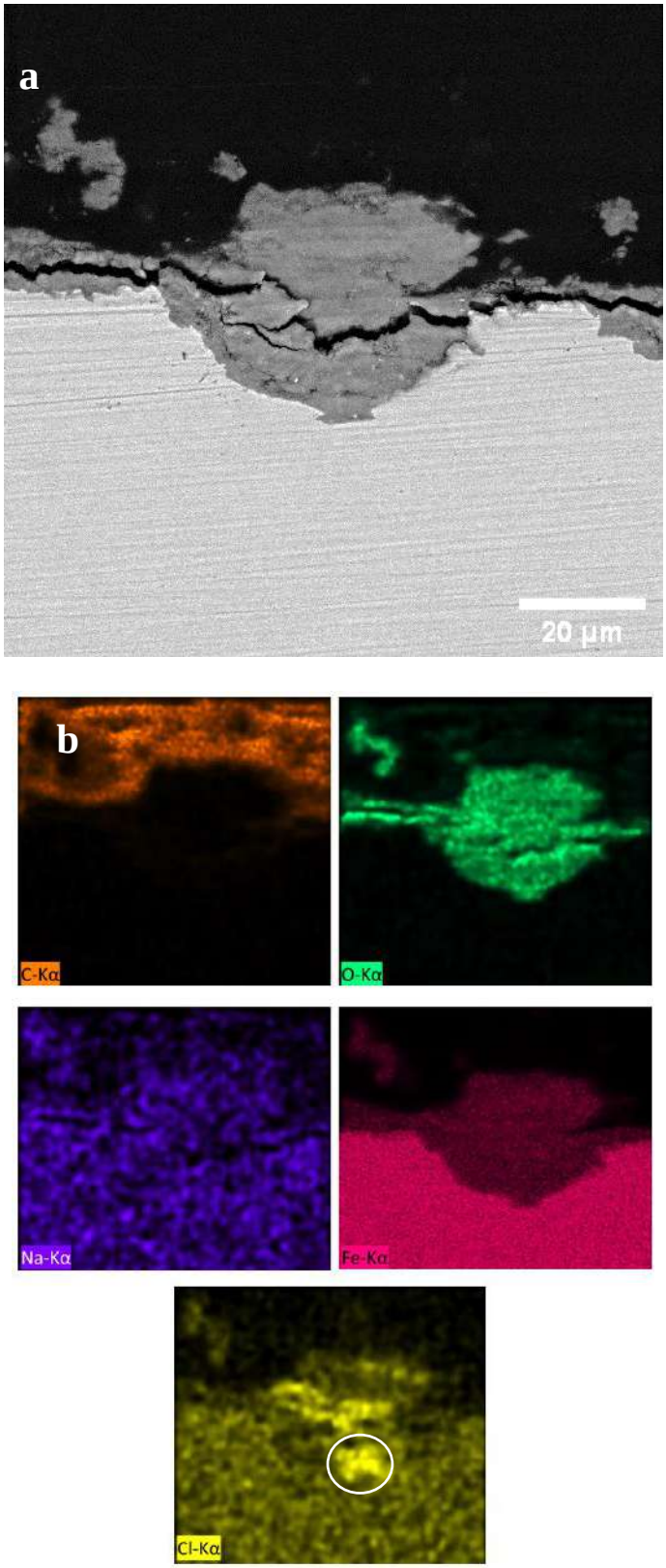


Figure 33 – (a) SEM image of cross-sectioned sample Type 3 tested at 25 °C and 3.5 wt.% NaCl showing localized corrosion. (b) SEM maps highlighting siderite formation and presence of element Cl in localized corrosion tip.

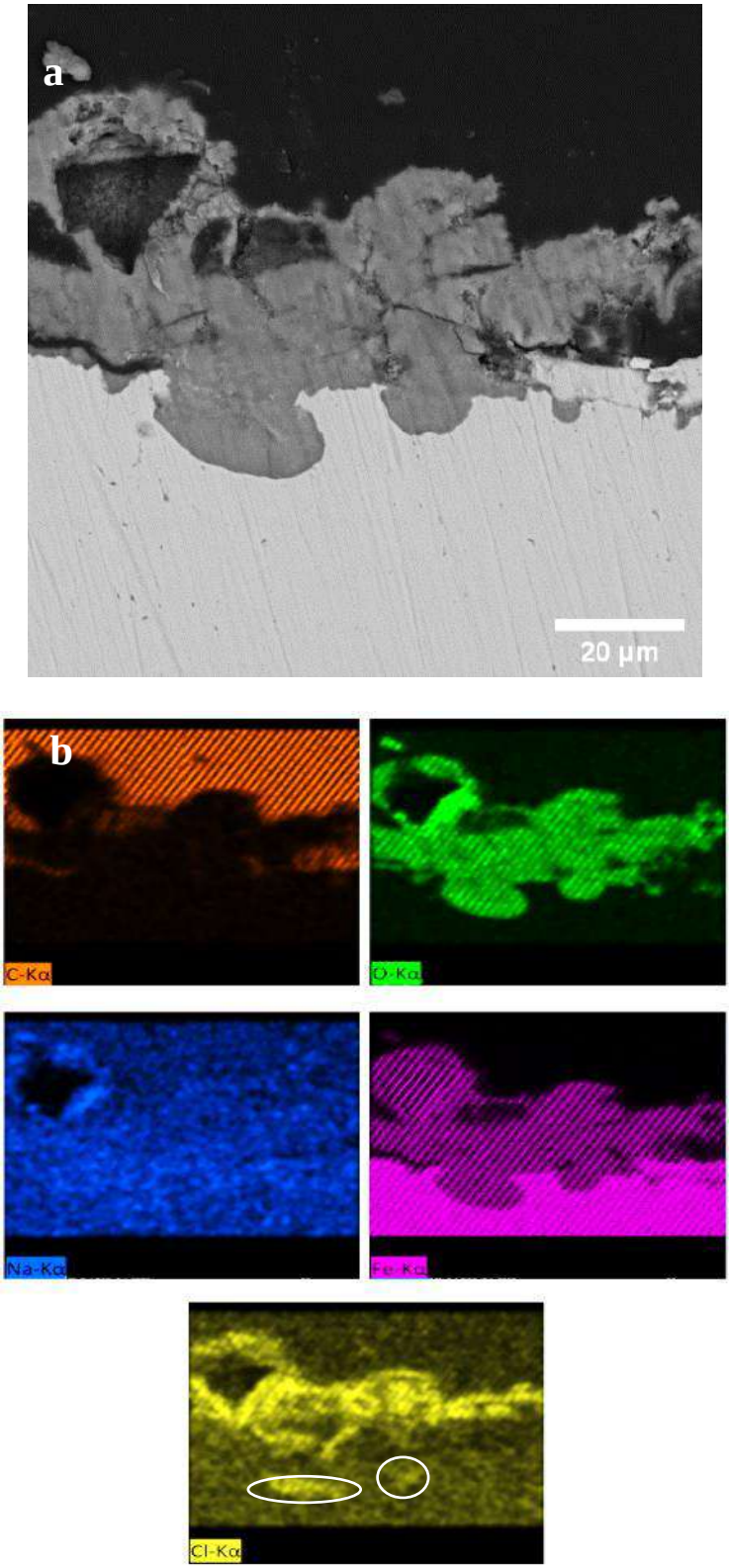


Figure 34 – (a) SEM image of cross-sectioned sample Type 3 tested at 40 °C and 3.5 wt.% NaCl showing localized corrosion. (b) SEM maps highlighting siderite formation and presence of element Cl in localized corrosion tip.

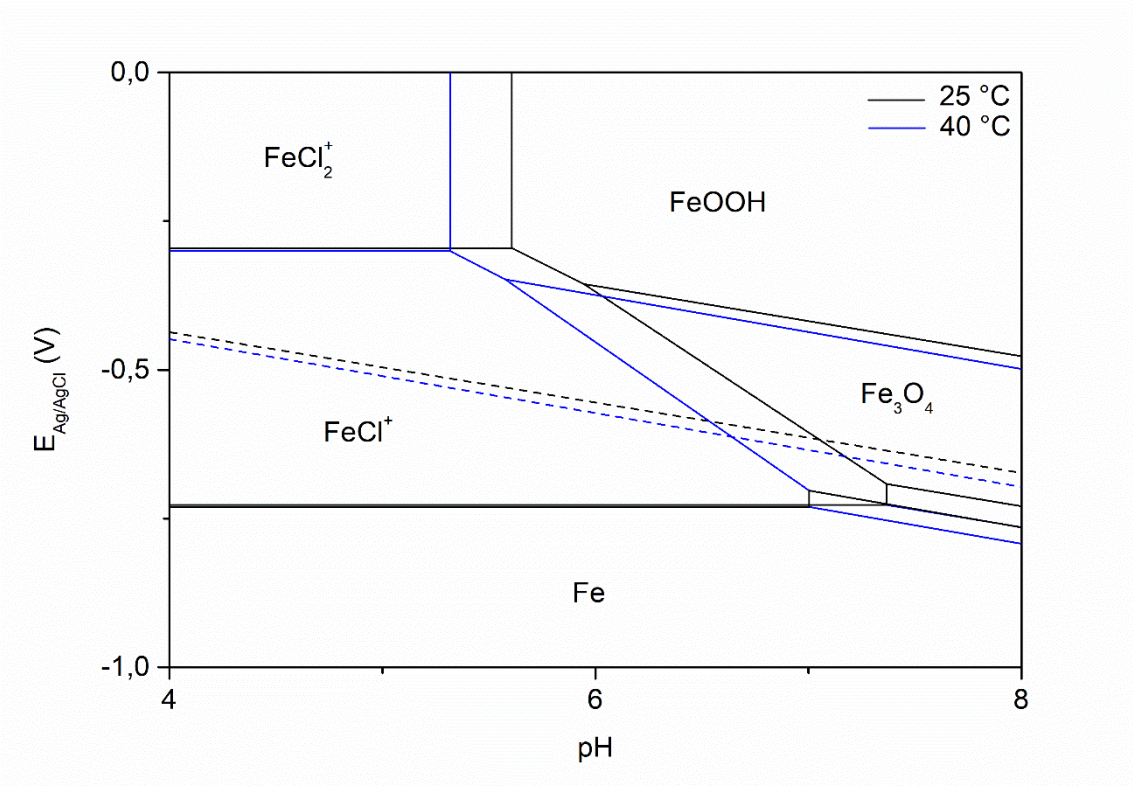
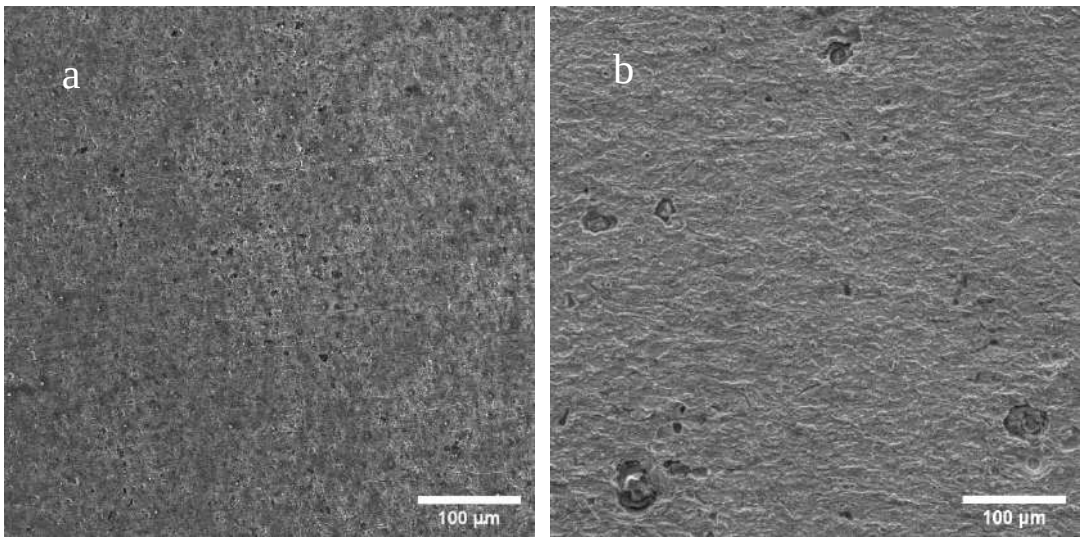


Figure 35 - Pourbaix diagram for the Fe-CI-H_2O system at 25 and 40 °C and 1.6 M NaCl.



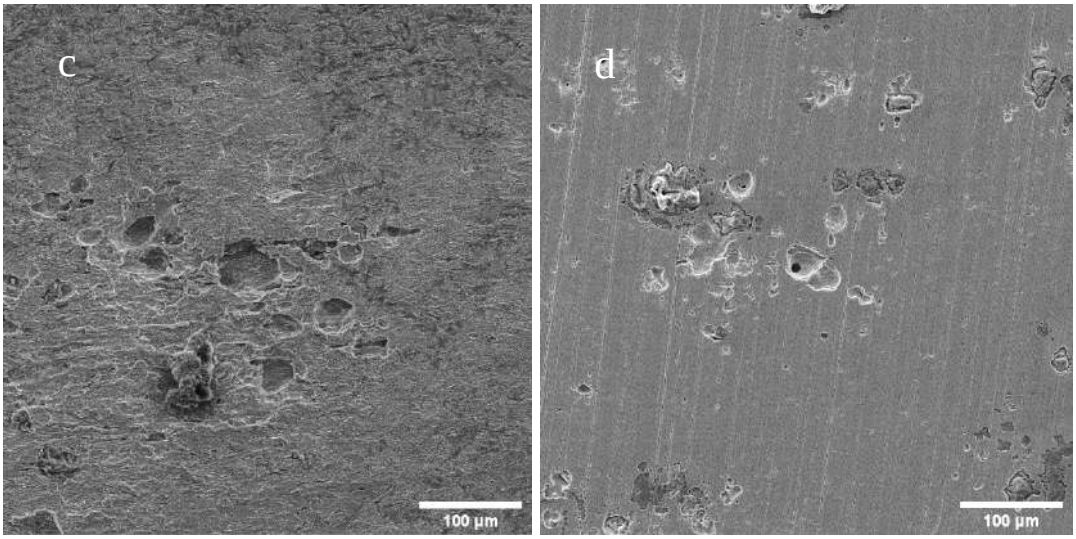


Figure 36 – SEM images of stripped Type 3 steels tested at (a) 0.1 wt.%NaCl 25 °C; (b) 0.1 wt.%NaCl 40 °C; (c) 3.5 wt.%NaCl 25 °C; and (d) 3.5 wt.%NaCl 40 °C.

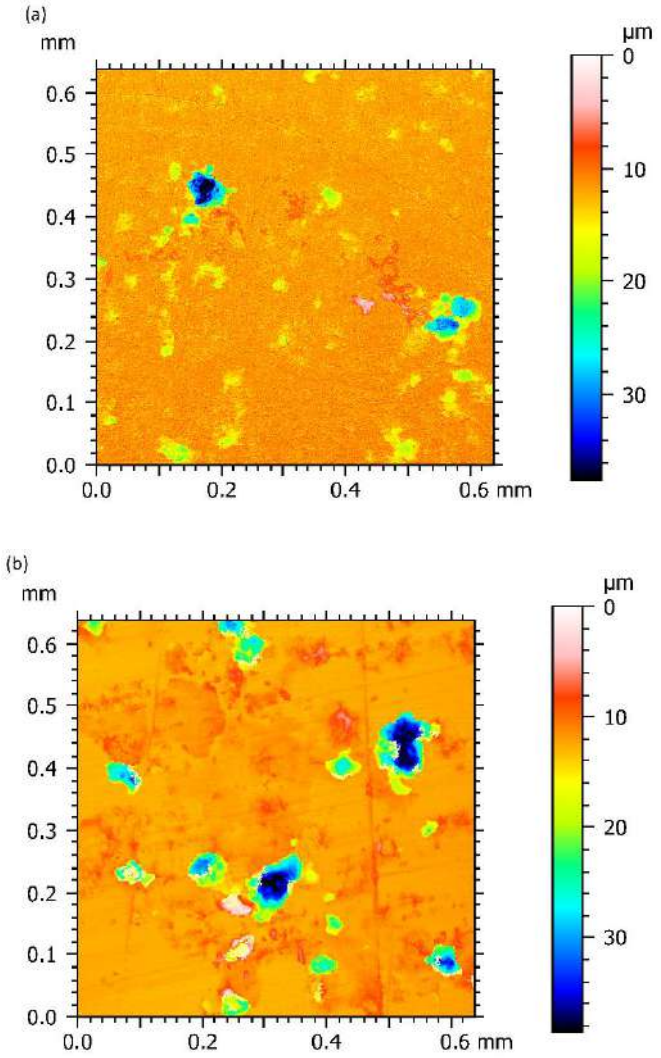


Figure 37 – Confocal microscopy showing depth profile of steel Type 3 tested in brine at (a) 25 °C; and (b) 40 °C, revealing localized corrosion.

4.4. Corrosion in bared samples

In order to assess the effect of film free surfaces on the corrosion behavior of the steel wires at near neutral pH, the tests listed in Table 5 and Table 6 were carried out. In such tests, the alkalinity of the solution was adjusted with the addition of sodium bicarbonate to prevent, or at least delay, the formation of siderite, although maintaining the pH at near neutral values. As they did not show a significant change in the corrosion rate during the tests, the B values used for calculations were more accurate and the results are discussed below.

According to the tests which the influence of temperature and salinity were taken into account (Table 5), the samples in acidic stage and 40 °C showed corrosion rates about 2 times higher than those tested at 25 °C, with values ca. 0.4 and 0.7 $mm.^{-1}$, respectively (Figure 38). In such stage, the pH was about 5 and no film was expected to form on the surface. The high temperature accelerated chemical and electrochemical reactions, in addition to speed up the mass transfer process by decreasing the viscosity of solution. Thus, increased the corrosion rate (HATAMLEH *et al.*, 2009, HONARVAR NAZARI *et al.*, 2010).

As a second step, sodium bicarbonate ($NaHCO_3$) with purity greater than 99% was added. In all scenarios the pH reached values close to 7 and then the effect of pH was analyzed. The increase of pH for about 36 h of test was not enough to stabilize the corrosion rate of the materials. The tests at 40 °C showed a drop-in corrosion rate of approximately 0.016 $mm.y^{-1}.h^{-1}$, reaching values below 0.2 $mm.y^{-1}$ at the end of the test, regardless of the salinity condition of the solution. At 25 °C and 0.1 wt.% NaCl this value remained practically unchanged. However, the brine condition at 25 °C showed an increase in the corrosion rate after the addition of sodium bicarbonate.

The CR reduction in tests carried out at 40 °C may be related to the fast formation of iron hydroxides on the steel surfaces, which conferred a greenish color to the solution. In addition, some siderite could precipitate under such temperature by the dissolution of the steel in presence of high alkalinity, rapidly raising the $SR_{(siderite)}$ to values above 1. Such layers could have served as a mass transfer barrier for the cations present in solution. At 25 °C, such solids were suppressed for longer and the pH increase was not sufficient to protect the steel.

Thus, at pH 5 the carbonic acid is the dominant cathodic reaction, while at near neutral pH the bicarbonate reduction becomes important, acting as a main oxidizing agent of bare steels until conditions for protective layer formation are reached (HONARVAR NAZARI *et al.*, 2010). NaCl did not present evidences of being determinant for corrosion morphologies. All conditions presented general corrosion up to 0.3 $mm.y^{-1}$ at the end of the tests. However, the CR under brine showed values slighter higher for both tested temperatures. If correlate such scenarios with a possible active localized corrosion tip, the steel dissolution rate can present an order of the CR values greater than the expected in annulus. These values may be even superior considering the effect of galvanic pair with the non-active areas around it, regardless of the pH (if acid or neutral).

EIS slopes with Nyquist and Bode plots complement the finds in LPR results, and are shown in Figure 39. The capacitive slopes for both, at acidic and near neutral stages, presented a single semicircle in Nyquist plot and an increment of phase change displaced to lower frequencies in Bode plots. They were associated with film free surface and are attributed to the non-ideal double layer capacitance (Q_{dl}), the polarization resistance (R_p) and the solution resistance (R_s), which provides a simple EEC for uniform corrosion (Figure 40). The samples tested at 25 °C presented an increase in the capacitive loops as soon as the sodium bicarbonate was added (red lines). After that, the material tested in 3.5 wt.% NaCl solution decreased R_p after 48 h of exposure, which characterizes the active state of the interface. The capacitive slope of the material exposed to 0.1 wt.% NaCl solution basically showed no change while at near neutral pH. Both samples tested at 40 °C presented an important increase of the capacitive semicircles at the end of the near neutral stage. This was attributed to a mass transfer barrier due to adsorbed species and solid particles, as mentioned in discussions related to LPR. The Rs for low salinity conditions were higher and had an important decrease after the sodium bicarbonate ingress, which increased the ionic strength.

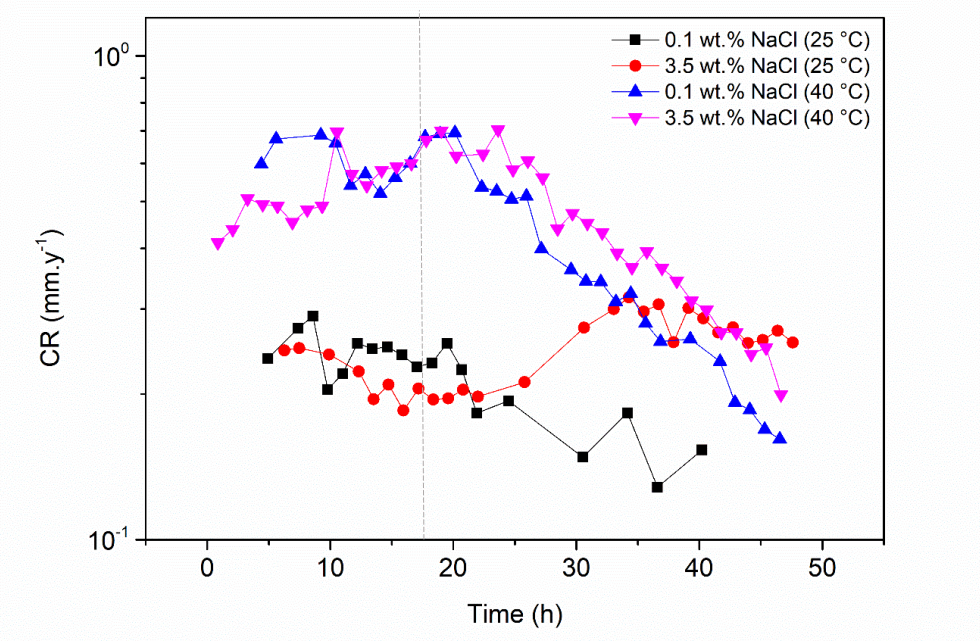
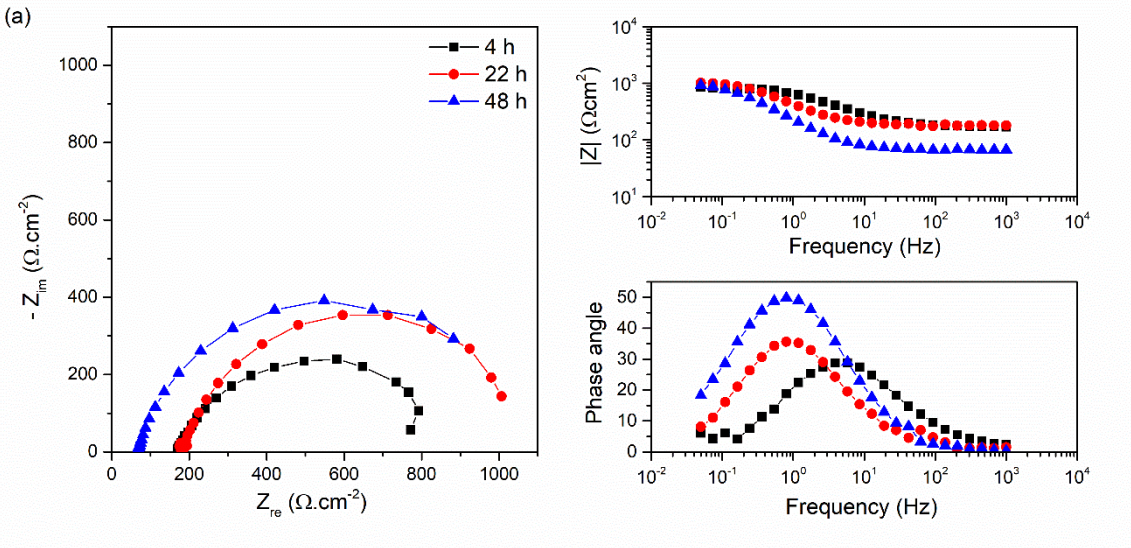


Figure 38 – Corrosion rate of Type 3 steel during the acid stage (on the left side of the line), and at near neutral pH by the addition of $NaHCO_3$ (on the right side of the line).



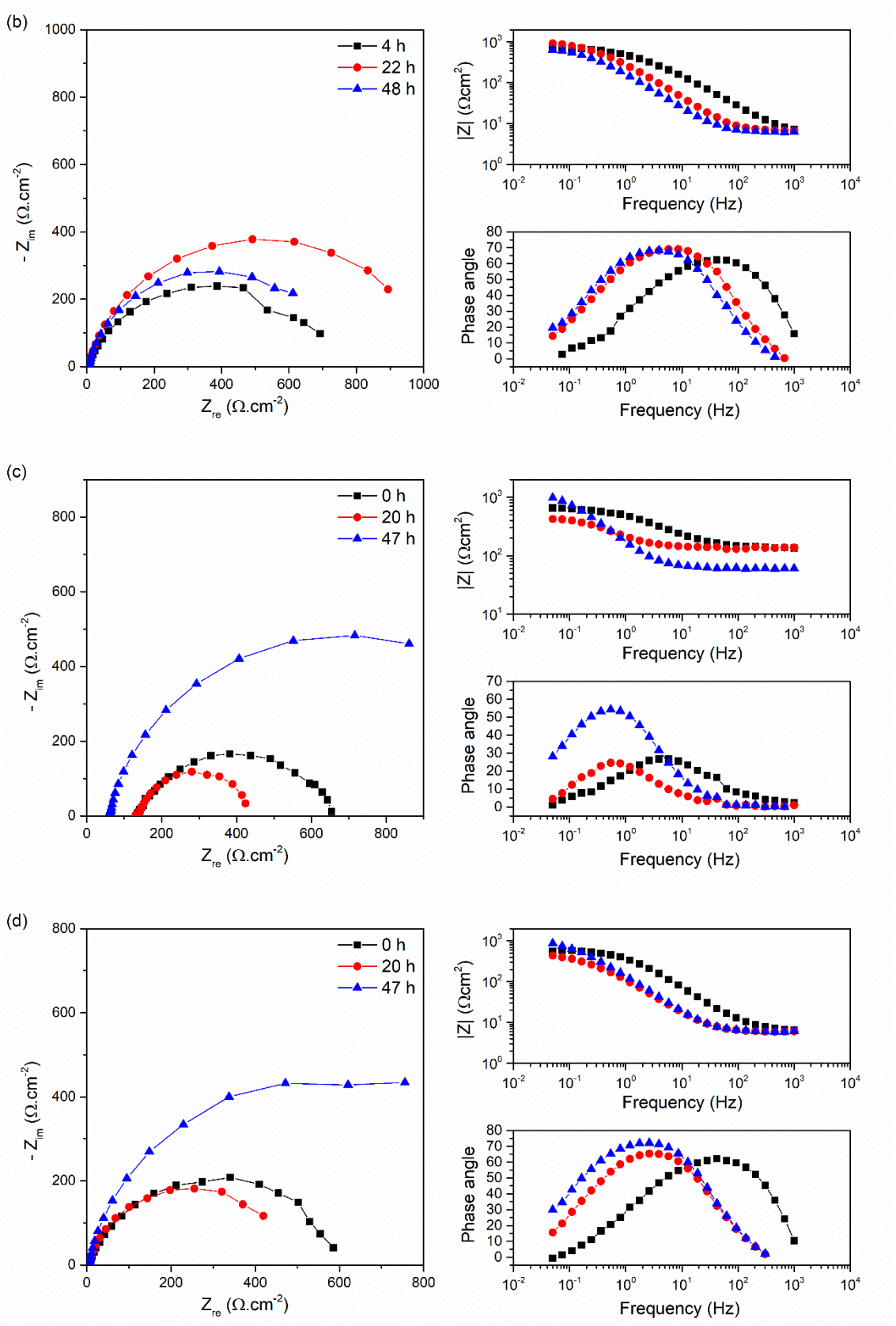


Figure 39 – Nyquist and Bode impedance spectra recorded for the tests carried out in bare steels under conditions shown in Table 5. The black line is related to the acidic stage; the red and blue lines were recorded after sodium bicarbonate addition. (a) 0.1

wt.%NaCl 25 °C; (b) 3.5 wt.%NaCl 25 °C; (c) 0.1 wt.%NaCl 40 °C; and (d) 3.5 wt.%NaCl 40 °C.

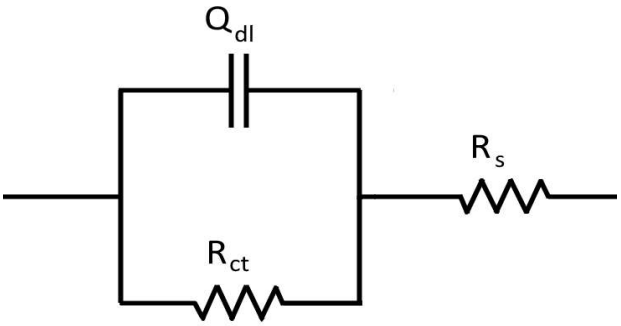
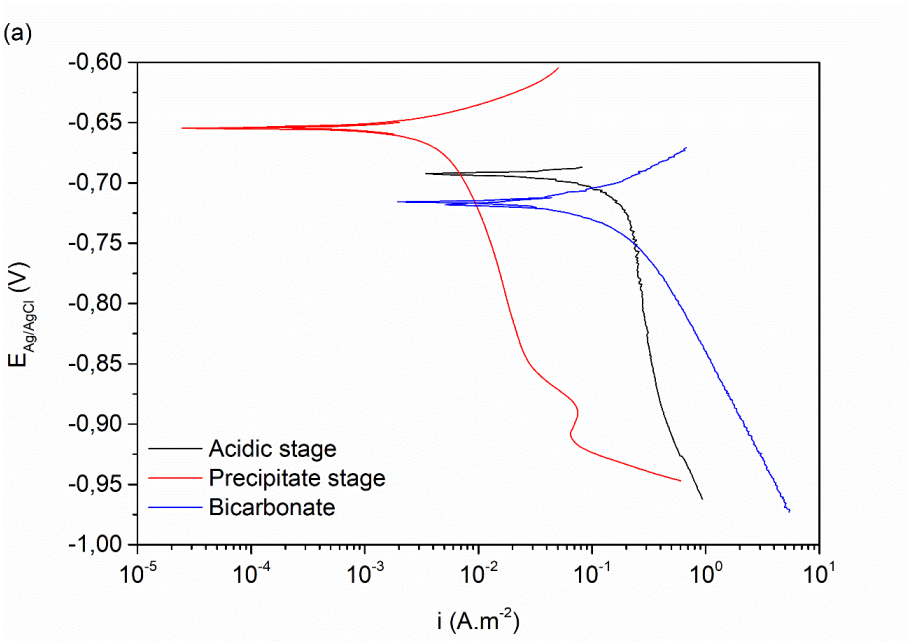
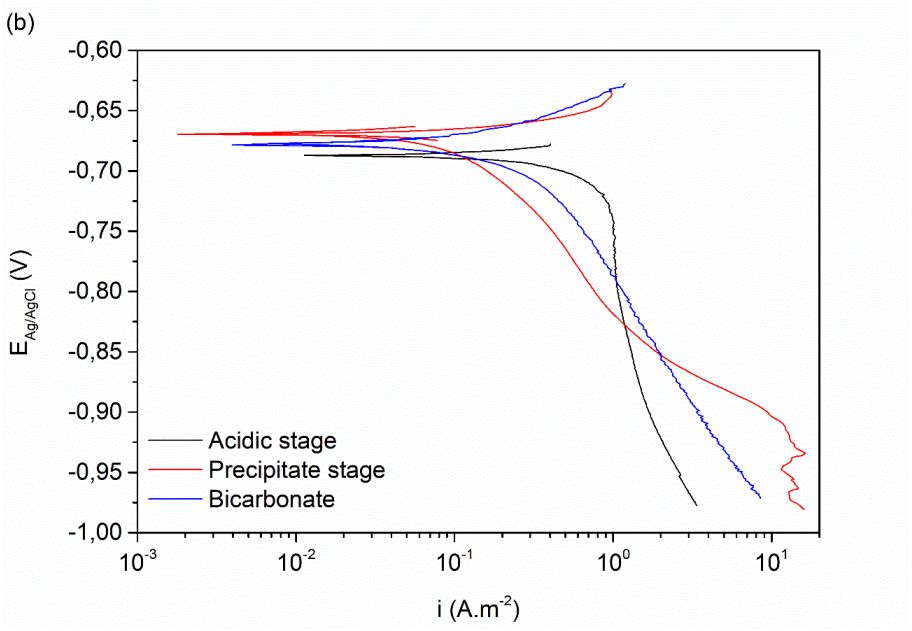


Figure 40 – ECC for modelling the impedance spectra shown in Figure 39.

To better understand the effect of pH, the polarization curves performed with pH 5 were related to those obtained at near neutral pH, not only by the presence of ferrous ions (layered surface) but also through the addition of sodium bicarbonate (bare surface) (Figure 41). The slopes were recorded at the end of each stage, as presented in Table *4* and Table *5* . In all following charts the polarization slopes presented diffusion control behavior at potentials below OCP. Under over potentials in tests at high alkalinities, the decrease in slopes means that the cathodic current increased. This suggests that some cathodic species may be reduced supplying with additional H^+, such as bicarbonate ions, regardless of whether the steel surfaces are covered or not.

Increasing bicarbonate concentration, by $NaHCO_3$ addition, did not shift the OCP significantly, nor did it reduce the current density. This is in line with the low changes in CR in bare steel tests and the corrosive effect of bicarbonate (Figure 38) (HAN *et al.*, 2011b). However, in conditions that siderite precipitated, there was a shift in slopes to low cathodic currents. It is assumed that both, bicarbonate consumption and siderite layer formation, contributed to the activation controlled of cathodic currents close to OCP. The curves also changed to high potentials direction which indicates a pseudo-protection of the mild steel surface. This protection is usually attributed to a second phase formed between the steel and siderite, the magnetite (HAN *et al.*, 2011a). This behavior was less pronounced in the sample tested at 25 °C and 3.5 wt.% NaCl (Figure 41 (b)). In such case, the formation of a diffusional barrier is the most likely.


(a)
-0,60
-0,65
-0,70
-0,75
-0,80
-0,85
-0,90
-0,95
-1,00
E Ag/AgCl (V)
Acidic stage
Precipitate stage
Bicarbonate
10-5
10-4
10-3
10-2
10-1
100
101
i (A.m-2)


(b)
-0,60
-0,65
-0,70
-0,75
-0,80
-0,85
-0,90
-0,95
-1,00
E Ag/AgCl (V)
Acidic stage
Precipitate stage
Bicarbonate
10-3
10-2
10-1
100
101
i (A.m-2)

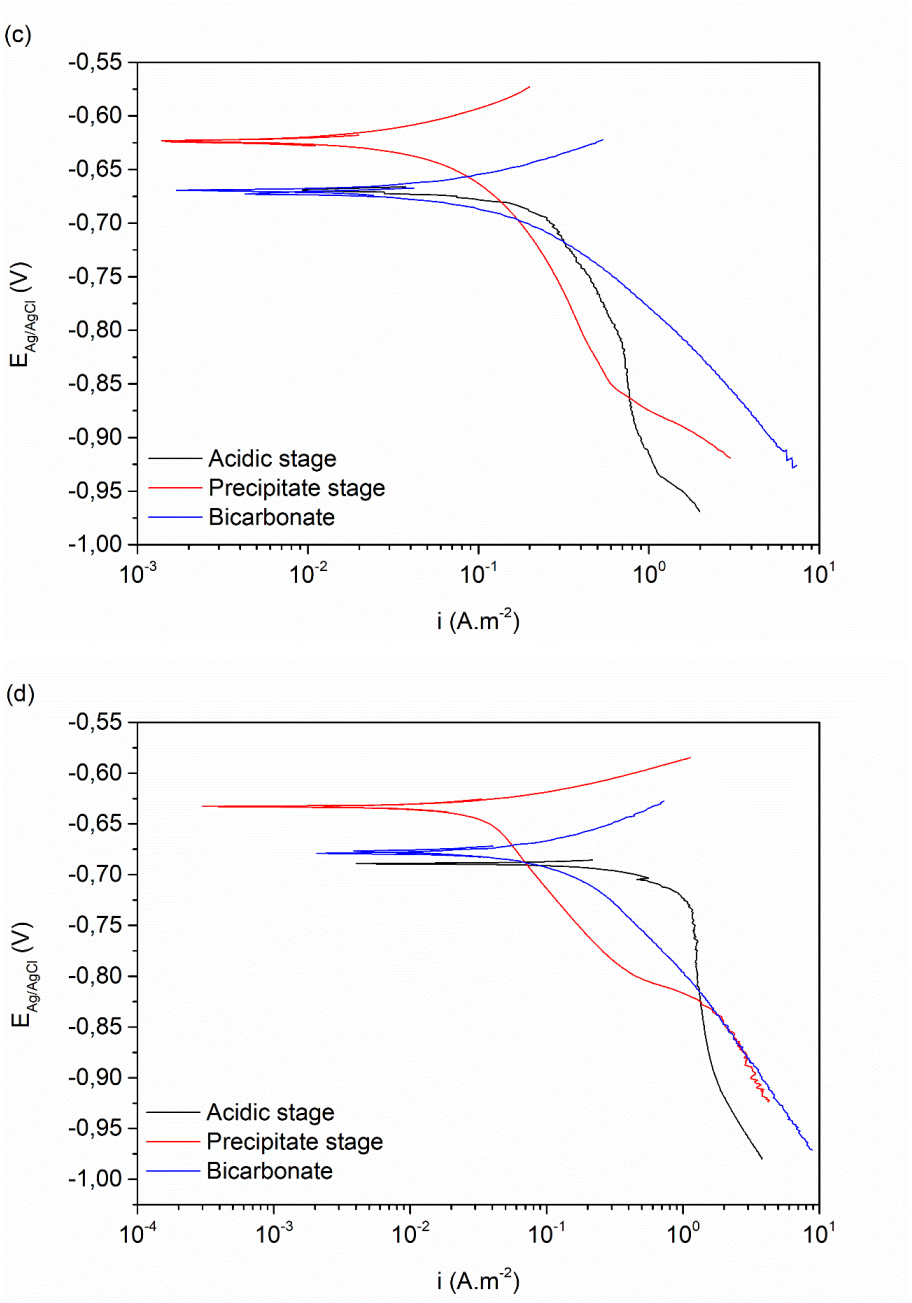


Figure 41 – Polarization sweeps for steel Type 3 during acidic stage (black), precipitation stage (red) and in presence of NaHCO3 (blue) recorded at the end of the corresponding stage. (a) 0.1 wt.% NaCl at 25 °C; (b) 3.5 wt.% NaCl at 25 °C; (c) 0.1 wt.% NaCl at 40 °C; and (d) 3.5 wt.% NaCl at 40 °C.

According to the previous results, only the increase in pH was not enough to reduce the corrosion rate of carbon steels. Therefore, a further investigation was carried out on which parameter directly influences the corrosion rate of bare steels at near neutral pH range. For that, pCO_2, alkalinity and pH varied in a fixed temperature (25 °C) and solution, composed by artificial seawater (ASTM D1141, 2003) without Ca, Sr and Mg to avoid precipitation, as described in Table *6*. The choice of temperature was based on the later

formation of precipitates. High salinity was chosen because it increases the solubility of the siderite, and is the most likely condition to be found in the annulus related to corrosion issues. For that, the armor wire steel Type 2 and a well-known carbon steel X65 (Ref.) were tested.

Although the three parameters are interdependent, the charts in Figure 42 show that the corrosion rate of both materials varied proportional only in relation to pCO_2. Thus, in electrochemically active sites in annulus, such as in precipitate gaps or at localized corrosion tips, the pCO_2 is the ruling factor that influences the evolution of corrosion. Alkalinity and pH were not identified individually important to the process because they did not exhibit a clear trend in the charts. The summary of the test parameters and CR of the materials are shown in Table 10.

The steel wire Type 2 clearly presented higher CR than Ref from 0.1 bar CO_2. This may be related to the chemical composition of the material, since Ref. has about twice the amount of Mn. The Mn improve of the corrosion behavior of steels by increasing the corrosion potential and reducing the corrosion current density.(XIAOYAN *et al.*, 2014) Another possibility is the difference in carbon content. The Type 2 has 0.66 wt.% C, and Ref. has only 0.08 wt.% C. This impact directly on the microstructure, which make easier the pearlite formation in Type 2 steel. Pearlite is a constituent formed for lamellar ferrite and cementite. The last acts as a cathodic site around an anodic ferrite. Therefore, a high corrosion rate is expected in carbon steels with higher carbon and low alloy content.

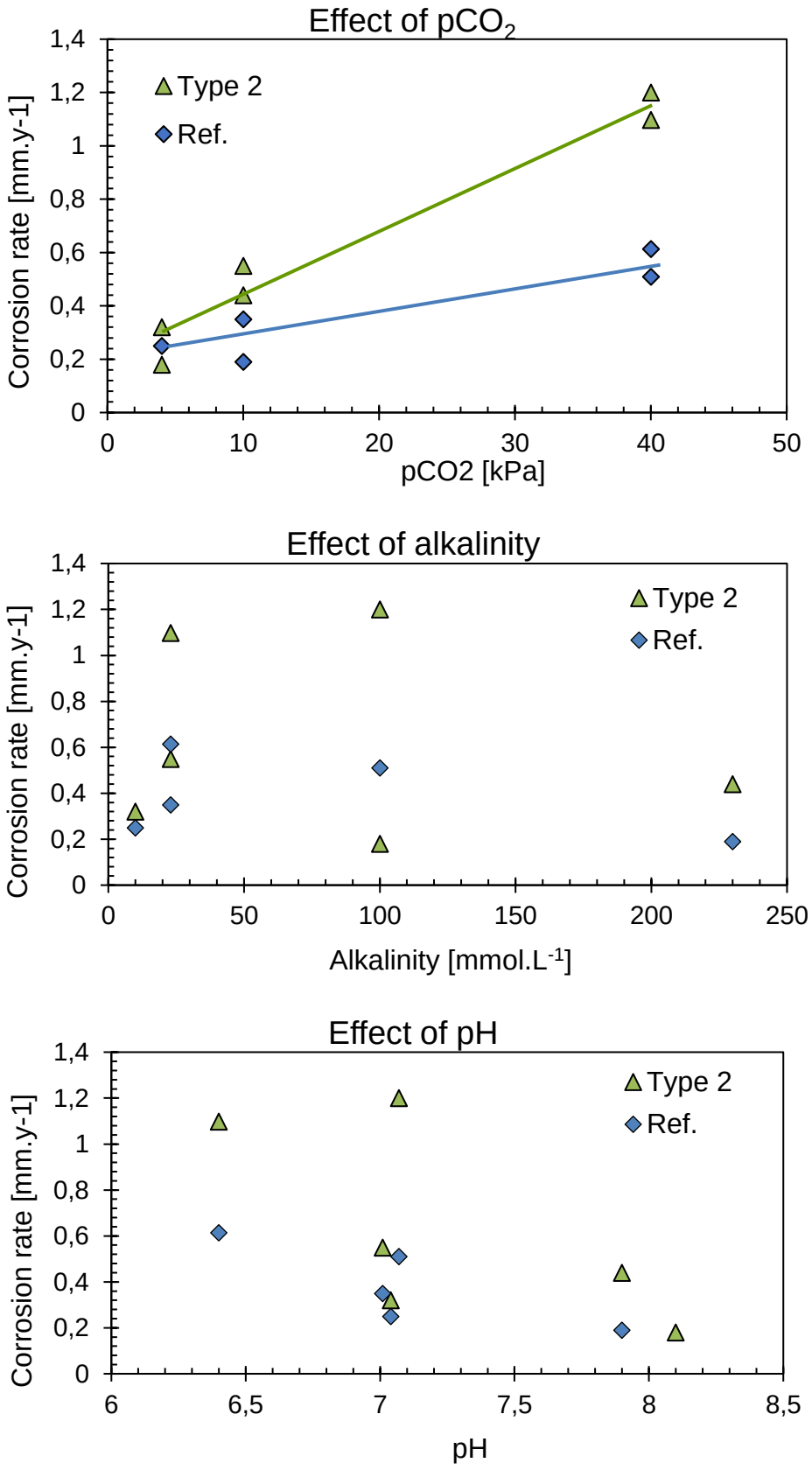


Figure 42 – The effect of pCO2, alkalinity and pH on bare steels Type 2 and Ref. under near neutral pH.

Table 10 – CR of the tested steels Type 2 and Ref. by varying pCO_2, alkalinity and pH in artificial seawater.

pH	$NaHCO_3$ (mmol.kg^{-1})	pCO_2 (kPa)	LPR results (mm.y-1)	
			Type 2	Ref.
7.07	100	40	1.20	0.51
8.10	100	4	0.18	-
7.04	10	4	0.32	0.25
7.01	23	10	0.5	0.35
6.40	23	40	1.10	0.61
7.90	230	10	0.44	0.19

5. CONCLUSIONS

- The nucleation and growth of siderite are so slow that the water solutions in occluded spaces, as in flexible pipes, can stay supersaturated and maintain a near neutral pH condition for weeks when the temperature is low. The pH was still above 7 when the 10 and 15 °C experiments were stopped after 22 and 17 days, respectively. The precipitation rate increases with temperature and a lower pH was observed after 10 days exposure at 25 °C (pH 6.8) and 40 °C (pH 6.4).

- The morphology of the protective layer depends on the composition of the electrolyte. In 0.1 wt.% NaCl solution, the samples were completely covered with siderite pyramids clustered in a sphere shape with platelets of chuckanovite on top. Pyramidical crystals of siderite with calcium ($(Fe,Ca)CO_3$) formed in artificial seawater. The layer formed in 0.1 wt.% NaCl solution was three times thicker than the layer formed in artificial seawater at otherwise identical conditions.

- At 25 °C, high strength carbon steels develop protective layers at the surface after short time when they corrode in solutions supersaturated with siderite. Fully protective layers reduce the corrosion rate to less than 0.01 mm.y^{-1} in 24 h when the $SR_{(siderite)}$ is above 1000. The cathodic reaction becomes limited by diffusion through the layer.

- The initial surface conditions, “as received” or “machined”, and differences in microstructure of the steel wires are a secondary factor and have little impact on the

morphology of the protective layer and the corrosion rate in steels submitted only to near neutral pH solutions.

- High salinity (3.5 wt.%NaCl), low temperature (< 40 °C) and pre-corroded areas with cementite are conditions that enhance corrosion rate in steel armors and localized corrosion formation.

- The formation of siderite is followed by its partial dissolution in brine and/or low temperatures.

- The possibility of $FeCl^+$ formation in localized corrosion tips indicates the deleterious action of NaCl can cause in steel armors not fully protected by the siderite. The corrosion rate in its active (bared) areas may be one order higher than encountered in global measurements regardless the pH, if acidic or near neutral.

- At near neutral pH and 25 °C, pCO_2 is the main parameter that controls corrosion rate of bare steels. Alkalinity and pH are not individually relevant, as bicarbonate ions may be a source of protons in place of carbonic acidic.

- The increase in carbon content and differences in microstructure influence the corrosion rate of carbon steels in CO_2 systems at near neutral pH levels by forming more cathodic sites (cementite) nearby to anodic ferrite.

6. SUGGESTIONS FOR FUTURE WORK

- Study the influence of higher CO_2 pressures, lower temperatures and salinity simulating annulus conditions in relation to corrosion morphology and chemical and electrochemical evolution.
- Evaluate the influence of near neutral pH on zeta wires.
- Perform mechanical tests of the steel wires to assess the possibility of SCC in the annulus based on fundamental understandings of the layer rupture mechanism.
- Analyze how cathodic protection can influence both, the annulus environment and the mechanical properties of steel wires.

7. REFERENCES

"ASTM G1-03 Standard Practice for Preparing, Cleaning, and Evaluating Corrosion Test Specimens". , 2017. "ASTM G1-03 Standard Practice for Preparing, Cleaning, and Evaluating Corrosion Test Specimens". . 2017. S.l.: s.n.

AL-HASSAN, S., MISHRA, B., OLSON, D.L., et al., 1998, "Effect of Microstructure on Corrosion of Steels in Aqueous Solutions Containing Carbon Dioxide". In: *Corrosion*. v. 54, pp. 480–491.

ALAM, M.T., CHAN, E.W.L., DE MARCO, R., et al., 2016, "Electrochemical and Surface Analysis Studies on the Carbon Dioxide Corrosion of X-65 Carbon Steel". In: *Electroanalysis*. v. 28, pp. 2910–2921.

AMERICAN PETROLEUM INSTITUTE, 2008. "API RP 17B Recommended Practice for Flexible Pipe". . 2008. S.l.: s.n. Disponível em: <http://scholar.google.com/scholar?hl=en&btnG=Search&q=intitle:Recommended+Practice+for+Flexible+Pipe#0>.

AMUNDSEN, T., NILSEN-AAS, C., KANESTRØM, Ø., et al., 2017, "Digitizing flexible riser annulus testing By automated portable test equipment". In: *Proceedings of the Annual Offshore Technology Conference*. v. 1, pp. 147–154.

ASHER, S.L., LEIS, B., COLWELL, J., et al., 2007, "Investigating a mechanism for transgranular stress corrosion cracking on buried pipelines in near-neutral pH environments". In: *Corrosion*. v. 63, pp. 932–939.

ASTMD1141, 2003. "Standard Practice for the Preparation of Substitute Ocean Water". . 2003. S.l.: s.n.

BAI, Y., BAI, Q., 2005, *Subsea Pipelines and Risers*. . S.l., s.n.

BAI, Y., BAI, Q., 2010a, *Subsea Engineering Handbook*. . USA, s.n.

BAI, Y., BAI, Q., 2010b, *SUBSEA STRUCTURAL ENGINEERING HANDBOOK*. . S.l., s.n.

BAPTISTA, W., 1985. *Estudo sobre as características químicas e eletroquímicas das soluções existentes no interior de cavidades de corrosão localizada do Incoloy 800*. . S.l.: UFRJ.

BATISTA, G.Z., SILVA, R.D.A., JÚNIOR, E.H., et al., 2007, "DETERMINAÇÃO DOS PARÂMETROS PARA O CURVAMENTO A QUENTE E TRATAMENTO TÉRMICO DE TUBOS API 5L X80". In: *Rio Pipeline Conference & Exposition*. pp. 1–8.

BEAVERS, J.A., JASKE, C.E., 1998. "Near-neutrak pH SCC in pipelines: Effects of pressure fluctuations on crack propagation". In: *Corrosion*. S.l.: s.n. 1998.

BÉNÉZETH, P., DANDURAND, J.L., HARRICHOURY, J.C., 2009, "Solubility product of siderite (FeCO3) as a function of temperature (25-250 °C)". In:

Chemical Geology. v. 265, pp. 3–12.

BERGE, S., ENGSETH, A., FYLLING, I., et al., 2017, *Handbook on Design and Operation of Flexible Pipes*. . S.l., s.n.

BERNTSEN, T., 2017. *CO2 Corrosion of Carbon Steel in pH Stabilised Multiphase Pipelines*. . S.l.: University of Stavanger.

BERNTSEN, T., SEIERSTEN, M., HEMMINGSEN, T., 2013, "Effect of FeCO3 supersaturation and carbide exposure on the CO2 corrosion rate of carbon steel". In: *Corrosion*. v. 69, pp. 601–613.

BOGDANOV, R.I., UNIGOVSKI, Y.B., GUTMAN, E.M., et al., 2019, "Stress corrosion cracking of pipeline steels in near-neutral pH solutions: The role of mechanochemical and chemomechanical effects". In: *AIMS Materials Science*. v. 6, pp. 1065–1085.

BORRE, M.K., COFFEY, B.P., 2014. "Multi-stage cleaning for routine core analysis in heavy oil-bearing carbonates, Campos Basin, Brazil". In: *Society of Petroleum Engineers*. S.l.: s.n. 2014. pp. 1801–1809.

BRAUN, R.D., 1991, "Solubility of iron(II) carbonate at temperatures between 30 and 80°". In: *Talanta*. v. 38, pp. 205–211.

BURKLE, D., DE MOTTE, R., TALEB, W., et al., 2017, "In situ SR-XRD study of FeCO3 precipitation kinetics onto carbon steel in CO2-containing environments: The influence of brine pH". In: *Electrochimica Acta*. v. 255, pp. 127–144.

CAMPOS, T., SEIERSTEN, M., PALENCSÁR, S., et al., 2021, "Corrosion of High-Strength Carbon Steels in Siderite Supersaturated Water at Near Neutral pH". In: *Corrosion*. v. 77, pp. 632–645.

CEPA, 2015, "CEPA Recommended Practices for Managing Near-neutral pH Stress Corrosion Cracking 3 rd edition". In: .

CHEN, W., 2016, "An Overview of Near-Neutral pH Stress Corrosion Cracking in Pipelines and Mitigation Strategies for Its Initiation and Growth". In: *Corrosion*. v. 72, pp. 962–977.

CHEN, W., KING, F., JACK, T.R., et al., 2002a, "Environmental aspects of near-neutral pH stress corrosion cracking of pipeline steel". In: *Metallurgical and Materials Transactions A: Physical Metallurgy and Materials Science*. v. 33, pp. 1429–1436.

CHEN, W., KING, F., VOKES, E., 2002b, "Characteristics of near-neutral-pH stress corrosion cracks in an X-65 pipeline". In: *Corrosion*. v. 58, pp. 267–275.

CLOVER, D., KINSELLA, B., PEJCIC, B., et al., 2005, "The influence of microstructure on the corrosion rate of various carbon steels". In: *Journal of Applied Electrochemistry*. v. 35, pp. 139–149.

CORCORAN, J., DAVIES, C.M., CAWLEY, P., et al., 2019, "A Quasi-DC Potential

Drop Measurement System for Material Testing". In: *IEEE Transactions on Instrumentation and Measurement*. v. 69, pp. 1313–1326.

CROLET, J.L., THEVENOT, N., NESIC, S., 1998, "Role of Conductive Corrosion Products in the Protectiveness of Corrosion Layers". In: . pp. 194–203.

DUGSTAD, A., 1998. "MECHANISM OF PROTECTIVE FILM FORMATION DURING CO2 CORROSION OF CARBON STEEL". In: *Corrosion*. S.l.: s.n. 1998.

DUGSTAD, A., 2015, "Fundamental Aspects of CO2 Metal Loss Corrosion, Part I: Mechanism". In: *Corrosion 2015, NACE*. pp. 1–12.

DUGSTAD, A., HEMMER, H., SEIERSTEN, M., 2000, "Effect of steel microstructure upon corrosion rate and protective iron carbonate film formation". In: *NACE - International Corrosion Conference Series*. v. 2000-March, pp. 369–378.

DUGSTAD, A., HEMMER, H., SEIERSTEN, M., 2001, "Effect of steel microstructure upon corrosion rate and protective iron carbonate film formation". In: *Corrosion 2001*. v. 57, pp. 369–378.

DUGSTAD, A., MORLAND, B., CLAUSEN, S., 2011, "Corrosion of transport pipelines for CO2–Effect of water ingress". In: *Energy Procedia*. v. 4, pp. 3063–3070.

DUGSTAD, A., PALENCSÁR, S., BERNTSEN, T., et al., 2018, "Corrosion of steel armour wires in flexible pipes - History effects". In: *Society of Petroleum Engineers - SPE International Oilfield Corrosion Conference and Exhibition 2018*. pp. 18–19.

DUGSTAD, A., PALENCSAR, S., BORVIK, L., et al., 2015. "Corrosion Testing of Steel Armour Wires in Flexible Pipes – A Parametric Study". In: *CORROSION 2015*. S.l.: NACE International. 2015. pp. 1–11.

DUGSTAD, A., PALENCSÁR, S., SVENNINGSEN, G., et al., 2020. "The combined effect of O2 and CO2 on corrosion of flexible armour wires". In: *CORROSION 2020*. S.l.: NACE International. 2020. pp. 1–15.

ESMAEELY, S.N., CHOI, Y., YOUNG, D., et al., 2013, "Effect of Calcium on the Formation and Protectiveness of Iron Carbonate Layer in CO2 Corrosion". In: *Corrosion, NACE*. pp. 1–13.

FELIU, S., GARCÍA-GALVAN, F.R., LLORENTE, I., et al., 2017, "Influence of hydrogen bubbles adhering to the exposed surface on the corrosion rate of magnesium alloys AZ31 and AZ61 in sodium chloride solution". In: *Materials and Corrosion*. v. 68, pp. 651–663.

FERREIRA, L.R.M., KLOK, S.M., PONTE, H.A., et al., 2016, "A FORMAÇÃO DA CAMADA PROTETORA DE FeCO3 E O CONTROLE DA CORROSÃO POR CO2 EM CONDIÇOES DE FLUXO TURBULENTO". In: *Quim. Nova*. v. 39, pp. 1027–1033.

FIORAVANTE, I.A., NUNES, R.S., ACCIARI, H.A., et al., 2019, "Films formed on carbon steel in sweet environments - A review". In: *Journal of the Brazilian Chemical Society*. v. 30, pp. 1341–1349.

GADALA, I.M., ALFANTAZI, A., 2015, "Low Alloy X100 Pipeline Steel Corrosion and Passivation Behavior in Bicarbonate-Based Solutions of pH 6.7 to 8.9 with Groundwater Anions: An Electrochemical Study". In: *Metallurgical and Materials Transactions A: Physical Metallurgy and Materials Science*. v. 46, pp. 3104–3116.

GAO, X., BROWN, B., NESIC, S., 2014. "Effect of Chloride on Localized Corrosion Initiation of Carbon Steel in a CO2 Aqueous Environment". In: *Corrosion*. S.l.: s.n. 2014. pp. 1–14.

GIL, P.M., PALOMAR-PARDAVÉ, M., DE OCA-YEMHA, M.G.M., et al., 2018, "Effect of carbonate and chloride ions on the corrosion susceptibility of pipeline steel samples artificially aged". In: *International Journal of Electrochemical Science*. v. 13, pp. 1844–1858.

GRAY, L.G.S., ANDERSON, B.G., 1990. "Effect of pH and temperature on the mechanism of carbon steel corroison by aqeous carbon dioxide". In: *NACE International*. S.l.: s.n. 1990. pp. 1–26.

GU, B., LUO, J., MAO, X., 1999, "Hydrogen-facilitated anodic dissolution-type stress corrosion cracking of pipeline steels in near-neutral pH solution". In: *Corrosion*. v. 55, pp. 96–106.

HAN, J., BROWN, B.N., NEŠIĆ, S., 2010, "Investigation of the galvanic mechanism for localized carbon dioxide corrosion propagation using the artificial pit technique". In: *Corrosion Journal*. v. 66, pp. 0950031–09500312.

HAN, J., NEŠIĆ, S., YANG, Y., et al., 2011a, "Spontaneous passivation observations during scale formation on mild steel in CO2 brines". In: *Electrochimica Acta*. v. 56, pp. 5396–5404.

HAN, J., ZHANG, J., CAREY, J.W., 2011b, "Effect of bicarbonate on corrosion of carbon steel in CO2 saturated brines". In: *International Journal of Greenhouse Gas Control*. v. 5, pp. 1680–1683.

HATAMI, S., GHADERI-ARDAKANI, A., NIKNEJAD-KHOMAMI, M., et al., 2016, "On the prediction of CO2 corrosion in petroleum industry". In: *The Journal of supercritical fluids*. v. 117, pp. 108–112.

HATAMLEH, O., SINGH, P.M., GARMESTANI, H., 2009, "Corrosion susceptibility of peened friction stir welded 7075 aluminum alloy joints". In: *Corrosion Science*. v. 51, pp. 135–143.

HEUER, J.K., STUBBINS, J.F., 1999, "An XPS characterization of FeCO3 films from CO2 corrosion". In: *Corrosion Science*. v. 41, pp. 1231–1243.

HONARVAR NAZARI, M., ALLAHKARAM, S.R., KERMANI, M.B., 2010, "The effects of temperature and pH on the characteristics of corrosion product in CO2

corrosion of grade X70 steel". In: *Materials and Design*. v. 31, pp. 3559–3563.

IAEA, 2000, *Environmental Isotopes in the Hydrological Cycle - Principles and Applications*. . S.l., s.n.

INGHAM, B., KO, M., LAYCOCK, N., et al., 2015, "First stages of siderite crystallisation during CO2 corrosion of steel evaluated using in-situ synchrotron small- and wide- angle X-ray scattering". In: *Faraday Discussions*. v. 180, pp. 171–190.

J.A. COLWELL AND B.N. LEIS, P.M.S., 2005, "Recent Developments in Characterizing". In: *Corrosion*. pp. 1–12.

JENSEN, G.A., 2010. *Offshore Pipelaying Dynamics*. . S.l.: NTNU.

JHA, V., LATTO, J., DODDS, N., et al., 2013. "Qualification of Flexible Fiber-Reinforced Pipe for 10,000-Foot Water Depths". In: *OTC 24160*. S.l.: s.n. 2013. pp. 1–9.

JIANG, C.Z., TOSCA, N.J., 2019, "Fe(II)-carbonate precipitation kinetics and the chemistry of anoxic ferruginous seawater". In: *Earth and Planetary Science Letters*. v. 506, pp. 231–242.

JIANG, C.Z., TOSCA, N.J., 2020, "Growth kinetics of siderite at 298.15 K and 1 bar". In: *Geochimica et Cosmochimica Acta*. v. 274, pp. 97–117.

JOHNSON, J.T., DURR, C.L., BEAVERS, J.A., 2000, "Effects of O2 and CO2 on near-neutral-pH stress corrosion crack propagation". In: *Corrosion 2000, NACE*.

KAHYARIAN, A., BROWN, B., NESIC, S., 2018. "Mechanism of CO2 corrosion of mild steel: A new narrative". In: *NACE - International Corrosion Conference Series*. S.l.: s.n. 2018.

KAHYARIAN, A., SINGER, M., NESIC, S., 2016, "Modeling of uniform CO2 corrosion of mild steel in gas transportation systems: A review". In: *Journal of Natural Gas Science and Engineering*. v. 29, pp. 530–549.

KERMANI, M.B., MORSHED, A., 2003a, "Carbon dioxide corrosion in oil and gas production - A compendium". In: *Corrosion*. v. 59, pp. 659–683.

KERMANI, M.B., MORSHED, A., 2003b, "Carbon Dioxide Corrosion in Oil and Gas Production — A Compendium". In: . v. 59, pp. 659–683.

KESAVAN, S., MOZHI, T.A., WILDE, B.E., 1989, "Technical Note: Potential-pH Diagrams for the Fe-Cl-H2O System at 25 to 150 C". In: *Corrosion*. v. 45, pp. 213–215.

KHALEGHI, A., SADRAMELI, S.M., MANTEGHIAN, M., 2020, "Thermodynamic and kinetics investigation of homogeneous and heterogeneous nucleation". In: *Reviews in Inorganic Chemistry*. v. 40, pp. 167–192.

LI, W., BROWN, B., YOUNG, D., et al., 2014, "Investigation of Pseudo-Passivation of Mild Steel in CO2 Corrosion". In: *Corrosion j*. v. 9312, pp. 294–302.

LIBERTO, S. DI, GABETTA, G., 1998, "STRESS CORROSION CRACKING BY ANODIC DISSOLUTION AND HYDROGEN PERMEATION IN PIPELINE STEELS". In: *Materials Science*. v. 33, pp. 411–420.

LIU, Q.Y., MAOA, L.J., ZHOU, S.W., 2014, "Effects of chloride concentration on CO2 corrosion of carbon steel in simulated oil and gas well environments". In: *Corrosion Science*. v. 84, pp. 165–171.

LIU, R., LI, J., LIU, Z., et al., 2015a, "Effect of pH and H2S concentration on sulfide stress corrosion cracking (SSCC) of API 2205 duplex stainless steel". In: *International Journal of Materials Research*. v. 106, pp. 608–613.

LIU, Z., GAO, X., DU, L., et al., 2015b, "Corrosion behavior of low-alloy steel with martensite/ferrite microstructure at vapor-saturated CO2 and CO2-saturated brine conditions". In: *Applied Surface Science*. v. 351, pp. 610–623.

LIU, Z.Y., LI, X.G., CHENG, Y.F., 2012, "Mechanistic aspect of near-neutral pH stress corrosion cracking of pipelines under cathodic polarization". In: *Corrosion Science*. v. 55, pp. 54–60.

LÓPEZ, D., SCHREINER, W., SÁNCHEZ, S., et al., 2003a, "The influence of carbon steel microstructure on corrosion layers An XPS and SEM characterization". In: *Applied Surface Science*. v. 207, pp. 69–85.

LÓPEZ, D.A., PEREZ, T., SIMISON, S.N., 2003b, "The influence of microstructure and chemical composition of carbon and low alloy steels in CO 2 corrosion . A state-of-the-art appraisal". In: *Materials & Design*. v. 24, pp. 561–575.

LOTZ, U., SYDBERGER, T., 1988, "CO2 corrosion of carbon steel and 13Cr steel in particle-laden fluid". In: *Corrosion*. v. 44, pp. 800–809.

MA, Z., YANG, Y., BROWN, B., et al., 2018, "Investigation of precipitation kinetics of FeCO3 by EQCM". In: *Corrosion Science*. v. 141, pp. 195–202.

MANKOWSKI, J., SZKLARSKA-SMIALOWSKA, Z., 1975, "Studies on accumulation of chloride ions in pits growing during anodic polarization". In: *Corrosion Science*. v. 15, pp. 493–501.

MCCARTHY, J., 1997, *Stress corrosion cracking on canadian oil and gas pipelines*. . S.l., s.n.

MORA-MENDOZA, J.L., TURGOOSE, S., 2002, "Fe3C influence on the corrosion rate of mild steel in aqueous CO2 systems under turbulent flow conditions". In: *Corrosion Science*. v. 44, pp. 1223–1246.

NEŠIĆ, S., 2007, "Key issues related to modelling of internal corrosion of oil and gas pipelines - A review". In: *Corrosion Science*. v. 49, pp. 4308–4338.

NESIC, S., THEVENOT, N., CROLET, J., et al., 1996. "Electrochemical properties of

iron dissolution in the presene of CO2 - Basics revisited". In: *Corrosion 1996, NACE*. S.l.: s.n. 1996.

OCHOA, N., VEGA, C., PÉBÈRE, N., et al., 2015, "CO2 corrosion resistance of carbon steel in relation with microstructure changes". In: *Materials Chemistry and Physics*. v. 156, pp. 198–205.

PALMER, A.C., KING, R.A., 2008, *Subsea Pipeline Engineering*. . Tulsa, Oklahoma USA, s.n.

PARKINS, R.N., 1979, "Environment sensitive fracture and its prevention". In: *British Corrosion Journal*. v. 14, pp. 5–14.

PARKINS, R.N., ZHOU, S., 1997a, "The stress corrosion cracking of C-Mn steel in CO2-HCO-3-CO2-3 solutions. I: Stress corrosion data". In: *Corrosion Science*. v. 39, pp. 159–173.

PARKINS, R.N., ZHOU, S., 1997b, "The stress corrosion cracking of C-Mn steel in CO2-HCO-3-CO23- solutions. II: Electrochemical and other data". In: *Corrosion Science*. v. 39, pp. 175–191.

PAUL, S., PATTANAYAK, A., GUCHHAIT, S.K., 2014, "Corrosion Behavior of Carbon Steel in Synthetically Produced Oil Field Seawater". In: *International Journal of Metals*. pp. 1–11.

PENG, S., ZENG, Z., 2015, "An experimental study on the internal corrosion of a subsea multiphase pipeline". In: *Petroleum*. v. 1, pp. 75–81.

PESSU, F., BARKER, R., NEVILLE, A., 2016, "Understanding pitting corrosion behavior of X65 carbon steel in CO2-saturated environments: The temperature effect". In: *Corrosion*. v. 72, pp. 78–94.

PESSU, F., BARKER, R., NEVILLE, A., 2020, "CO2 Corrosion of Carbon Steel: The Synergy of Chloride Ion Concentration and Temperature on Metal Penetration". In: *Corrosion*. v. 76.

QU, X.-F., YAO, Q.-Z., ZHOU, G.-T., 2011, "Synthesis of siderite microspheres and their transformation to magnetite microspheres". In: *European Journal of Mineralogy*. v. 23, pp. 759–770.

REMITA, E., 2009. *Investigation of the corrosion of a low alloyed steel in confined aqueous environments containing dissolved CO2*. . S.l.: L'UNIVERSITE PIERRE ET MARIE CURIE.

REMITA, E., KITTEL, J., TRIBOLLET, B., et al., 2008a, "EXPERIMENTAL AND THEORETICAL INVESTIGATION OF THE UNIFORM CORROSION IN THE ANNULUS OF OFFSHORE FLEXIBLE PIPELINES". In: *Nace*. pp. 1–17.

REMITA, E., TRIBOLLET, B., SUTTER, E., et al., 2008b, "A Kinetic Model for CO2 Corrosion of Steel in Confined Aqueous Environments". In: *Journal of The Electrochemical Society*. v. 155, pp. C41–C45.

ROGOWSKA, M., GUDME, J., RUBIN, A., et al., 2016, "Effect of Fe ion concentration on fatigue life of carbon steel in aqueous CO2 environment". In: *Corrosion Engineering Science and Technology*. v. 51, pp. 90–103.

RUBIN, A., GUDME, J., 2006, "Qualification of Steel Wire for Flexible Pipes". In: *CORROSION NACExpo*. pp. 1–19.

SALLEH, S., 2012. *Modelling Pitting Corrosion in Carbon Steel Materials*. . S.l.: s.n.

SCHLEGEL, M.L., BATAILLON, C., BLANC, C., et al., 2010, "Anodic activation of iron corrosion in clay media under water-saturated conditions at 90 °C: Characterization of the corrosion interface". In: *Environmental Science and Technology*. v. 44, pp. 1503–1508.

SHI, Z., ATRENS, A., 2011, "An innovative specimen configuration for the study of Mg corrosion". In: *Corrosion Science*. v. 53, pp. 226–246.

SK, M.H., ABDULLAH, A.M., KO, M., et al., 2017, "Local supersaturation and the growth of protective scales during CO2 corrosion of steel: Effect of pH and solution flow". In: *Corrosion Science*. v. 126, pp. 26–36.

SPARKS, C.P., 2007, *Fundamentals of Marine Riser Mechanics: Basic Principles and Simplified Analysis*. . 1st ed. Tulsa, Oklahoma USA, s.n.

SUN, J.B., ZHANG, G.A., LIU, W., et al., 2012, "The formation mechanism of corrosion scale and electrochemical characteristic of low alloy steel in carbon dioxide-saturated solution". In: *Corrosion Science*. v. 57, pp. 131–138.

SUN, W., NESIC, S., TECHNOLOGY, M., 2006, "BASICS REVISITED: KINETICS OF IRON CARBONATE SCALE PRECIPITATION IN CO2 CORROSION". In: *CORROSION NACExpo*. pp. 1–21.

SUN, W., NEŠIĆ, S., WOOLLAM, R.C., 2009, "The effect of temperature and ionic strength on iron carbonate (FeCO3) solubility limit". In: *Corrosion Science*. v. 51, pp. 1273–1276.

SUTCLIFFE, J.M., FESSLER, R.R., BOYD, W.K., et al., 1972. "Stress Corrosion Cracking of Carbon Steel in Carbonate Solutions.". . 1972. S.l.: s.n.

SUZUKI, T., YAMABE, M., KITAMURA, Y., 1973, "Composition of Anolyte Within Pit Anode of Austenitic Stainless Steels in Chloride Solution". In: *Corrosion*. v. 29, pp. 18–22.

TANG, X., CHENG, Y.F., 2011, "Quantitative characterization by micro-electrochemical measurements of the synergism of hydrogen, stress and dissolution on near-neutral pH stress corrosion cracking of pipelines". In: *Corrosion Science*. v. 53, pp. 2927–2933.

TANUPABRUNGSUN, T., YOUNG, D., BROWN, B., et al., 2012. "Construction and Verification of Pourbaix Diagrams for CO2 Corrosion of Mild Steel Valid up to 250°C". In: *Corrosion (Houston)*. S.l.: s.n. 2012. pp. C2012-0001418.

TOMSON, M.B., RICE, U., JOHNSON, M.L., 1991, "How Ferrous Carbonate Kinetics Impacts Oilfield Corrosion". In: .

UEDA, M., TAKABE, H., 1999, "EFFECT OF ENVIRONMENTAL FACTOR AND MICROSTRUCTURE ON MORPHOLOGY OF CORROSION PRODUCTS IN CO2 ENVIRONMENTS". In: *Corrosion*.

VAN WESTEN, T., GROOT, R.D., 2018, "Effect of Temperature Cycling on Ostwald Ripening". In: *Crystal Growth and Design*. v. 18, pp. 4952–4962.

XIA, Z., CHOU, K.C., SZKLARSKA-SMIALOWSKA, Z., 1989, "Pitting corrosion of carbon steel in CO2-containing NaCi brine". In: *Corrosion*. v. 45, pp. 636–642.

XIAOYAN, L., MINGZHAO, L., LIUQUN, F., et al., 2014, "Effects of Mn on Corrosion Resistant Property of AZ91 Alloys". In: *Rare Metal Materials and Engineering*. v. 43, pp. 278–282.

YEAN, S., SAIARI, H. AL, KAN, A.T., et al., 2008, "Ferrous Carbonate Nucleation and Inhibition". In: *SPE*. pp. 28–29.

YU, J., YU, J.C., ZHANG, L., et al., 2004, "Facile fabrication and characterization of hierarchically porous calcium carbonate microspheres". In: *Chemical Communications*. v. 1, pp. 2414–2415.

ZENG, Z., LILLARD, R.S., CONG, H., 2016, "Effect of salt concentration on the corrosion behavior of carbon steel in CO2 environment". In: *Corrosion*. v. 72, pp. 805–823.

ZHOU, Y., ZHANG, P., ZUO, Y., et al., 2017, "The structure and composition of corrosion product film and its relation to corrosion rate for carbon steels in CO2 saturated solutions at different temperatures". In: *Journal of the Brazilian Chemical Society*. v. 28, pp. 2490–2499.